University of Genova

School of Mathematical, Physical and Natural Sciences
Master's degree in Physics

Plasmonically enhanced fluorescence of Archaerhodopsin-based GEVIs for voltage imaging

Candidate:
Marco Locarno

Advisors:
Daan Brinks
Ornella Cavalleri

Co-advisor:
Claudio Canale

Academic Year 2018/19

Not a physicist. Not a biologist.
All he knows is what he's not.
If only he could see what he is...

Contents

Chapter 1

Introduction

When Michael Faraday first synthesized his gold colloids, he could never have imagined that more than 150 years later scientists would have used similar metal nanoparticles to bring forward research in fields like biomedical and energy engineering. Despite the fact that plasmonics has been harnessed from photonic devices to cancer treatment, its application in *all-optical electrophysiology* is rather ground-breaking and could open ways of understanding neural dynamics that were inconceivable until now.

In order to achieve a deep and fundamental understanding of the brain, detailed knowledge about its elementary units, *neurons*, is needed. Neurons are cells that are capable of receiving, computing and generating electrical signals that can be transmitted from one unit to another via connections called *synapses*. One of the most fascinating aspects of neuroscience is the nature of the signals, neither purely digital or analog, but a mix of the two. Not only "all-or-none" electrical spikes play a role in neural networks: *local subthreshold events* contribute to the fine tuning of neural spikes and synchronization of neighboring neurons [1].

Classical measuring techniques require external electrodes that physically access the inside of the cell to test the membrane potential [2]. As the electrode tip is usually wider than $1\mu m$, signals coming from smaller structures get inevitably averaged. Furthermore, electrodes are cumbersome and only a limited number of them can be used in a typical experiment. Optical methods overcome classical limitations of electrophysiology. An exceptional family of engineered proteins, *Genetically Encoded Voltage Indicators* (GEVIs), presents a fluorescence that is sensitive to voltage and can be expressed in mammalian cells [3]. In other words, simply by illuminating a neuron that expresses such proteins one can instantly measure the point-by-point membrane potential. This can be done for multiple neurons in the same field of view of the camera.

The biggest drawback of fluorescence microscopy is dictated by the diffraction limit of light, as described by Ernst Abbe in 1873. The minimum resolvable distance between two point-like sources is roughly $\lambda/2$, where λ is the wavelength of light. Even in the most favorable experiment, spatial resolution will be around $200nm$, meaning that the fluorescence coming from smaller cellular compartments is indistinguishable from the rest. As a consequence, subthreshold potentials in structures like small synapses or *dendritic spines* remain inaccessible.

Going beyond the diffraction limit is however possible thanks to modern nanoscopy tools based on *plasmonic nanoparticles*. When in proximity of a fluorophore, these metal nanoparticles can function as the equivalent of optical antennas, affecting the radiation field emitted [4]. The electromagnetic coupling between the fluorophore and the resonant metal nanoparticle greatly enhances the quantum yield of the molecule (the efficiency of its fluorescence compared to

non-radiative decays) by altering the local density of states and the local field experienced by the fluorophore. Near the nanoantenna, in fact, the electromagnetic field can even be ten-fold more intense than the incoming one, if the resonance condition is met. Stronger fluorescence appearing in diffraction-limited spots can directly be attributed to this plasmonic effect, also meaning that the optical signal is coming from a much more localized region (Figure 1.1). If the nanoparticles are specifically bound to determined molecules, then the selective, non-invasive study of subcellular compartments can be a reality.
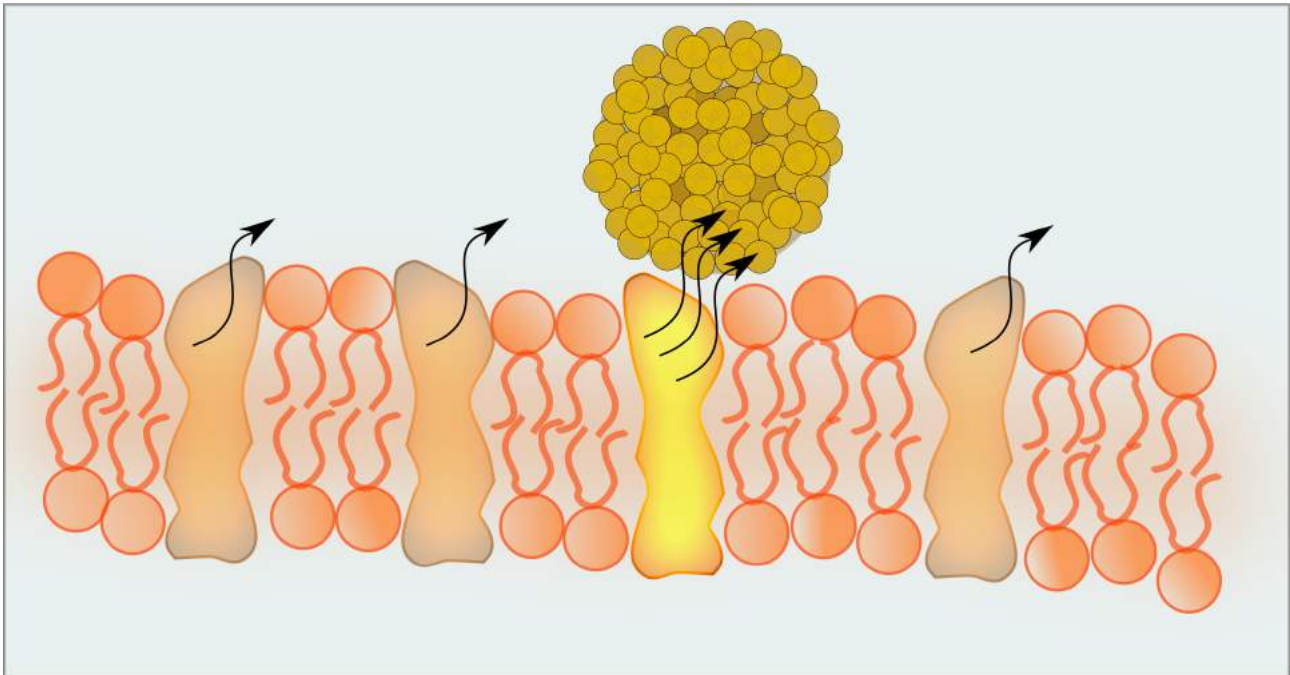

Figure 1.1: Plasmonically enhanced fluorescence of a low quantum yield membrane protein

The pioneering application of plasmonics to all-optical electrophysiology marks the birth of *voltage nanoscopy*. This novel field will cover a crucial role in neuroscience, as direct readout of the electrical signal in synapses and dendritic spines could unravel local mechanisms behind learning, memory and signal computation [5]. Voltage nanoscopy could even shed a light onto brain disorders like Alzheimer's disease, schizophrenia, autism, addiction, multiple sclerosis and chronic pain, and hopefully on how to treat them.

The first main gap to bridge in this novel field is finding the optimal features for nanoparticles so as to be resonant with the fluorescence of the GEVIs, in a very complex environment like the biological one, where many different molecules can affect the metal-GEVI interaction. Material, size, shape and dielectric coating of the nanoantennas are all parameters that affect the final plasmonic resonance and strength of the local electric fields. An additional question that is still open is whether the voltage sensitivity of the plasmonically enhanced fluorophores is modified and how. The alteration of local electric fields might have an unexpected influence on protein conformation and, consequently, on voltage sensitivity.

It is known that properly designed plasmonic nanoparticles enhance the quantum yield of fluorophores in controlled conditions. The hypothesis introduced in this thesis is that the fluorescence enhancement will happen as expected also in the biological environment under study, assuming that nanoantennas are close enough to the GEVIs (closer than $20nm$ from the surface of the particle). A second assumption is that the nanoparticles will be sparse enough to clearly distinguish the enhanced signal in diffraction-limited spots.

In this thesis a complete approach from simulations to biological application has been taken.

FDTD numerical simulations have been employed to precisely predict and quantify the field enhancement near the particles' surface when varying a set of controlled parameters. This allowed the optimization of the design of the nanoparticles, in relation to the fluorescent protein considered. Subsequently, gold nanorods produced by electron beam lithography and colloidal gold nanostars have both been fully characterized and finally tested on model cells expressing the GEVI under study.

Successful feature optimization of simulated nanoparticles hinted that the most suitable shapes to produce were gold nanorods and nanostars. The results discussed in the next chapters highlight the tunability and the stability of such nanoparticles, along with the practical limitations to overcome in future experiments. Although still preliminary, the very promising experiments strongly motivate further research on the subject.

Chapter 2

Theoretical framework

In this chapter I will briefly present the theoretical aspects behind my experimental work, from the biophysical problem to the features of plasmonic enhancement and the related simulation method employed. More emphasis is given to the section regarding the optical properties of metallic nanoparticles, in order to make my practical choices clearer to the reader.

Section 1 will briefly introduce some basic electrophysiology concepts that motivate my work; it is inspired by Solomon's general biology book [6], Kandel's neuroscience book [7] and Koch's computational neuroscience book [8].

Section 2 will focus on more specific optogenetics topics; it is mainly based on Ernst's rhodopsin review [9] and papers regarding the protein of interest.

Section 3 will cover classical light-matter interaction and its consequences on plasmonics; it is mainly based on Fox's materials optics book [10], Anghinolfi's Ph.D. thesis [11] and Brongersma's review [12].

Section 4 will present a simulation method used to predict and tune the plasmonic resonance to the desired parameters; it is based on Gedney's book [13] and Schneider's e-book [14].

2.1 Electrophysiology

Information in the nervous system is encoded in electrical signals that propagate from one cell to another. Environmental stimuli are converted into electrical signals by sensory neurons, then this information is processed through a complex neuronal network before eventually be transduced to other physical quantities, such as mechanical movement or biochemical production. All these fascinating mechanisms are due to the conductive properties of the cell membrane, and can arise either in animals and plants.

The cell membrane can be modeled as a *phospholipid bilayer* enriched with integral and peripheral *proteins* and *carbohydrates*. Since the phospholipids are made up of a hydrophylic polar head connected to two hydrophobic tails by a glycerol, in water they tend to self assemble in double layers exposing the hydrophylic heads to water and hiding the hydrophobic tails in the membrane interior. In this way, unfavorable interactions between hydrophobic tails and water are minimized. The phospholipid bilayer so formed is highly impermeable to ions and biomolecules, constituting a good dielectric barrier between the inside and the outside of the cell. Transmembrane proteins, acting as channels, carriers and ionic pumps control the ionic

fluxes between the interior and the exterior of the cell membrane. Very often carriers are neglected in circuit models, since they are slower and constitute only a secondary pathway for ionic species. The bilayer can be electrically modeled as a parallel-plate capacitor, while leakage channels are easily shown to behave like ohmic conductors and so are modeled as resistors.
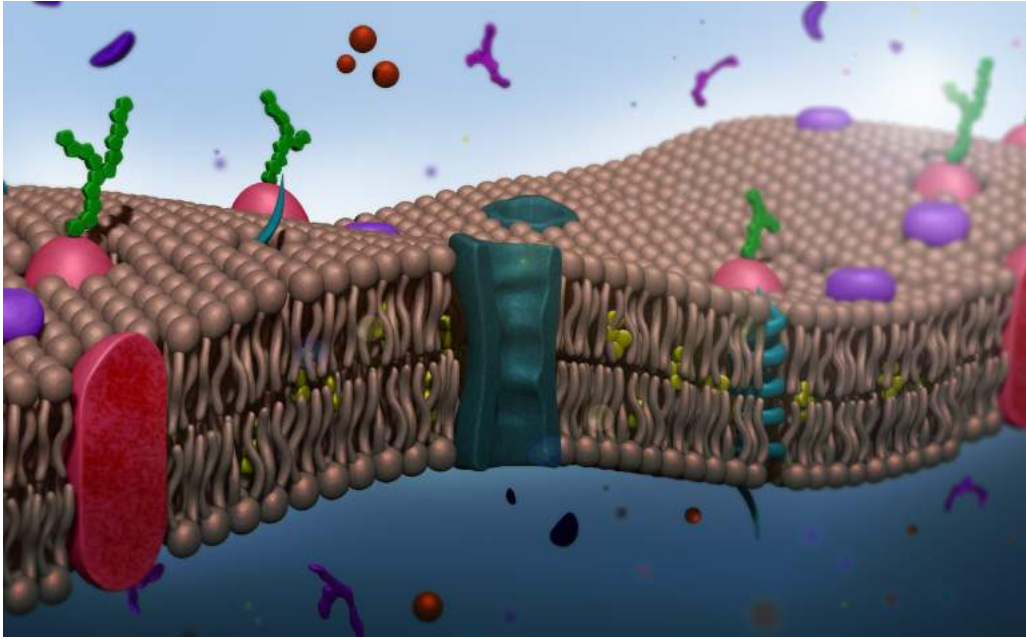

Figure 2.1: Graphical rendering of a cell membrane's section (courtesy of Noemi Rosano)

By consuming ATP, which is the main energy source of the cell, pumps can continuously transport ions against the concentration gradient. The charge separation induces an electrical gradient and gives rise to the so called *membrane potential*. For a single ion at equilibrium, electric potential between the cytoplasm and the external solution is given by Nernst equation:

$$E_i = \frac{RT}{z_i F} \ln \left(\frac{[c_i]_{out}}{[c_i]_{in}} \right) \tag{2.1}$$

where R is the ideal gas constant, T is the temperature, z_i is the valence of the ion, F is Faraday's constant and $[c_i]$ are the ionic concentrations outside or inside the cell. The Nernst potential has the equivalent function of a voltage generator, while Na^+/K^+ pumps can be modeled as two parallel current generators that regulate the charge separation across the membrane. The latter component is usually not included explicitly in the equations, but its effect is taken into account by considering Nernst potentials constant over time. It is important to note that when a cell is dead or not properly functioning ATP-driven pumps stop and membrane potential tends to zero (no charge separation).

If only one type of ion is involved, the cell membrane can be treated as a capacitor C_m in parallel to a series of a resistance R_i and a voltage generator E_i. This rough model can well describe the glial cells' membrane potential, where only K^+ ions are permeable.

When more ions are involved, such as Na^+, K^+ and Cl^- like in neurons, the more general *Goldmann-Hodgkin-Katz (GHK) voltage equation* for monovalent ions must be used to calculate the membrane potential:

$$V_m = \frac{RT}{F} \ln \left(\frac{\sum P_{i+}[c_{i+}]_{out} + \sum P_{i-}[c_{i-}]_{in}}{\sum P_{i-}[c_{i-}]_{out} + \sum P_{i+}[c_{i+}]_{in}} \right) \tag{2.2}$$

where ionic permeabilities P_i are involved and ions are divided between positive and negative. If permeabilities are constant in time and this leakage of ions through passive channels is

continuously counterbalanced by ion pumps, then V_m is called *membrane resting potential*. This resting potential varies from cell to cell but is in general around $-70mV$, meaning that the cytoplasm is at a lower potential compared to the extracellular side.

Simplifying all the leakage resistors into a single R_L and the membrane resting potential into a voltage generator E_L, then the equivalent circuit is similar to the one described for glial cells. It is common to describe the resistors by their conductance g rather than their resistance R: if a channel is in the closed state, it should have a theoretically infinite resistance, and computationally speaking this is not easy to handle. Furthermore, channels have a biophysical limitation to the number of ions that can pass through them per unit of time, so a zero resistance (and therefore infinite conductance) is never expected.
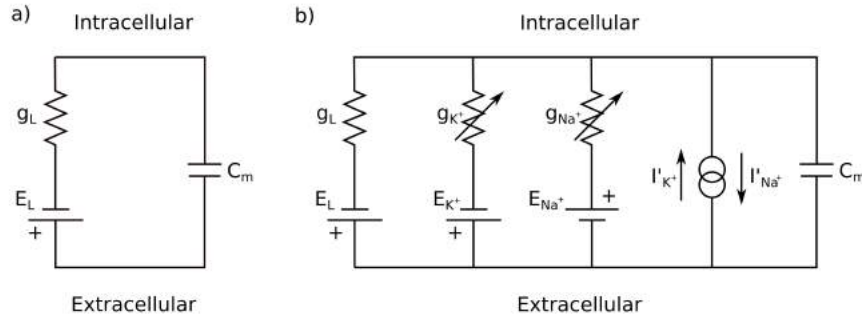

Figure 2.2: Membrane model a) RC-like and b) with variable conductances and Na^+/K^+ pump

If only leakage channels are considered and the cell is treated as isopotential, the equivalent circuit equation is rather simple:

$$C_m \frac{dV_m}{dt} = -g_L(V_m - E_L) \tag{2.3}$$

The solution to this differential equation is an exponential function, depending on the initial conditions, and approaching the resting potential E_L.

As studied by Hodgkin and Huxley [15], the electrical properties of membranes are not purely passive; instead, in certain depolarization conditions a non linear spike (called *action potential*) can be generated. The findings of Hodgkin and Huxley revealed that the action potential can be explained by two types of voltage-dependent channels, permeable respectively to Na^+ and K^+. These channels are closed in the resting phase, but above a certain potential threshold they show an interesting dynamic. Mathematically, the equivalent circuit equation becomes:

$$C_m \frac{dV_m}{dt} = -g_L(V_m - E_L) - g_{Na^+}(V_m - E_{Na^+}) - g_{K^+}(V_m - E_{K^+}) + I_{inj} \tag{2.4}$$

where g_{Na^+} and g_{K^+} are both voltage and time dependent. An external injected current I_{inj} has also been considered in the above equation, so as to simulate synapses or experimentally controlled inputs.

The voltage-gated channels that are modeled through g_{Na^+} and g_{K^+} have been described in detail by Hodgkin and Huxley after some voltage clamp experiments, but more complex models involving more ions, different gating mechanisms and compartmentalization of the cell can be developed for each neuron. One of the most complete and precise model for neurons is the Traub one [16], largely used in single cell simulations.

Many techniques have been developed to precisely measure the voltage and the currents with physical probes, ranging from patch clamp to multi-electrode arrays, but these usually fail in measuring smaller compartments' potential, like in dendritic spines. Because of this, spines' voltage dynamics and its role in plasticity is still to unravel, and that's why optical probes are thought to be the future of neuroscience and electrophysiology.

2.2 Optogenetics

Bacteria, plants and animals had adapted to the environment and enhanced their survival chances thanks to *photoreceptor* proteins. This kind of macromolecule is able to interact with light in some way and constitutes the fundamental building block for complex functions such as maintenance of the circadian rhythm and vision. Rhodopsins are a subset of photoreceptor proteins which take their peculiar name from ancient Greek: ῥόδον means "rose", because of their pinkish color, and ὄψις means "sight".

The common molecular architecture underlying microbial and animal rhodopsins consists of seven transmembrane α-helices covalently bound to a retinal chromophore via a Schiff base linkage. This second complex takes the name of *retinal Schiff base* and modifications of its protonation state induce rhodopsin activity.
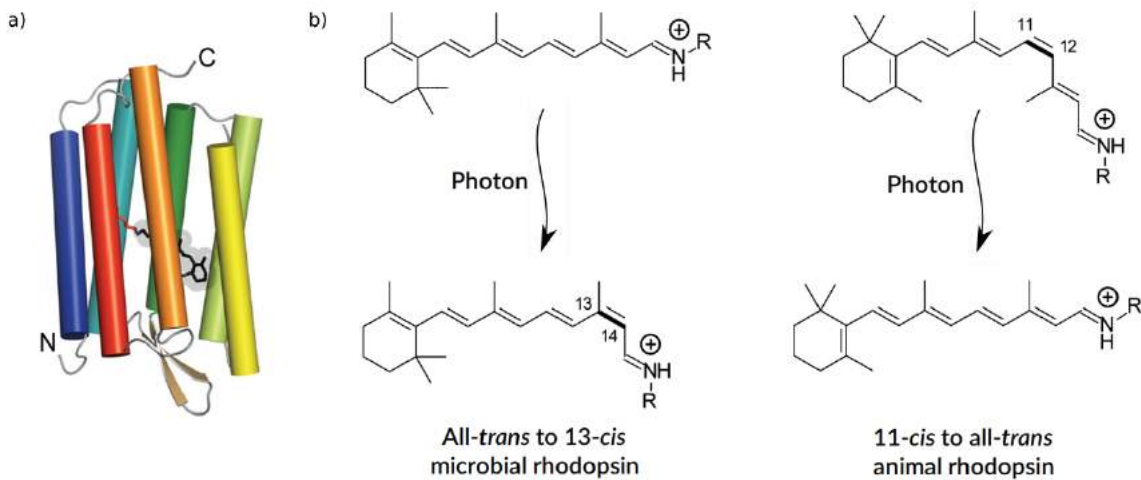

Figure 2.3: a) Bacteriorhodopsin (PDB ID: 1C3W) graphical representation with retinal in all-*trans* configuration and b) photoisomerization of either microbial and animal rhodopsin

In principle, a photon of a certain wavelength can be absorbed by the retinal which changes its conformation (from all-*trans* to 13-*cis* in microbial rhodopsins or from 11-*cis* to all-*trans* in animal rhodopsins) in a process called *photoisomerization*. Since animal rhodopsins and microbial GPCRs are highly specialized in function and expression site, we will focus our attention on a more versatile microbial subclass of rhodopsins.

The energy absorbed during the photoisomerization process leads to conformational changes that enable one of the following functions:

- Light-driven inward chloride pump (like *halorhodopsin*);

- Light-driven outward proton pump (like *bacteriorhodopsin* and *proteorhodopsin*);

- Light-gated cation channel (like *channelrhodopsin*);

- Light-sensor activating transmembrane or soluble transducer protein.

Most of the energy absorbed is converted into chemical energy, but losses eventually occur. The discovery that proteorhodopsin was weakly fluorescent in the near infrared when the retinal Schiff base was protonated and nonfluorescent when deprotonated shed a new light on the potential use of microbial proton pumps as voltage sensors [3]. Unfortunately, proteorhodopsin was impossible to express in mammalian cells, but this fluorescence mechanism was sought (and found) into other types of proton pumps, such as *Archaerhodopsin 3*.

Naturally light-driven outward proton pumps found in *archaea*, archaerhodopsins have found many applications in the field of optogenetics. Depending on the type, archaerhodopsins may be composed of 258 to 260 amino acids, presenting a very well conserved structure. Since archaerhodopsins can be expressed in mammalian cells and more specifically in neurons, in optogenetics they have been used to hyperpolarize cells and thus inhibit the firing of action potentials by illuminating the system with a green laser. Just like proteorhodopsins, archaerhodopsins showed a very weak voltage sensitive fluorescence and they have been engineered since then to optimize this feature. These engineered proteins belong to the wider family of the *genetically encoded voltage indicators* (GEVIs).

Derived from the Dead Sea microorganism *Halorubrum sodomense*, Archaerhodopsin 3 (Arch in short) is a wild type GEVI that functions as a light-driven outward proton pump. Its fluorescence is sensitive to membrane voltage, with twofold increased brightness from $-150mV$ to $+150mV$ with a sub-millisecond response time. Two main drawbacks of this GEVI are the generation of a hyperpolarizing photocurrent (due to its primary pumping feature) that suppresses any action potential, and a very dim fluorescence [17].

Protein engineering helped to block the pumping function by replacing the proton acceptor with a different amino acid, creating the Arch(D95N) mutant. Arch(D95N) shows a higher sensitivity to membrane voltage, namely threefold increased brightness from $-150mV$ to $+150mV$, but far slower response time ($\approx 40ms$). The absorption and emission spectra of Arch(D95N) are showed in Figure 2.4, presenting the absorption peak at $\approx 580nm$ (blue and green curves) and the emission peak at $\approx 680nm$, as showed in Kralj's paper [18].
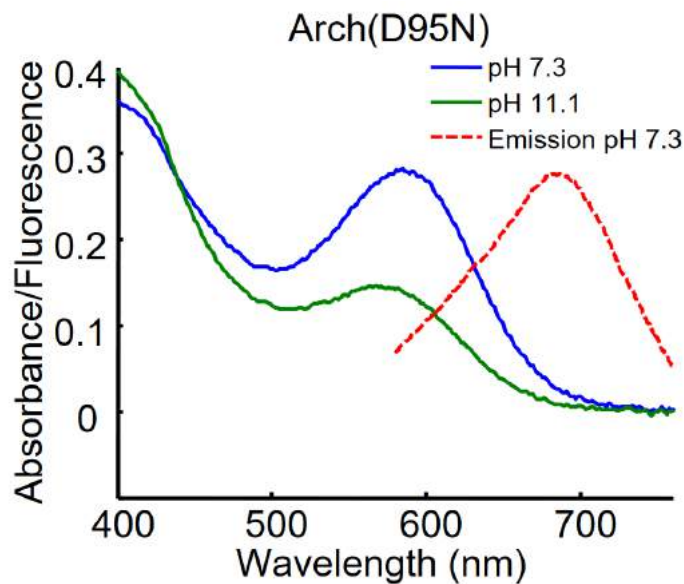
Figure 2.4: Absorption and emission spectra of Arch(D95N)[18]

The ideal GEVI for all-optical electrophysiology in neurons should present high sensitivity to membrane potential, high fidelity, good temporal and spatial resolution, high intensity and eventually high specificity in compartment expression. For instance, a voltage sensor that could allow the study of dendritic spines' voltage dynamics, without its fluorescence being covered by the background signal, would definitely help in disentangling the local mechanisms of plasticity and signal computation. Up to now, however, no GEVI has been exclusively expressed in dendritic spines, so the local voltage dynamics remains a mystery. While protein engineering can be helpful in finding a more suitable mutant by changing the aminoacidic sequence of the biomolecule, in a direct or random manner, another promising approach involves plasmonic enhancement.

2.3 Plasmonic Enhancement

A *plasmon* is a quasiparticle defined as a collective oscillation of free electrons in a metal; since this concept comes from the quantization of classical plasma oscillations, most of its properties can be derived directly from Maxwell's equations. Plasmons can take the form of propagating electron density waves along surfaces (*surface plasmon polaritons*, SPPs) or charge oscillations in metal nanoparticles (*localized surface plasmons*, LSPs). As fascinating as SPPs can be, in this thesis only LSPs will be covered. To better understand the classical derivation of the plasmonic resonance, I hereby propose a quick but complete review of some essential electromagnetic concepts applied in order to obtain the optical properties of metallic nanoparticles in a dielectric medium.

2.3.1 Light-matter interaction

Light is an electromagnetic wave that propagates in time and space following Maxwell's equations. The simplest electromagnetic wave is the *monochromatic plane wave* in which the electric field $\vec{E}(\vec{r}, t)$ and the magnetic field $\vec{B}(\vec{r}, t)$ are orthogonal sinusoids in the form:

$$\vec{E}(\vec{r}, t) = E \exp[i(\omega t - \vec{k} \cdot \vec{r})]\hat{E} \qquad \vec{B}(\vec{r}, t) = B \exp[i(\omega t - \vec{k} \cdot \vec{r})]\hat{B} \qquad (2.5)$$

where $\vec{k}$ indicates the wave vector, ω is the angular frequency and $\hat{E} \cdot \hat{B} = 0$, $\hat{E} \cdot \vec{k} = 0$, $\hat{B} \cdot \vec{k} = 0$. If $\hat{E}$ is constant over time and space the wave is said to be *linearly polarized*; if $\hat{E}$ is a superimposition of randomly oriented vectors then the wave is said to be *unpolarized.*

A monochromatic wave can be described by its period T and wavelength λ:

$$T = \frac{2\pi}{\omega} \qquad \lambda = \frac{2\pi}{|\vec{k}|} \qquad (2.6)$$

In free space and with excellent approximation in air, visible light has a wavelength that goes from $400nm$ (violet) to $700nm$ (red). In this range and at typical intensities light is usually not harmful for living organisms and therefore it is a good tool for studying biology: in fact, infrared light and microwaves can heat the watery biological environment, while ultraviolet can damage cells' DNA leading them to become cancerous or to die.

Optical properties of solids are closely related to microscopic features of matter, so that one way to study a certain material is then to characterize its response to light. Optical processes roughly include reflection, transmission and propagation. While light propagates inside a material several other interactions are possible:

- *Refraction*: light propagates inside a material at a lower speed compared to vacuum, following Snell's laws and without changing the intensity of the fields;

- *Absorption*: if the frequency of light is resonant with some of the molecular transition frequencies of the material, a fraction of light will be absorbed; absorbed energy can be lost in non-radiative processes (associated with the production of heat) or re-emitted in form of luminescence (as in fluorescent molecules);

- *Scattering*: the interaction with the material changes the direction of the incoming wave and eventually its frequency; reflection is a form of coherent elastic scattering happening at the surface.

Other more complex optical processes (such as frequency doubling) may happen at high intensities, but belong to non-linear optics and won't be treated in this thesis.

From a microscopical point of view, optical properties are due to the interaction of the electromagnetic field with each atom. For now, only homogeneus materials will be treated in detail. The electrons surrounding the nucleus are displaced, creating an oscillating dipole having dipole moment $\vec{p}$:

$$\vec{p} = \epsilon_0 \vec{\alpha} \otimes \vec{E} \tag{2.7}$$

where $\vec{\alpha}$ is the polarizability tensor and $\vec{E}$ the external field. It is important to note that in general $\vec{\alpha} = \vec{\alpha}(\omega)$. If the material is isotropic, then the polarizability tensor becomes a scalar quantity $\vec{\alpha} \to \alpha$ and so $\vec{E} || \vec{p}$.

The induced polarization density $\vec{P}$ is due to the collective effect of microscopic oscillating dipoles, and in isotropic and homogeneus materials it becomes:

$$\vec{P} = N\vec{p} \tag{2.8}$$

where N is the carrier density of the material.

The electric displacement vector $\vec{D}$ accounts for both external and induced electric field:

$$\vec{D} = \epsilon_0 \vec{E} + \vec{P} = \epsilon_0 \epsilon \vec{E} \tag{2.9}$$

where ϵ is the complex dielectric function $\epsilon = \epsilon_1 - i\epsilon_2$, in general frequency dependent. It can be shown that the refractive index n and the extinction coefficient κ are dependent on the real and imaginary parts of the dielectric function:

$$\epsilon_1 = n^2 - \kappa^2 \qquad \epsilon_2 = 2n\kappa \tag{2.10}$$

$$n = \sqrt{\frac{\sqrt{\epsilon_1^2 + \epsilon_2^2} + \epsilon_1}{2}} \qquad \kappa = \sqrt{\frac{\sqrt{\epsilon_1^2 + \epsilon_2^2} - \epsilon_1}{2}} \tag{2.11}$$

These equations link the optical properties (n and κ) with the microscopic features (ϵ) of a material. Using the Kramers-Kronig relations it can be proved that ϵ_1 and ϵ_2 (and therefore n and κ) are not independent from each other:

$$\epsilon_1(\omega) = 1 + \frac{2}{\pi}\mathbf{P}\int_0^\infty \frac{\epsilon_2(\omega')\omega'}{\omega'^2 - \omega^2}d\omega' \qquad \epsilon_2(\omega) = -\frac{2\omega}{\pi}\mathbf{P}\int_0^\infty \frac{\epsilon_1(\omega') - 1}{\omega'^2 - \omega^2}d\omega' \tag{2.12}$$

where $\mathbf{P}$ is the principal value of the integral. The Kramers-Kronig relations imply that by measuring one part of the complex function, the other can be directly calculated.

It is possible to link refractive index and extinction coefficient to *reflectance*:

$$R = \frac{I_R}{I_I} = \frac{(n-1)^2 + \kappa^2}{(n+1)^2 + \kappa^2} \tag{2.13}$$

where I_R is the flux of reflected light and I_I is the flux of incoming light. $R = 1$ means that all the incoming light is reflected, while $R = 0$ means that no light is reflected.

2.3.2   Brief history of plasmonics

While nanotechnology was born only some decades ago, natural optical phenomena had been intriguing human kind since ancient times. Witnessing and harnessing such "technologies" far preceded any possible scientific explanation: photonic crystals shape light creating spectacular iridescent colors in butterflies [19], dielectric particles suspended in air are responsible for fiery sunsets, blue skies and rainbows [20], lead-based quantum dots had been involved in black hair dyes by ancient Greeks and Romans [21] and copper nanoparticles were employed in red opaque glass production in Egypt and Mesopotamia [22].

As far as metallic nanoparticles are concerned, one of the most impressive historical pieces of glasswork is the *Lycurgus cup* (Figure 2.5a). Dated around the 4th century, this Roman cage cup is made up of dichroic glass, so that it appears red if light is passing through it from the inside but green if light is reflected from the outside. It depicts the legend of king Lycurgus, bound and killed by the vine as a punishment for trying to murder Dionysus's follower Ambrosia. Recent analysis showed that the dichroism is due to the presence of colloidal gold and silver nanoparticles dispersed throughout the glass. It is very unlikely that the process was understood and controllable at that time, so the hypothesis of accidental contamination from silver-gold alloy residues in the workshop is more realistic. The particles embedded have diameters around $70nm$, meaning that they are invisible to optical microscopy and require transmission electron microscopy (TEM) to be seen. [23]

Michael Faraday got the credit for the first scientific approach to the subject by methodically performing pioneeristic experiments on gold colloids, in the 1850s. What puzzled him was the ruby red color of the solutions synthesized (Figure 2.5b), far distant from the aureate color of bulk gold. A satisfying classical explanation of this phenomenon came only in 1904, when Maxwell Garnett combined the new Drude theory of metals with Lord Rayleigh's description of electromagnetic properties of small spheres. This theory was purely based on bulk optical parameters of metals, and it wasn't until 1970 that it was re-elaborated by Uwe Kreibig and Peter Zacharias. For the first time, they explained the electronic and optical response of silver and gold nanoparticles in terms of localized surface plasmon excitations. It became clear then that size, shape, arrangement, medium and temperature have all a crucial role in intensity and tuning of plasmonic resonances.

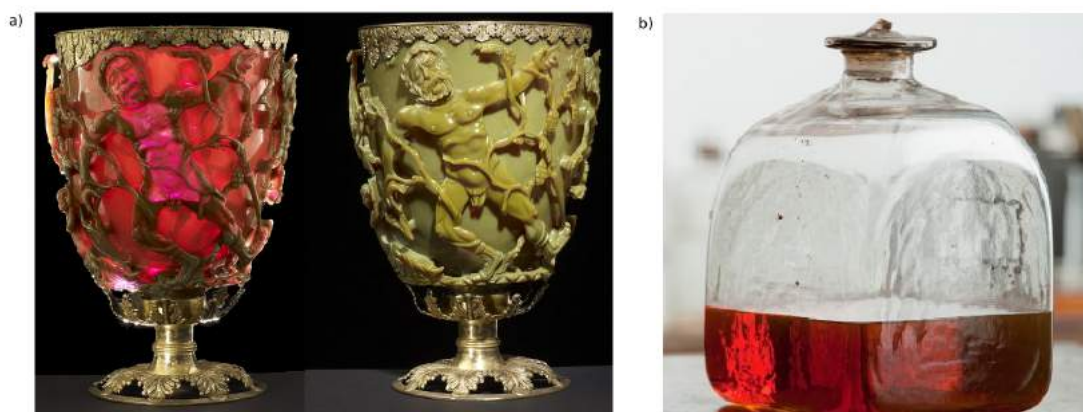Figure 2.5: a) Lycurgus cup's color changes depending on if the light is transmitted (left) or reflected (right) [24] b) Faraday's gold colloidal dispersion in a flask [25]

From the early 2000's on, the interest in plasmonics boomed, mainly thanks to novel nanofabrication techniques, to commercialization of simulation software and to the plethora of biological and biomedical possible applications.

In fact, the integration of plasmonic resonances and biochemical functionalization finds wide usage in:

- biosensing and imaging;

- single-nanoparticle spectroscopy;

- surface enhanced Raman scattering (SERS);

- metal-enhanced fluorescence (MEF);

- site-dependent photothermolysis.

The renewed interest in plasmonics is motivating many application-oriented research projects, giving rise to the need of stronger collaborations between physicists, material scientists, biologists, chemists, bioengineers and physicians.

2.3.3 From Lorentz model to plasmonic resonance

A simple yet descriptive derivation of the plasmonic resonances combines the Drude theory of metals and the generalization of Clausius-Mossotti relation. While the former will be explored in detail starting from the Lorentz model, the latter will only be quoted. An elegant and complete proof of it can be found in Bohren and Huffman's book [26].

Drude model for metals

Whatever material is taken into consideration, each atom in it can be approximated as a negative charge bound to a positive nucleus via a spring-like force. If the negative charge is moving, it will experience a viscous friction due to the collisions with other entities in the surrounding environment. Since each nucleon is about 1836-fold heavier than the electron, when an incoming electromagnetic wave interacts with the atom only the negative charge will be displaced. This is often referred to as the *Lorentz oscillator model*, a classical description of materials proposed years before the discovery of the electron.
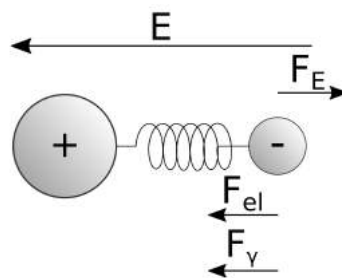

Figure 2.6: Lorentz oscillator model for an atom

The displacement x of the electron caused by the external field $E(t)$ is ruled by Newton's second law of motion (refer to Figure 2.6):

$$m\ddot{x} = F_E - F_{el} - F_\gamma \quad \Rightarrow \quad m\ddot{x} + m\gamma\dot{x} + m\omega_0^2 x = eE(t) \quad \Rightarrow \quad \ddot{x} + \gamma\dot{x} + \omega_0^2 x = \frac{e}{m}E(t) \quad (2.14)$$

where m is the effective mass of the electron, ω_0 is the resonance frequency of the oscillator and γ is the damping frequency, all dependent on the material considered. In particular, γ is given by *Matthiessen's rule* for different independent collision events, each of time constant τ_i:

$$\gamma = \sum_i 1/\tau_i \qquad (2.15)$$

If the incoming wave is a continuous plane wave $E(t) = E^0 e^{i\omega t}$ of frequency ω and complex amplitude E^0, one may search for solutions in the following form:

$$x(t) = x_0 e^{i\omega t}, \qquad \dot{x}(t) = x_0(i\omega)e^{i\omega t} \qquad \ddot{x}(t) = x_0(-\omega^2)e^{i\omega t} \tag{2.16}$$

where x_0 is a complex function of ω.

Substituting it in (2.14) we get:

$$-x_0\omega^2 e^{i\omega t} + \gamma x_0 i\omega e^{i\omega t} + \omega_0^2 x_0 e^{i\omega t} = \frac{e}{m}E^0 e^{i\omega t} \tag{2.17}$$

$$x_0(-\omega^2 + i\gamma\omega + \omega_0^2) = \frac{eE^0}{m} \tag{2.18}$$

$$x_0 = \frac{eE^0}{m}\frac{1}{\omega_0^2 - \omega^2 + i\gamma\omega} \tag{2.19}$$

Therefore the displacement $x(t)$ and the dipole moment $p(t)$ can be obtained:

$$x(t) = \frac{e}{m}\frac{1}{\omega_0^2 - \omega^2 + i\gamma\omega}E(t) \tag{2.20}$$

$$p(t) = -ex(t) = -\frac{e^2}{m}\frac{1}{\omega_0^2 - \omega^2 + i\gamma\omega}E(t) \tag{2.21}$$

If the polarization vector is taken in the same direction of the field, it results:

$$P(t) = -Np(t) = \frac{Ne^2}{m}\frac{1}{\omega_0^2 - \omega^2 + i\gamma\omega}E(t) \tag{2.22}$$

where N is the carrier density of the material. In case of isotropic material, the displacement vector $\vec{D}$ is:

$$\vec{D} = \epsilon_0\vec{E} + \vec{P} = \epsilon_0\epsilon\vec{E} \tag{2.23}$$

where ϵ is the complex dielectric function. Putting together (2.22) and (2.23):

$$\epsilon = 1 + \frac{Ne^2}{\epsilon_0 m}\frac{1}{\omega_0^2 - \omega^2 + i\gamma\omega} \tag{2.24}$$

Separating the function in the real and the imaginary parts $\epsilon = \epsilon_1 - i\epsilon_2$:

$$\epsilon_1 = 1 + \frac{Ne^2}{\epsilon_0 m}\frac{\omega_0^2 - \omega^2}{(\omega_0^2 - \omega^2)^2 + (\gamma\omega)^2}, \qquad \epsilon_2 = \frac{Ne^2}{\epsilon_0 m}\frac{\gamma\omega}{(\omega_0^2 - \omega^2)^2 + (\gamma\omega)^2} \tag{2.25}$$

It should be noted that here γ represents the peak's full width half maximum (FWHM).

The *Drude model for metals* can be derived directly from the Lorentz oscillator model by setting $\omega_0 = 0$, meaning that the electrons are not bound to the nucleus and therefore do not experience a restoring force but only a viscous friction due to collisions:

$$\epsilon_m = 1 + \frac{Ne^2}{\epsilon_0 m}\frac{1}{-\omega^2 + i\gamma\omega} = 1 - \frac{\omega_P^2}{\omega^2 - i\gamma\omega} = 1 - \frac{\omega_P^2}{\omega^2 + \gamma^2} - i\frac{\omega_P^2\gamma}{\omega^3 + \gamma^2\omega} \tag{2.26}$$

where the *plasma frequency* $\omega_P = \sqrt{\frac{Ne^2}{\epsilon_0 m}}$ has been introduced, different for every metal. But what happens to the material at this frequency? By calculating $\epsilon_m(\omega_P)$ one gets:

$$\epsilon_m(\omega_P) = 1 - \frac{1}{1 - i\frac{\gamma}{\omega_P}} = \frac{1}{1 + i\frac{\omega_P}{\gamma}} \tag{2.27}$$

Since experimentally it's almost always true that $\omega_P \gg \gamma$:

$$|\epsilon_m(\omega_P)| = \frac{1}{\sqrt{1 + (\frac{\omega_P}{\gamma})^2}} \approx 0 \tag{2.28}$$

By combining (2.11) and (2.13) it is possible to get the reflectance:

$$n(\omega_P) \approx 0, \quad \kappa(\omega_P) \approx 0 \qquad \Rightarrow \qquad R(\omega_P) \approx 1 \tag{2.29}$$

meaning that at the plasma frequency the material is perfectly reflective.

Much above such frequency the dielectric function of the metal becomes:

$$\epsilon_m(\omega \gg \omega_P) \approx 1 \tag{2.30}$$

and again we can calculate the reflectance:

$$n(\omega_P) \approx 1, \quad \kappa(\omega_P) \approx 0 \qquad \Rightarrow \qquad R(\omega_P) \approx 0 \tag{2.31}$$

meaning that at higher frequencies the material is transparent to electromagnetic radiation.

Quasi-Static Approximation

For metals that present a plasmonic resonance in the visible or UV range (Ag, Au, Cu and Al), spheres of radii under the hundred of nanometers can be treated as oscillating dipoles. This approach is called *Quasi-Static Approximation* and is motivated by the small phase difference in the local field in different regions of the particle. Mathematically this translates to:

$$d \ll \lambda \quad \Rightarrow \quad \vec{E}^0(\vec{r}, t) = \vec{E}^0 e^{i(\omega t - \vec{k} \cdot \vec{r})} \approx \vec{E}^0 e^{i\omega t} \tag{2.32}$$

This approximation let us consider the electron cloud (in Figure 2.7 depicted in blue) as collectively oscillating in the same direction, so instantly each atom inside the particle experiences the same electric field.
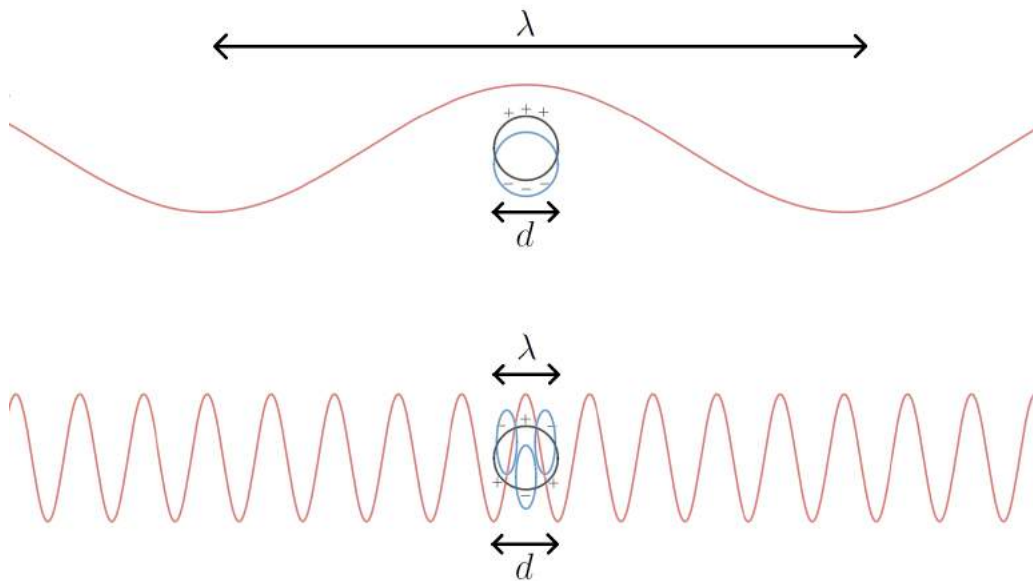

Figure 2.7: Dipolar (above) and multipolar (below) excitation of the free electrons in metals

It is important to note that larger particles may produce a plethora of effects that cannot be explained as the simple radiation of a dipole, because multipolar effects arise. Eventually, very large particles will exhibit the same optical properties of bulk metal.

Generalization of Clausius-Mossotti relation for ellipsoids

Consider an isolated ellipsoid having a complex dielectric function ϵ_m and semiaxes respectively a_x, a_y and a_z, immersed in a host having a real and positive dielectric constant ϵ_h. Under the Quasi-Static Approximation, all the atomic dipole moments are the same and sum coherently to produce a single macroscopic dipole moment.
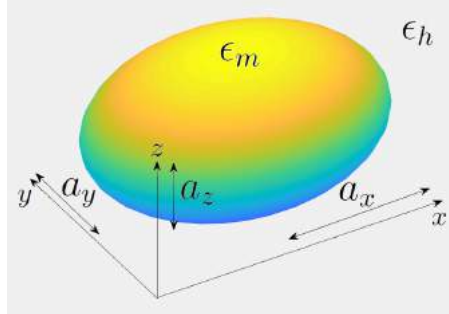

Figure 2.8: Ellipsoidal particle immersed in a dielectric medium

The nanoparticle's dipole moment $\vec{p}$ is function of the *polarizability tensor* $\vec{\alpha}$ as well as of the *local electric field* $\vec{E}_{loc}$. The latter is different from the incoming field $\vec{E}^0$ because of the polarization of the host, but if the dielectric medium is homogeneous and isotropic then the local field will be proportional to the incoming one $(\vec{E}_{loc} = \epsilon_h \vec{E}^0)$ and so:

$$\vec{p} = \epsilon_0 \vec{\alpha} \otimes \vec{E}_{loc} = \epsilon_0 \epsilon_h \vec{\alpha} \otimes \vec{E}^0 \tag{2.33}$$

It is important to note that for most cases $\vec{\alpha}$ is a diagonal matrix.

While Clausius-Mossotti relation describes the polarizability of a spherical particle in vacuum, a similar equation can be obtained for this more general case:

$$\alpha_i = \frac{4\pi a_x a_y a_z}{3} \frac{\epsilon_m - \epsilon_h}{\epsilon_h + L_i(\epsilon_m - \epsilon_h)}, \qquad i = x, y, z \tag{2.34}$$

where L_i is the *depolarization factor* for the i-th axis, written as:

$$L_i = \frac{a_x a_y a_z}{2} \int_0^\infty \frac{dq}{(q + a_i^2)\sqrt{\prod_{\eta = x,y,z}(q + a_\eta^2)}} \tag{2.35}$$

It can be shown an important property of these depolarization factors:

$$\sum_{i=x,y,z} L_i = 1 \tag{2.36}$$

Thanks to this normalization property some easy geometries (see Table 2.1) can be treated without calculating the integrals explicitly. Anisotropy is then reflected on the matrix nature of $\vec{\alpha}$, leading $\vec{p}$ to not being parallel to $\vec{E}^0$.

Particle Shape	Semiaxes	Depolarization factors
Sphere	$a_x = a_y = a_z$	$L_x = L_y = L_z = 1/3$
Long cylinder	$a_x \gg a_y, a_z$	$L_x = 0, \quad L_y = L_z = 1/2$
Large disk	$a_x = a_y \gg a_z$	$L_x = L_y = 0, \quad L_z = 1$

Table 2.1: Depolarization factors for some typical geometries

Clearly, the sphere in vacuum case coincides with the Clausius-Mossotti relation:

$$\alpha_i = 3v \frac{\epsilon_m - 1}{\epsilon_m + 2}, \qquad i = x, y, z \tag{2.37}$$

in which v is the volume of the spherical particle.

Plasmonic resonance

From equation (2.34) it is easy to see that if the denominator approaches zero the polarizability intensity drastically increases, leading to a strong dipole moment at frequency ω_{res}. This resonance condition translates to the requirement that, in a given direction along i-axis:

$$\text{Re}\big[\epsilon_m(\omega_{res})\big] = -\frac{1 - L_i}{L_i}\epsilon_h, \qquad \text{Im}\big[\epsilon_m(\omega_{res})\big] \approx 0 \tag{2.38}$$

For a sphere, the above equations reduce to the so called *Fröhlich condition*:

$$\text{Re}\big[\epsilon_m(\omega_{res})\big] = -2\epsilon_h, \qquad \text{Im}\big[\epsilon_m(\omega_{res})\big] \approx 0 \tag{2.39}$$

Applying such condition to Drude model in equation (2.26), the *resonance frequency* ω_{res} can be obtained:

$$\omega_{res} = \sqrt{\frac{\omega_P^2}{1 + 2\epsilon_h} - \gamma^2} = \omega_P\sqrt{\frac{1}{1 + 2\epsilon_h} - \frac{\gamma^2}{\omega_P^2}} \approx \frac{\omega_P}{\sqrt{1 + 2\epsilon_h}} \tag{2.40}$$

where in the last step the (reasonable) assumption of $\omega_P \gg \gamma$ has been introduced.

Figure 2.9 below shows a simulation of the plasmonic resonance for a spherical nanoparticle having gold-like Drude parameters, put either in vacuum or water. Just as predicted by the equation (2.40), in vacuum $\lambda_{res} \approx 430nm$ and in water $\lambda_{res} \approx 520nm$.
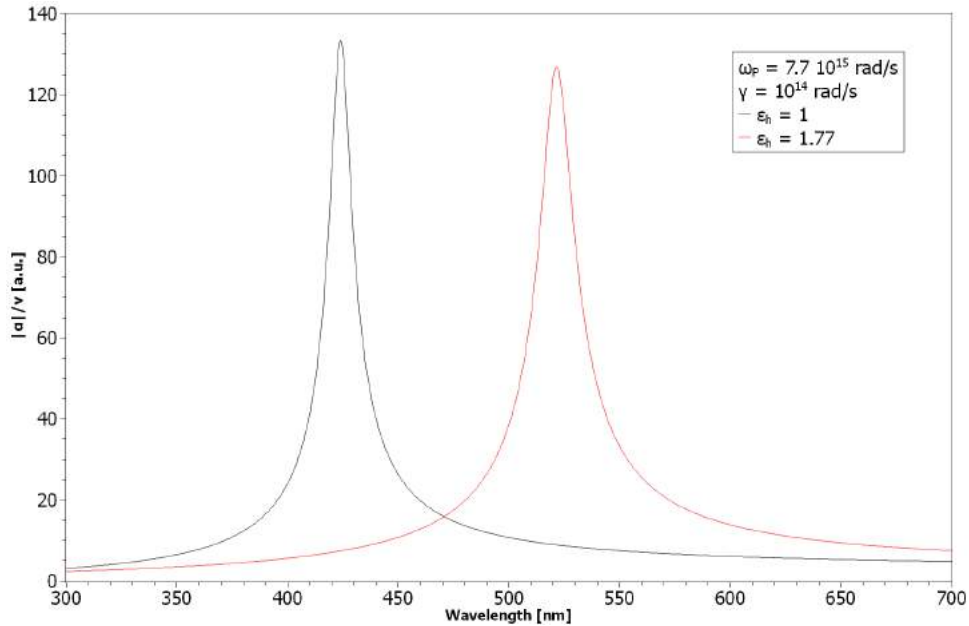

Figure 2.9: Simulated plasmonic peak for a spherical nanoparticle with gold-like parameters

Unfortunately, only few metals (namely Ag, Au, Cu and Al) happen to satisfy the Fröhlich condition, having a sufficiently low imaginary part of the dielectric function at the resonance frequency to show a peak. The window of obtainable plasmonic resonances is then limited to the natural properties of those metals. Even worse, not all these materials are suitable for biological applications: Al has a nice resonance, but in the UV; Ag has a higher peak compared to Au, but it oxidizes; Cu both has a little resonance peak and oxidizes. Sometimes the drawbacks are negligible for certain applications, but in principle cytotoxicity has always to be checked.

In the dipolar regime, the Rayleigh formula for cross sections can be applied:

$$\sigma_{abs} = k\mathrm{Im}[\alpha], \qquad \sigma_{sca} = \frac{k^4}{6\pi}|\alpha|^2 \tag{2.41}$$

where k is the wave number. It is important to note the cross sections' dependence on α and, as a consequence, on the volume: since the absorption cross section σ_{abs} scales linearly with v while the scattering one σ_{sca} scales quadratically with it, it is possible to assume that smaller particles mainly absorb light while larger particles mainly scatter it.

The total electric field outside the particle is the superimposition of the incoming field $\vec{E}^0$ and the dipolar field generated by the particle, so for a continuous wave the local field amplitude will result:

$$\vec{E}(\vec{r}) = \vec{E}^0 + \frac{1}{4\pi\epsilon_0\epsilon_h}\frac{3(\vec{r}\cdot\vec{p})\vec{r} - r^2\vec{p}}{r^5} \tag{2.42}$$

where r is the distance from the center of the particle. It comes naturally that resonances in α will reflect on $\vec{p}$ and subsequently on the local electric field $\vec{E}(\vec{r})$. Field enhancement is typically quantified by $|E|^2/|E^0|^2$ (as in Figure 2.10); in simulations $|E^0|$ is usually set as unitary, since non-linear effects due to the amplitude of the incoming wave are not expected, and light is typically linearly polarized in a certain direction.
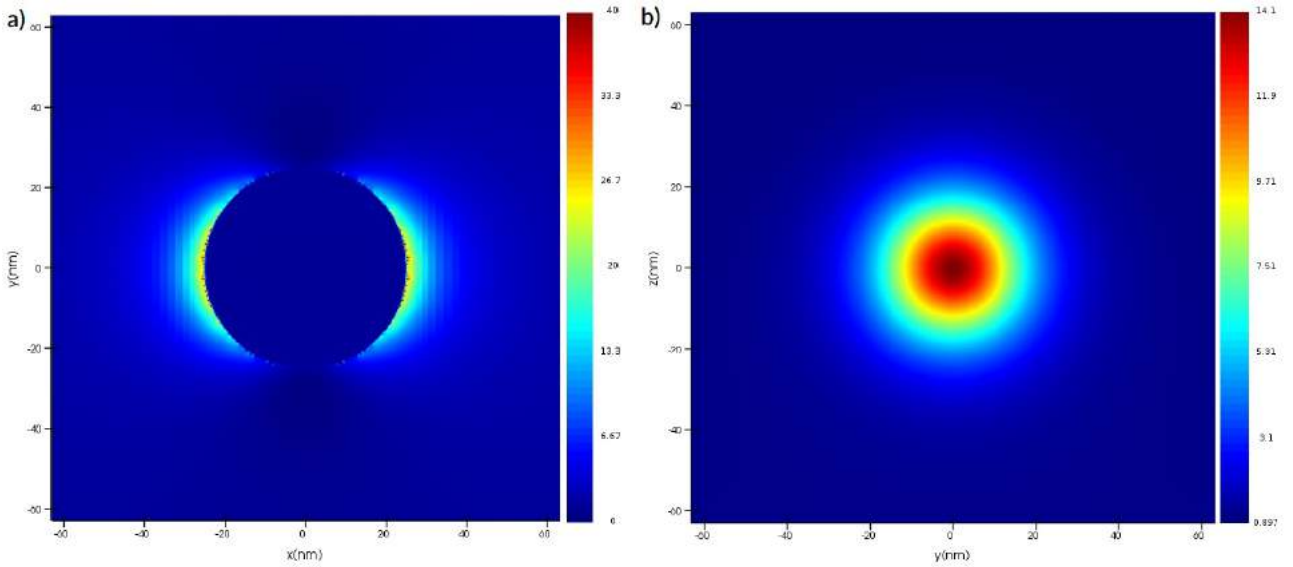

Figure 2.10: Simulated $|E|^2/|E^0|^2$ at $\lambda = 520nm$ near a gold spherical nanoparticle of $R = 25nm$ in water a) in the XY plane ($z = 0$) and b) in the YZ plane ($x = 4nm$ away from nanoparticle)

2.3.4 Corrections to Quasi-Static Approximation

The Quasi-Static Approximation describes fairly well a lot of processes happening at the nanoscale, such as the absorption of certain colors or the local field enhancement in the proximity of metallic nanoparticles, but fails in predicting other effects due to the size and the arbitrary shape of the particles. Although modern simulation techniques can give high precision results for any imaginable nanostructure, a deeper insight about the corrections to the dipolar limit can be helpful when collecting and interpreting the data.

Surface damping

Up to now the damping frequency γ has been implicitly considered dominated by the collisions of the electron with other electrons, nuclei in the lattice or phonons, but at a very small scale it will also impact with the particle boundary. This is possible when the dimensions of the particle are smaller than the *mean free path* (λ_{MFP}), that is the average distance traveled by the electron between two consecutive collisions; in other words, if the particle is small enough the electrons will feel the boundary way before colliding with other objects [26]. The empirical model developed hereafter well matches experimental data and in the end is very similar to the exact one obtainable with quantum calculations.

As the free electrons move at the Fermi velocity v_F, the characteristic time between two consecutive collisions with the boundary will be:

$$\tau_{boundary} = \frac{\lambda_{boundary}}{v_F} \tag{2.43}$$

where $\lambda_{boundary}$ is the characteristic length of the process. By applying equation (2.15) the damping frequency will become:

$$\gamma = \gamma_{bulk} + \frac{1}{\tau_{boundary}} = \frac{v_F}{\lambda_{MFP}} + \frac{v_F}{\lambda_{boundary}} \tag{2.44}$$

where γ_{bulk} is the bulk metal damping frequency. For a sphere of radius r Kreibig used the linear relation $\lambda_{boundary} = 4/3r$, but coefficients between 1 and 4/3 have been used by other authors. The use of this linear relation with coefficient 4/3 is motivated in Appendix A.

Around the plasma frequency it is almost always true that $\omega \gg \gamma$, so in first approximation the Drude model (equation (2.26)) becomes:

$$\epsilon_1 \approx 1 - \frac{\omega_P^2}{\omega^2}, \qquad \epsilon_2 \approx \frac{\omega_P^2 \gamma}{\omega^3} \tag{2.45}$$

While the real part is almost unchanged when introducing the damping correction, near the Fröhlich frequency the imaginary part can be rewritten as:

$$\epsilon_2 \approx \frac{\omega_P^2}{\omega_{res}^3}\left(\gamma_{bulk} + \frac{3v_F}{4r}\right) = \epsilon_{2_{bulk}} + A\frac{v_F}{r} \tag{2.46}$$

where the Kreibig relation and the constant A have been employed. For very small particles this implies that at ω_{res} the condition of small ϵ_2 is not true anymore, therefore drastically diminishing the resonance peak in α. In practice this means that excessively small particles are useless for most applications.

Modified long-wavelength approximation

The dipolar approximation is good as long as the dimensions of the metallic nanoparticle are $d \ll \lambda$, otherwise variations in the incoming field will not be negligible anymore and multipolar modes will eventually be excited. Between this dipolar treatment and the brute-force computational solution of Maxwell's equations lies the so called *modified long-wavelength approximation* (MLWA), a correction to the polarizability obtained in the Quasi-Static Approximation that enables it to take into account retardation effects [27].

Consider an ellipsoidal nanoparticle of semiaxis $a_i, i = x, y, z$ excited by an electromagnetic field. The MLWA electrodynamic corrections are included rewriting equation (2.33):

$$\vec{p} = \epsilon_0 \epsilon_h \vec{\alpha} \otimes (\vec{E}^0 + \vec{E}_{MLWA}) \tag{2.47}$$

where $\vec{E}_{MLWA}$ is the radiative correction given by:

$$E_{MLWA,i} = \frac{1}{4\pi\epsilon_0\epsilon_h} \left(\underbrace{\frac{k^2}{a_i}}_{\text{dynamic depolarization}} + \underbrace{i\frac{2}{3}k^3}_{\text{radiation damping}} \right) p_i, \quad i = x, y, z \tag{2.48}$$

in which $k = 2\pi/\lambda$ is the wave number. The first term in (2.48) is due to the depolarization of the radiation across the particle surface, while the second one describes the radiative losses of the induced dipole. According to this approximation, an increase in particle size will result in a red shifted, broadened and less intense plasmonic resonance.

The overall effect on the polarizability is:

$$\alpha_{MLWA,i} = \frac{\alpha_i}{1 - \frac{\alpha_i}{4\pi} \left(\frac{k^2}{a_i} + i\frac{2}{3}k^3 \right)}, \quad i = x, y, z \tag{2.49}$$

The MLWA usually works well for nanoparticles of dimensions up to $\approx 200nm$, above which multipolar resonances cannot be neglected anymore and computational methods are required.

Realistic dielectric medium

Although typically modeled as constant, the optical parameters of dielectric media are slightly dependent on wavelength, giving rise to the phenomenon of *dispersion*. Neglecting this characteristic may eventually lead to an inaccurate description of the plasmonic peak position or intensity.

In biological applications water is the typical medium considered. The refractive index of water in the visible range is shown in Figure 2.11, while the extinction coefficient is not plotted since it is very close to zero [28].
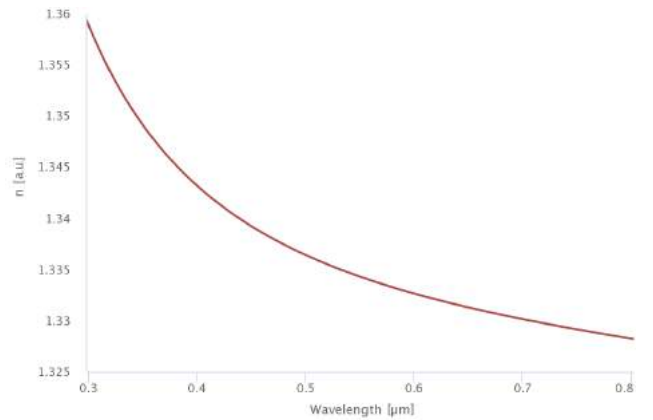

Figure 2.11: Refractive index of H_2O at $24.0°C$

Accounting for this wavelength dependence in either analytical or computational modeling is useful as well as easy and not time consuming. Polynomial interpolation of data is usually sufficient for a good quantitative description of the phenomenon.

2.3.5 Metal-Enhanced Fluorescence (MEF)

In Section 2.2 a brief overview on optogenetics has been given, introducing the concepts of photoisomerization of rhodopsins and fluorescent voltage sensors. The combination of plasmonic resonance and fluorescence emission leads to the so called *metal-enhanced fluorescence* (MEF), on which the experimental chapters of this thesis will mainly focus. After a first introduction on the principles of fluorescence [29], the interaction of metallic nanoparticles and fluorophores will be broadly covered [30].

Fundamentals of fluorescence

The emission of light occurring from the disexcitation of electronic states is generally called *luminescence*. The types of luminescence can be categorized by the energy source in the process (for example chemiluminescence, electroluminescence, photoluminescence) or by the nature of the excited state (*fluorescence* if singlet, *phosphorescence* if triplet). The main difference between fluorescence and phosphorescence is the time spent in the excited state: since triplet transitions to the ground state are forbidden, phosphorescence lifetimes range typically from milliseconds to seconds; on the contrary, singlet transitions are allowed and therefore fluorescence lifetimes range from nanoseconds to milliseconds.

One elegant way to illustrate the processes of electronic excitation and disexcitation is the *Jablonski diagram*, named after Professor Alexander Jablonski. In this diagram singlet states are depicted by S_i while triplet states by T_j with S_0 being the ground state. For each electronic energy level, numerous vibrational energy levels can exist. The transitions between the states are depicted as arrows starting from the initial state to the final one.
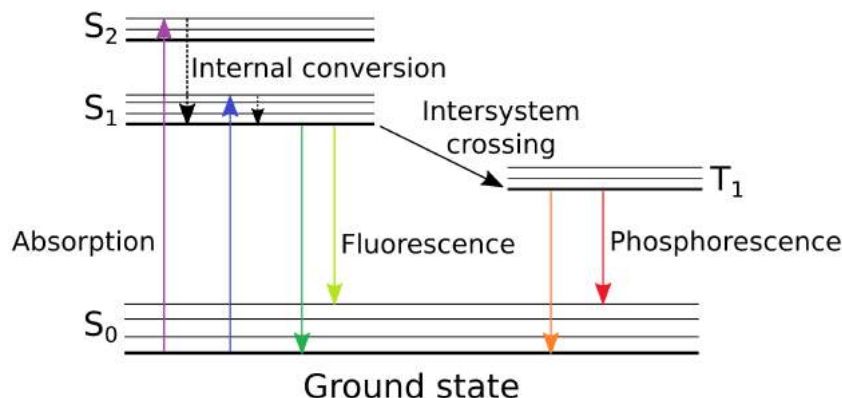

Figure 2.12: Example of Jablonski diagram in which solid colored lines represent radiative decays (photon absorption/emission) and black lines non-radiative decays (solid one intersystem crossing, dotted ones relaxation)

From the diagram in Figure 2.12 it can be inferred that the emission energy is always lower than that of absorption, explaining why the fluorescence spectrum is red shifted compared to the absorption one.

Even tough absorption typically involves one photon at a time, *multiphoton excitation* is in certain conditions possible. If the intensity of a laser is high enough, a fluorophore can simultaneously absorb two long-wavelength photons to reach the first singlet state. Clearly, such intensities would normally destroy the sample, so a femtosecond pulsed laser is required. The advantage of such technique is the excitation of the sample in the spot where the light is focused, reducing the absorption by the out-of-focus molecules.

It is important to acknowledge that an absorbed photon will not always lead to a radiative decay, because non-radiative transitions are possible. In presence of a certain environment, for example, the fluorophore may have the chance of transferring the energy of the electron in the excited state to other molecules or particles nearby. This process is called *quenching* and has the effect of reducing the efficiency of the radiative process. Even tough typically regarded as detrimental, quenching may be useful in applications like molecular imaging and FRET (*Förster resonance energy transfer*). Quenching is described by the *Stern-Volmer relationship*:

$$\frac{I_0}{I} = 1 + k_q \tau_{\bar{q}} [Q] \tag{2.50}$$

where I_0 is the fluorescence intensity in the absence of a quencher, I the intensity in presence of a quencher, k_q is the quencher rate coefficient, $\tau_{\bar{q}}$ the unquenched lifetime of the fluorophore and $[Q]$ is the concentration of the quencher.

Every process, either radiative or non-radiative, will have an occurrence probability and therefore a certain *decay rate*. As shown in Figure 2.13, the radiative emission rate is depicted with Γ, the non-radiative decay rate with k_{nr} and the quenching rate with k_q.
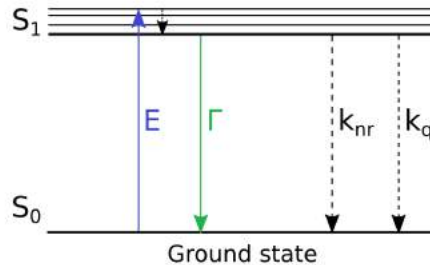

Figure 2.13: Radiative and non-radiative decay processes in a fluorophore

The efficiency of the radiative process is called *quantum yield* (or quantum efficiency) Q_0:

$$Q_0 = \frac{\Gamma}{\Gamma + k_{nr} + k_q} \tag{2.51}$$

The quantum yield is zero when none of the absorbed photons gets re-emitted, and one when there are no non-radiative losses.

The *lifetime* τ_0 of the fluorophore is given by:

$$\tau_0 = \frac{1}{\Gamma + k_{nr} + k_q} \tag{2.52}$$

When speaking about typical fluorophores, the drawbacks can be numerous and limiting:

- **Low quantum efficiency**: the radiative decay is not the most favorite, reducing the total fluorescence intensity;

- **Photobleaching**: after a finite number of photocycles the fluorophore changes chemical properties and loses its ability to fluoresce;

- **Autofluorescence**: some proteins are weakly fluorescent by nature, therefore introducing optical noise in biological systems;

- **Lack of specificity**: certain proteins are expressed everywhere in the cell membrane, so subcellular compartments are more difficult to locate;

Chemical modifications to the surrounding environment can have a little positive impact on some fluorescence's parameters, but the recent employment of metallic nanostructures has opened the door to novel opportunities in biotechnology.

Mechanism of MEF

Most of the literature regarding metal-enhanced fluorescence (MEF) appeared in the past few years, but its origin dates back to 1974 when Karl H. Drexhage first observed it. His pioneering work demonstrated the possibility of altering the lifetime of an europium complex near a planar metal surface [31]. Just as many new scientific discoveries, the complex mechanisms of MEF are not completely understood and the theory behind them is still debatable. For now what is generally accepted is that there are at least three mechanisms that compete in MEF, strongly dependent of the distance between the fluorophore and the nanoparticle:

- $0 - 5nm$ **Fluorophore quenching**:

  At short distances the nanoparticle will act as a quencher, since the dipolar oscillations of the fluorophore are damped by the nearby metal. This effect highers k_q and is reflected in equations (2.51) and (2.52) with a lower quantum efficiency as well as a lower lifetime.

- $0 - 15nm$ **"Lightening Rod" effect**:

  As showed in equation (2.42), the local electric field nearby the metallic nanoparticle can present a higher intensity. If a fluorophore is positioned in the enhancement region resonant with the excitation wavelength, the intensity of light will be highly concentrated and so more photons will be absorbed by the fluorescent molecule.

- $0 - 20nm$ **Increase in the radiative decay rate**:

  Modifications of the radiative decay rate Γ are usually not considered, because this rate is determined by the probability of the $S_1 \rightarrow S_0$ transition. When placed at a suitable distance from the metallic nanoparticle, the fluorophore can however show an additional radiative decay rate Γ_m, due to the interaction with the metal, such as equations (2.51) and (2.52) become:

  $$Q_m = \frac{\Gamma + \Gamma_m}{\Gamma + \Gamma_m + k_{nr} + k_q}, \qquad \tau_m = \frac{1}{\Gamma + \Gamma_m + k_{nr} + k_q} \qquad (2.53)$$

  Control over Γ_m can lead to modifications in both quantum yield and lifetimes, if the nanoparticle's parameters are properly tuned.
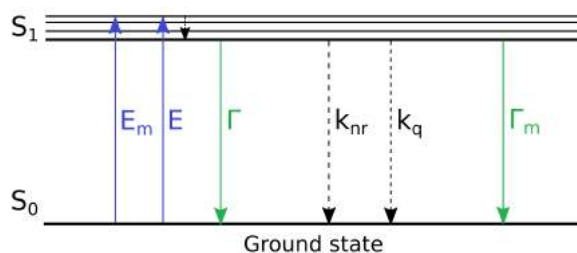

Figure 2.14: Jablonski diagram of MEF

MEF finds its roots in modifications to the photonic *Local Density Of States* (LDOS), the density of accessible states at each level of energy. The process can be understood and evaluated using time-dependent perturbation theory and more specifically *Fermi's golden rule*[4]:

$$\Gamma \propto \left| < g|\vec{E} \cdot \vec{D}|e > \right|^2 \rho_g \qquad (2.54)$$

where $|g>$ and $|e>$ are the ground and the excited states, $\vec{E}$ is the local electric field, $\vec{D}$ is the molecular dipole moment and ρ_g is the final photonic LDOS. In presence of a metallic nanoparticle the LDOS and the local electric field are much higher, resulting in the Γ_m contribution to Equation (2.53) and leading to the definition of an enhanced quantum yield Q_m.

From (2.51) and (2.53) it is possible to see that molecules with low natural quantum yield Q_0 are the most enhanced when in the proximity of a metallic nanoparticle. Fluorophores with $Q_0 \approx 1$ already present a high Γ, so the addition of Γ_m has less impact on photonic emission.

Despite several experiments have been carried out trying to completely determine the LDOS of metallic nanostructures [32][33], the description of Γ_m in relation with the nanoparticle's features (size, shape, material) is still quite limited.

An alternative newer interpretation, the *radiating plasmon model* [34], considers a non-radiative resonant energy transfer from the fluorophore to the surface plasmon electrons, which in turn radiate at a certain wavelength. Scattering component of the resonance is therefore responsible for fluorescence enhancement.

2.4 Finite-Difference Time-Domain (FDTD) simulations

All the analytical treatment developed in the previous sections has been focusing on spheres and ellipsoids, but with the help of nanochemistry and nanofabrication almost any kind of imaginable shape can be produced. While some features can be naively approximated to the previous cases, sharp edges and amorphous protuberances reflect in unique features not predicted by the theory. The only way to get reliable results is then the employment of numerical methods that in some way solve Maxwell's equations.

The most popular simulation techniques used in the field of plasmonics are the Finite-Difference Time-Domain (FDTD), the Finite-Difference Frequency-Domain (FDFD), the Discrete Dipole Approximation (DDA) and the Boundary Element Method (BEM). Each has advantages and drawbacks, so the right one has to be chosen depending on the desired application.

In this thesis only FDTD has been employed, because of its powerful features and the very limited number of approximations involved. This section will briefly focus on the fundamental principles of the FDTD simulation technique.

The *Finite-Difference Time-Domain* (FDTD) method was invented by Kane S. Yee, who published a paper about it in 1966. His approach concerned the approximate solution of Maxwell's equations by the discretization of space and time and the use of the *central difference approximations* for the curl equations. For the first time, Yee's method enabled a second-order accuracy in the results. For almost ten years this technique remained theoretical, because at that time there were no computers powerful enough to perform such three-dimensional calculations. From the first use in numerical simulations in the late '70s, FDTD continued growing up to what we now recognize as one of the easiest and yet most versatile simulation tool.

2.4.1 Yee algorithm for Maxwell's equations

Maxwell's equations in matter

The foundations of classical electromagnetism inside macroscopic materials are undoubtedly the four *Maxwell's equations*, which completely describe the behaviour of electric and magnetic fields in matter:

$$\vec{\nabla} \cdot \vec{D} = \rho_f \tag{2.55}$$

$$\vec{\nabla} \cdot \vec{B} = 0 \tag{2.56}$$

$$\vec{\nabla} \times \vec{E} = -\frac{\partial \vec{B}}{\partial t} \tag{2.57}$$

$$\vec{\nabla} \times \vec{H} = \vec{J}_f + \frac{\partial \vec{D}}{\partial t} \tag{2.58}$$

where the first two are called *divergence equations* and the last two are called *curl equations*. To these, the *constitutive relations* that describe the material have to be added:

$$\vec{D} = \epsilon_0 \epsilon \vec{E} \tag{2.59}$$

$$\vec{H} = \frac{1}{\mu_0 \mu} \vec{B} \tag{2.60}$$

If there are no free charges nor free currents (which is usually the case in plasmonics):

$$\rho_f = 0, \qquad \vec{J}_f = 0 \tag{2.61}$$

Putting all the previous equations together, the curl equations simplify to:

$$\vec{\nabla} \times \vec{E} = -\mu_0 \mu \frac{\partial \vec{H}}{\partial t} \tag{2.62}$$

$$\vec{\nabla} \times \vec{H} = \epsilon_0 \epsilon \frac{\partial \vec{E}}{\partial t} \tag{2.63}$$

When discretized, those equations can iteratively be solved to get $\vec{E}$ and $\vec{H}$. It is more useful to look at the projections of the equations on the three main cartesian axes:

$$\mu_0 \mu \frac{\partial H_x}{\partial t} = \frac{\partial E_y}{\partial z} - \frac{\partial E_z}{\partial y} \tag{2.64}$$

$$\mu_0 \mu \frac{\partial H_y}{\partial t} = \frac{\partial E_z}{\partial x} - \frac{\partial E_x}{\partial z} \tag{2.65}$$

$$\mu_0 \mu \frac{\partial H_z}{\partial t} = \frac{\partial E_x}{\partial y} - \frac{\partial E_y}{\partial x} \tag{2.66}$$

$$\epsilon_0 \epsilon \frac{\partial E_x}{\partial t} = \frac{\partial H_z}{\partial y} - \frac{\partial H_y}{\partial z} \tag{2.67}$$

$$\epsilon_0 \epsilon \frac{\partial E_y}{\partial t} = \frac{\partial H_x}{\partial z} - \frac{\partial H_z}{\partial x} \tag{2.68}$$

$$\epsilon_0 \epsilon \frac{\partial E_z}{\partial t} = \frac{\partial H_y}{\partial x} - \frac{\partial H_x}{\partial y} \tag{2.69}$$

Central difference approximation

The key feature in the Yee algorithm is the use of the central difference approximation of the first order partial derivative. If a function f is C^∞-continuous, then its Taylor series expansions around the points $x + \Delta x/2$ and $x - \Delta x/2$, with Δx arbitrarily small, are:

$$f\left(x + \frac{\Delta x}{2}\right) = f(x) + \frac{\partial f}{\partial x}\frac{\Delta x}{2} + \frac{1}{2}\frac{\partial^2 f}{\partial x^2}\left(\frac{\Delta x}{2}\right)^2 + \frac{1}{3!}\frac{\partial^3 f}{\partial x^3}\left(\frac{\Delta x}{2}\right)^3 + \dots \tag{2.70}$$

$$f\left(x - \frac{\Delta x}{2}\right) = f(x) - \frac{\partial f}{\partial x}\frac{\Delta x}{2} + \frac{1}{2}\frac{\partial^2 f}{\partial x^2}\left(\frac{\Delta x}{2}\right)^2 - \frac{1}{3!}\frac{\partial^3 f}{\partial x^3}\left(\frac{\Delta x}{2}\right)^3 + \dots \tag{2.71}$$

Then:

$$\frac{f(x + \frac{\Delta x}{2}) - f(x - \frac{\Delta x}{2})}{\Delta x} = \frac{\partial f}{\partial x} + \frac{\Delta x^2}{24}\frac{\partial^3 f}{\partial x^3} + ... \tag{2.72}$$

Rearranging the terms:

$$\frac{\partial f}{\partial x} \approx \frac{f(x + \frac{\Delta x}{2}) - f(x - \frac{\Delta x}{2})}{\Delta x} + O(\Delta x^2) \tag{2.73}$$

The leading order error goes down as Δx^2, so the approximation is said to have second order accuracy. The smaller Δx, the better the precision of this approximation.

Discretization of Maxwell's equation

Consider a three-dimensional uniform rectangular grid in which every cell (named *Yee cell*) has sides of length $\Delta x, \Delta y, \Delta z$ along each cartesian axis. Similarly, time is discretized in steps of duration Δt. The coordinates of a node in the grid at a certain time (x, y, z, t) can be expressed in terms of $(i\Delta x, j\Delta y, k\Delta z, n\Delta t)$ where i, j, k, n are integers.

A more elegant notation to express any arbitrary function in the discretized space is:

$$f(x, y, z, t) = f(i\Delta x, j\Delta y, k\Delta z, n\Delta t) = f_{i,j,k}^n \tag{2.74}$$

The most natural way to sample the projections of the fields has to be consistent with the central difference approximations: considering a Yee cell, the electric fields $\vec{E}$ are then sampled at center of grid edges, while the magnetic fields $\vec{H}$ are sampled at the center of grid faces.
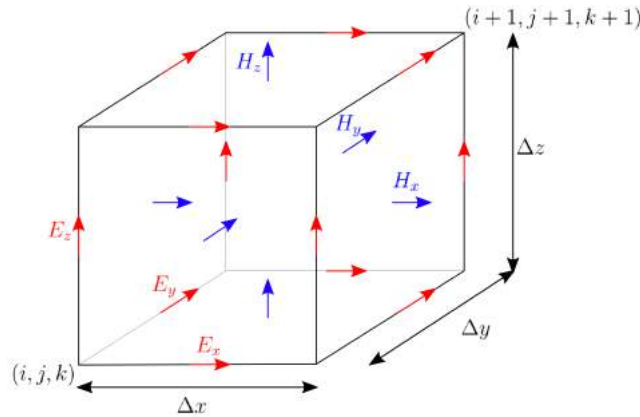

Figure 2.15: Yee cell

Employing equation (2.73) in the partial derivatives appearing in curl equations, their discrete forms can be obtained. For example, equations (2.64) and (2.67) become:

$$\mu_0\mu\left(\frac{H_{x_{i,j+\frac{1}{2},k+\frac{1}{2}}}^{n+1} - H_{x_{i,j+\frac{1}{2},k+\frac{1}{2}}}^{n}}{\Delta t}\right) = \frac{E_{y_{i,j+\frac{1}{2},k+1}}^{n+\frac{1}{2}} - E_{y_{i,j+\frac{1}{2},k}}^{n+\frac{1}{2}}}{\Delta z} - \frac{E_{z_{i,j+1,k+\frac{1}{2}}}^{n+\frac{1}{2}} - E_{z_{i,j,k+\frac{1}{2}}}^{n+\frac{1}{2}}}{\Delta y} \tag{2.75}$$

$$\epsilon_0\epsilon\left(\frac{E_{x_{i+\frac{1}{2},j,k}}^{n+\frac{1}{2}} - E_{x_{i+\frac{1}{2},j,k}}^{n-\frac{1}{2}}}{\Delta t}\right) = \frac{H_{z_{i+\frac{1}{2},j+\frac{1}{2},k}}^{n} - H_{z_{i+\frac{1}{2},j-\frac{1}{2},k}}^{n}}{\Delta y} - \frac{H_{y_{i+\frac{1}{2},j,k+\frac{1}{2}}}^{n} - H_{y_{i+\frac{1}{2},j,k-\frac{1}{2}}}^{n}}{\Delta z} \tag{2.76}$$

The discretized equations can be rewritten so as to calculate explicitly the fields at later instants. This is the so called *leapfrog* manner of solving Maxwell's equations, meaning that $\vec{E}$ and $\vec{H}$ are not known at the same time nor at the same position:

$$\vec{E}^{-\frac{1}{2}} \rightarrow \vec{H}^0 \rightarrow \vec{E}^{\frac{1}{2}} \rightarrow \vec{H}^1 \rightarrow \vec{E}^{\frac{3}{2}} \rightarrow \vec{H}^2 \rightarrow ... \tag{2.77}$$

The initial conditions are usually set to 0, except for the sources that are created as regions in which the fields are forced to assume certain values in time and space. In principle it is true that the finer is the *mesh* (in other words, the choice of $\Delta x, \Delta y, \Delta z$) the higher the precision will be. In practice, interfaces not properly meshed may create artifacts that are unphysical. Time step is not set by the user but automatically chosen to minimize the error:

$$\Delta t = \frac{1}{c_{max}} \frac{CFLN}{\sqrt{\frac{1}{\Delta x^2} + \frac{1}{\Delta y^2} + \frac{1}{\Delta z^2}}} \tag{2.78}$$

where c_{max} is the maximum wave speed in the problem domain and $CFLN$ is the so called *Courant-Fredrichs-Lewy number*. For guaranteeing the stability of the algorithm $CFLN < 1$, so usually it is chosen to be very close to 1 (for example, $CFLN = 0.99$).

2.4.2   FDTD's strengths and limitations

Just like all numerical methods, FDTD has both advantages and weaknesses. The strengths can be summarized as follows:

- Intuitive and easy to understand;

- Versatile, does not introduce other approximations other than the mesh size;

- Time-domain technique that can give broadband results with a single simulation;

- Compatible with both linear and nonlinear materials;

- Directly returns the physical fields, from which every other quantity can be calculated.

On the other hand, it is important to understand FDTD's limitations:

- The full discretization of space, even when empty or homogeneous, is not always efficient;

- Fine spatial mesh imposes a small time step, leading to a large number of iterations;

- Not efficient for continuous wave simulations;

- Orthogonal gridding is inaccurate for curved surfaces which require the implementation of local non-uniform mesh;

- Far-field simulations require additional post-processing.

Since in the experiments we don't have an *a priori* knowledge of the plasmonic resonances especially related to shape effects, broadband simulations are the right tool to design and optimize nanoparticles. Long simulation time is not a problem either, having a dedicated computer for that purpose.

Chapter 3

Materials and methods

An extensive part of my work has been focused on the production of plasmonic nanoparticles and the control of their optimal features such as shape, size and distance from the fluorophores. This chapter will indeed cover the practical details regarding either the simulations and the experimental work carried out during this time. Because of its inertness and optical properties, gold has been identified as the only material suitable for our biological application, therefore very little time was spent on the study of alternatives. After characterizing the different nanoparticles, they have been employed on HEK cells as a proof of principle of the genetically encoded voltage indicators' fluorescence enhancement.

Section 1 will outline the computational approach to the problem, the chosen features of the nanoparticles and the imposed boundary conditions.

Section 2 will explore the production of nanoparticles by electron beam lithography, the first technique tested. Pros and cons of this nanofabrication technology are highlighted as well.

Section 3 will cover the synthesis of colloidal nanoparticles, which is more compatible with the final application in electrophysiology.

Section 4 will briefly illustrate how SEM inspection has been employed to morphologically characterize the previously produced nanoparticles.

Section 5 will focus on UV-Vis spectroscopy and its application to the optical characterization of our colloidal solutions.

Section 6 will highlight the imaging techniques involved in the investigation of the interaction between fluorophores and gold nanoparticles.

Section 7 will ultimately explain the basic principles of patch clamp and how it has been used to control the membrane potential.

3.1 FDTD simulations

As already stated in Chapter 2, the plasmonic resonance of metallic nanostructures is strongly size and shape dependent, meaning that it is not possible to know *a priori* the ideal parameters for a certain purpose. A preliminary computational approach is then essential to avoid the long trial-and-error procedure normally carried out in these kind of studies. Nonetheless, plasmonic resonance's tunability in simple conditions is already known [35] [36], so the optimization of the parameters started from an extensive literature review.

Due to their properties and relative easiness of their production process, spheres, rods and stars were chosen as suitable shapes to start with in the simulations. The software used for this preliminary study was *Lumerical's FDTD Solutions* [37], a computational tool capable of simulating arbitrarily complex geometries with an user-friendly interface.

The choice of using the *Finite-Difference Time-Domain* algorithm over other computational approaches is supported by the need of a minimum number of approximations altogether with the direct computation of the physical fields (electric and magnetic). More information regarding the theoretical basis of this method can be found in Section 2.4 of this thesis.

I simulated three different geometries: spheres, rods and stars. These shapes were chosen because of the tradeoffs between the ease of theoretical understanding and their applicability to our biological systems:

- **Spheres**: they are easily created through colloidal synthesis, easy to simulate and relatively easy to understand intuitively, however they end up being sub-optimal for high localized field enhancement;

- **Rods**: roughly approximated as unidimensional, they are intuitive to understand. They can exhibit strong directional field enhancement, which is precisely tunable by changing the aspect ratio between the sides, but they are difficult to make using colloidal synthesis;

- **Stars**: probably one of the most anisotropic morphologies, nanostars show incredibly strong field enhancement localized nearby the spikes' tips [38]. Because of their non-trivial nature, no analytical models can be easily developed to predict their plasmonic behaviour. Simulations are therefore fundamental in the earliest stages of characterization. Their colloidal synthesis can be tricky, especially when trying to obtain monodispersed colloids, but they potentially offer superior field enhancement.

The simulations' goal was both to optimize the features of the nanoparticles beforehand and to formulate *a posteriori* explanations of the results obtained. In certain cases, simulation results were also a check of what was known from theory and literature.

Special care has to be given to the monitored features when simulating plasmonic nanoparticles: in certain cases absorption and scattering cross sections are crucial, in some others maximum or average electric field enhancement is more significant, in few others temporal dynamics gives a deeper understanding of the physical processes happening. Since the purpose of this thesis is to enhance the fluorescence emitted by proteins in the cell membrane, whose positions and orientations are impossible to precisely control, the optimized feature was the average field enhancement in a volume some nanometers away from the nanoparticle's surface. In this way we can avoid misleading results due to isolated voxels of insanely high enhancement or regions inaccessible to the fluorophores. Moreover, the choice of looking for enhancement few nanometers away from the plasmonic particle ensures negligible quenching effects (for more information regarding the fluorophore-nanoparticle interaction see Section 2.3.5).

The following topics will be briefly explained:

- Simulation parameters

- Materials

- Morphologies

- Sources

All the parameters and monitors have been set through custom made scripts that are available in Appendix B.
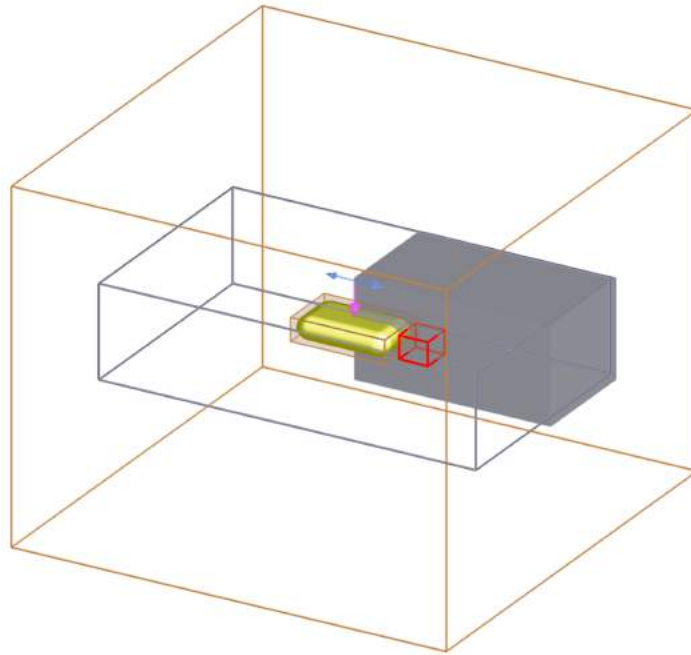
Figure 3.1: FDTD simulations' main components: in gold the particle, in light brown the simulation region and the finer mesh around the particle, in gray the TFSF source, in red the 3D monitor. The magenta arrow indicates the direction of the electromagnetic wave and the blue double arrow the direction of oscillation of the electric field.

Simulation parameters

The choice of the many technical parameters plays a crucial role in a significant and reliable simulation of the system. The plasmonic nanoparticles have been studied in a three-dimensional environment, with the *simulation region* set to be large enough to ensure no exponential field reflected at the boundaries. This usually translates to setting the FDTD region's span to the maximum wavelength plus the nanoparticle's diameter. With this condition the boundaries artificially act like perfectly absorbing materials, meaning that a wave passing through them is the same as it propagating through an open boundary towards infinity.

The *simulation time* is typically set so as to let the system evolve while guaranteeing a truncated loop in case of unphysical conditions. Usually, for plasmonic nanoparticles $200 fs$ is a more than sufficient simulation time to ensure the convergence of the simulation. As the energy sent by the source is absorbed by the boundaries, the total residual energy is continuously calculated; if this energy is less than 10^{-5} of the total, early shutoff occurs. All these conditions limit the length of the simulations without significantly affecting the results.

As far as the *boundary conditions* are concerned, all the considered particles were single entities isolated in the medium. In order to make the simulation more efficient, on x and y axes symmetry has been employed: in particular, x boundary was set as anti-symmetric and y boundary as symmetric. The difference between symmetry and anti-symmetry relies only on the direction of the electric field. It is important to note that the z dimension was not symmetric due to the presence of the wave source. All the surrounding boundaries have been set as perfectly absorbing materials, also known as *Perfectly Matched Layers* (PML).

In Section 2.4 the importance of using a fine *mesh grid* (Δx, Δy, Δz) to discretize the three-dimensional space has been highlighted. The employed software supports the non-uniform gridding option which optimizes the mesh size depending on the shape of the simulated objects. The general accuracy has always been set between medium and very high, in order to keep the

expected simulation time in a reasonable range. To accurately model the non-flatness of the nanoparticles' surface, an extra fine uniform mesh grid was introduced inside the TFSF source containing the object under study. In this way, the boundary between water and gold was faithfully reproduced without abrupt changes that could generate significant artificial hotspots. The criterion adopted in the automatic choice of the finest mesh size is the smallest feature's dimension divided by a factor between 10 and 30, resulting in steps of fractions of nanometers. Under a certain accuracy, the simulation only becomes longer and heavier without adding value to the results, especially considering that the real surface will never be infinitely smooth.

It should be noted that artifacts will always be present when modeling curved surfaces, no matter how fine the mesh size is. These artificial hotspots highlight one of the few weaknesses of the FDTD algorithm, but they can be neglected by simply not including them in the monitors. In this case, the finer the mesh the less voxels will be unphysical.
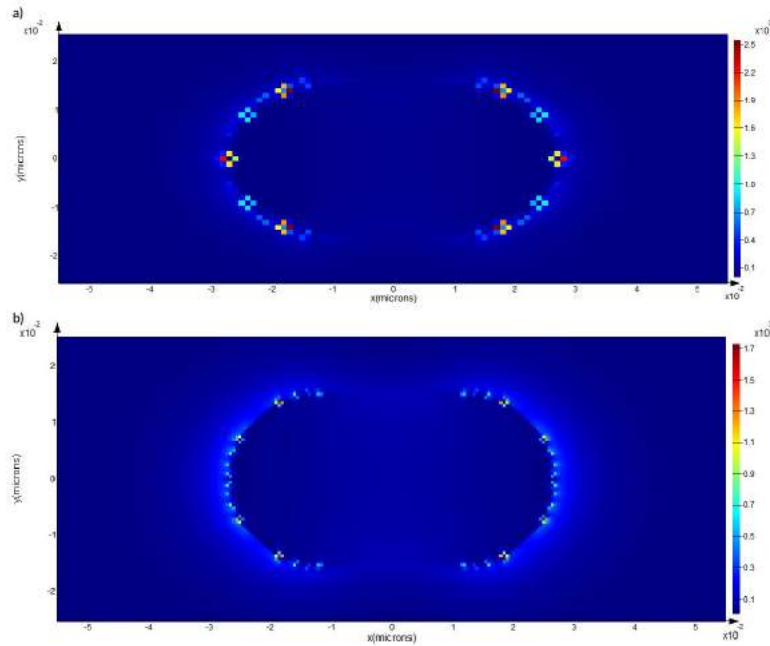

Figure 3.2: Comparison of artifacts in field enhancement due to the mesh size

The stability factor (also called *Courant-Fredrichs-Lewy number*) is automatically set to 0.99 and the time step Δt is computed following Equation (2.77) using the smallest Yee cell.

Depending on the information sought, two main *monitor* types have been employed. For most simulations a 3D power monitor was placed $4nm$ away from the nanoparticle's surface, along the direction of the electric field. The choice of this spacing distance is either for discarding artifacts and for considering the future use of nanoparticles functionalized with specific linkers. Furthermore, the fluorescence quenching effect has to be avoided while maximizing the field enhancement effect. Average field enhancement was chosen over maximum since the position of the nanoparticle in respect to the protein is not entirely controllable. The span of this 3D monitor was set as a function of the nanoparticle size. The average field enhancement was calculated for each wavelength and the peak corresponding to its highest value saved in a text file. A set of parameters is considered optimal when the peak of the average field enhancement is at the same wavelength of the emission peak of the fluorescent protein (specifically, $680nm$).

In few cases the absorption and scattering cross sections have been checked by employing the built-in tool in order to quantitatively compare the effects of the two processes at the desired wavelength. Indeed, a predominant absorption of the radiation leads to a disruptive quenching of the fluorescence, as explained in Section 2.3.5 of this thesis.

Materials

As far as the involved materials are concerned, all the simulated nanoparticles had gold-like complex dielectric function and were surrounded by pure water. The fitting routine attempts to find an analytical function that satisfy a certain tolerance value using the fewest number of model coefficients.

Although the optical parameters of biological materials are much more complex than just water, for all practical purposes they are transparent under white light and barely absorb radiation in the visible spectrum. In any case, it would not be possible nor useful to explicitly describe the surrounding watery environment in terms of biological materials, since the arrangement of the cell with respect to the nanoparticle is unpredictable. Water has been simulated by fitting the data in Palik's Handbook of Optical Constants of Solids [39] using the built-in fitting tool. The model function uses 2 coefficients and a 0 fit tolerance. It should be noted that the error between the fitted curve and the data is at most 2%.
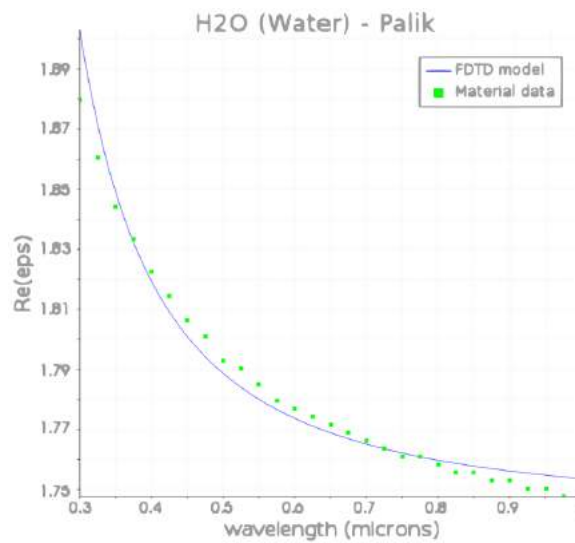

Figure 3.3: Fit of water's dielectric function (ϵ_1 plotted, $\epsilon_2 = 0$) using the built-in tool

Bulk gold's complex dielectric function has been fitted from data contained in CRC Handbook of Chemistry and Physics [40] using the built-in fitting tool. The same functions have been used consistently in each simulation, with the use of 11 coefficients and setting a 0 fit tolerance.
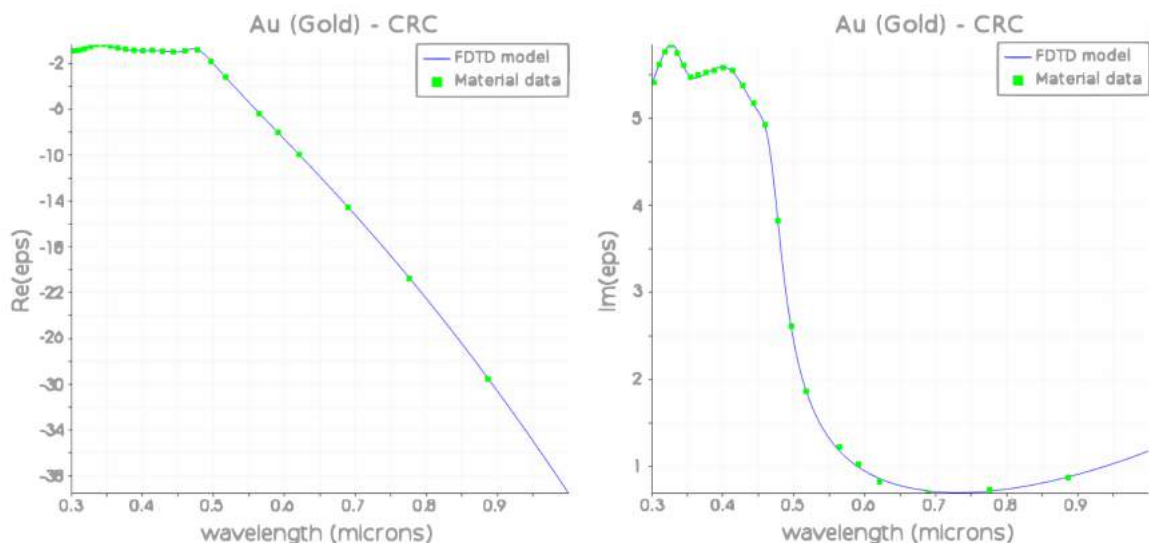

Figure 3.4: Fit of gold's complex dielectric function (ϵ_1 left, ϵ_2 right) using the built-in tool

37

Morphologies

Different shapes have been explored and carefully modeled so as to avoid misleading artifacts. Spheres and rods were simulated in advance to find the optimal parameters (namely size, aspect ratio and smoothness of the edges), while stars were studied *a posteriori* basing their morphology on the realistic one found at the SEM.

All the parameters have been set through custom made scripts and loops were involved to carry out parametric sweep studies. For spheres and stars, the influence of core radius on field enhancement was varied in a realistic range; as far as rods are concerned, all the three sides were varied independently in a wide range. Plasmonic nanoparticles with a resonance wavelength higher than $800nm$ were discarded being out of the scope of this thesis.

Since some preliminary simulations showed that infinitely sharp edges or tips could generate unphysical artifacts, smoothed shapes already available in the software's object library were used. Moreover, it is unlikely to obtain such sharpness with the fabrication methods employed.
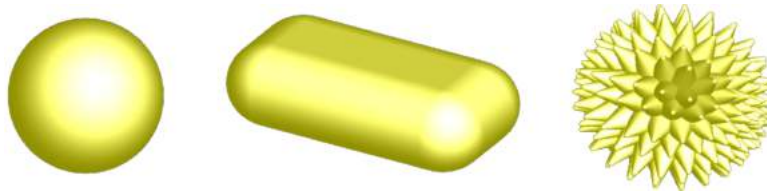

Figure 3.5: 3D rendering of simulated shapes

Sources

The only type of source used in the simulations was the *Total-Field Scattered-Field* (TFSF), a useful tool for studying stand-alone objects. This virtual box sends a plane wave along the desired direction and isolates the scattered field from the total one. In this way, the scattered field can pass through the box and be detected outside of it [41]. This tool makes the study of scattering and absorption cross section easy, while keeping the fields physical inside the box (where the power monitors are). A single broadband pulse is sufficient for studying the range of interest, in the depicted case $300nm - 1000nm$; the pulse is automatically optimized to be as short as possible. To work well, the TFSF source requires a uniform mesh grid inside it.
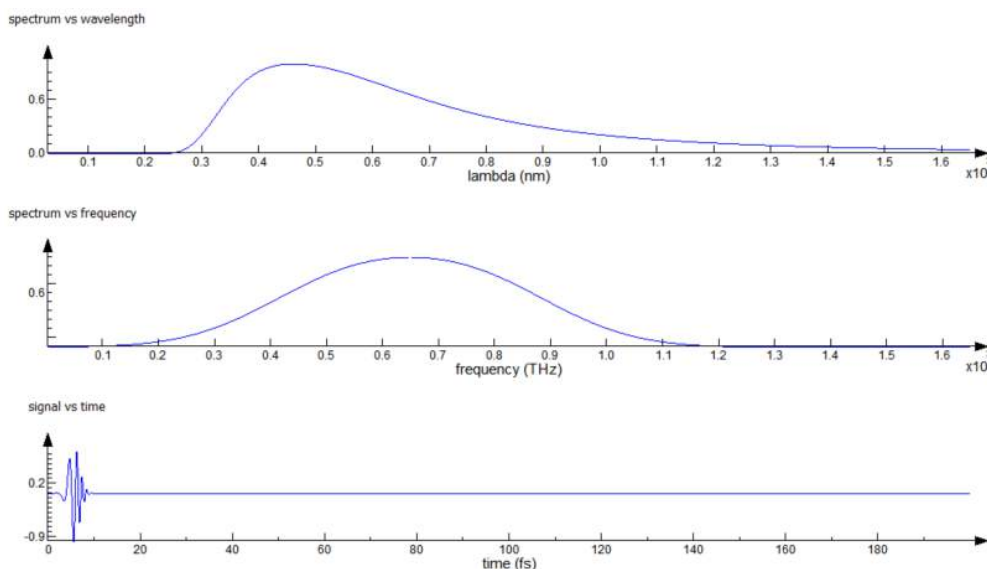

Figure 3.6: Frequency and time domain of the sent pulse

3.2 Electron beam lithography (EBL)

Since the first simulations, it has become clear that a fabrication tool with nanometric resolution was needed in order to produce particles with highly customized details. In particular, the strongest plasmonic resonance at the desired wavelength ($680nm$) was predicted in nanorods having size approximately of $65nm$ x $40nm$ x $20nm$. Even with the current state-of-the-art *photolithography* tools the diffraction limit makes it impossible to achieve such resolution, so a different technique had to be used.

The idea behind *electron beam lithography* (EBL) is then to use a focused beam of electrons, instead of photons, to write a pattern on a sensitive thin polymeric film, called *resist* [42][43]. The interaction between high energy electrons and the resist locally alters its solubility in certain organic solvents. The process is said to be *positive-tone* if the exposed material is removed and *negative-tone* if the unexposed material is. By scanning the electron beam using electric or magnetic fields and turning it on and off, virtually any arbitrary pattern can be imprinted in the resist. The so-obtained binary mask presents nanometric patterns and can be further used to selectively deposit other materials, like gold in our case.

While the ideal resolution is limited by the de Broglie electron wavelength ($\lambda = h/p = 8pm$ for $25kV$), uncontrollable interactions such as scattering and secondary processes bring the actual resolution to a few nanometers. One of the main drawbacks of this tool is the low throughput, due to the slow writing speed. In fact, being EBL a scanning technique, typical machines operate in the best conditions at $1cm^2/s$. Writing current happens to be a limitation to resolution as well.

Figure 3.7: Scheme of the whole positive-tone process
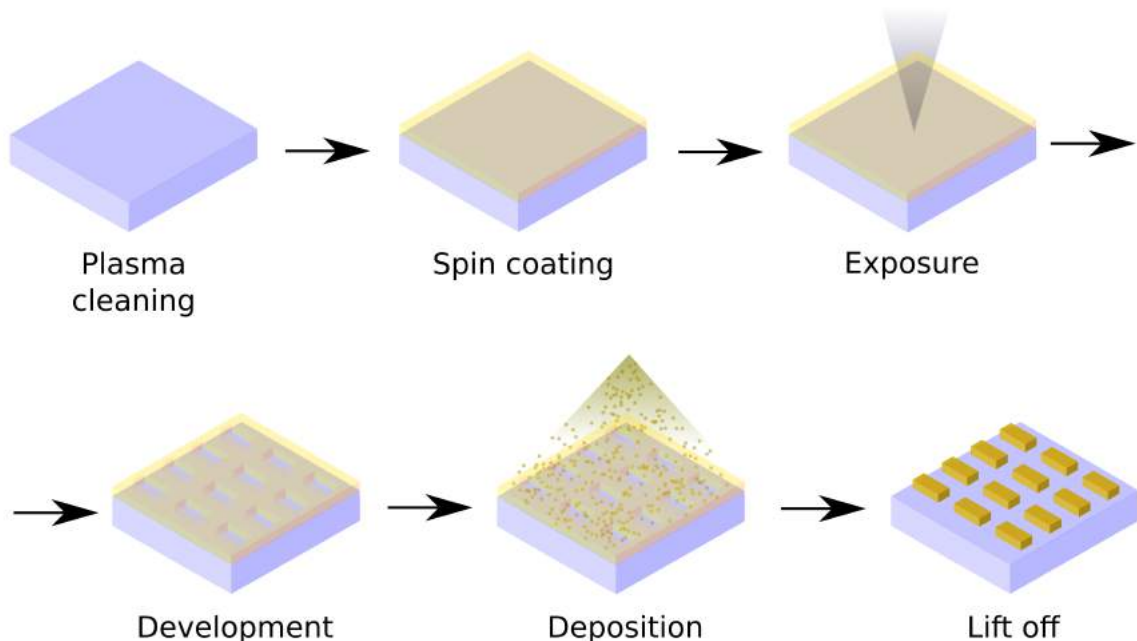
The general process followed for positive-tone EBL is schematically presented in Figure 3.7 and explained hereafter:

1. **Plasma cleaning**: the conductive substrate is typically cleaned with an oxygen plasma so as to remove eventual carbon contamination;

2. **Spin coating**: a thin layer of polymeric resist is spin coated on the substrate and baked to make it solid;

3. **Exposure**: the coated substrate is fixed inside the EBL system, put under high vacuum and written on with the electron beam;

4. **Development**: the solubilized polymer is removed by using specific chemicals (dependent on the resist) and dried;

5. **Deposition**: a thin layer of the desired material is uniformly deposited by sputtering;

6. **Lift off**: the undeveloped resist (covered with the deposited material) is removed using stronger chemicals; the nanodevice is finally ready to be used.

As the involved materials are sensitive to the UV component in the environmental light and even a speckle of dust can detriment nanometric resolution, all the steps are typically carried out in a cleanroom. To grant higher precision, a two-layer polymeric resist was employed.

The produced gold nanoparticles are designed specifically to be used on biological fluorescent samples in an optical microscope, so the substrate has to be transparent in the visible spectrum. Furthermore, the exposure step requires a conductive substrate to work properly, so in the end *indium tin oxide* (ITO) coated glass samples were used to fulfill both the requirements.

After several attempts (see Section 4.2 for more information), the final protocol tested was the following:

1. Clean the ITO covered glass substrates (size $22mm$ x $22mm$ x $0.550mm$) with an oxygen plasma;

2. Spin coat the bottom layer of PMMA $495K$ 4% diluted $1:1$ in anisole, at $3000rpm$ to get a thickness of about $50nm$;

3. Bake for $30min$ at $180°C$;

4. Spin coat the top layer of PMMA $950K$ $A2$ 2%, at $10000rpm$ to get a thickness lower than $50nm$;

5. Bake for $30min$ at $175°C$;

6. With an electron beam evaporator (Temescal) deposit $10nm$ of chromium on top of the resist;

7. Expose the sample with the electron beam (dose $1200mJ/cm^2$, beam current $198pA$);

8. Wet etch chromium for $30s$, rinse in water and dry in oven at $120°C$;

9. Develop in MIBK diluted $1:3$ IPA, stop the reaction in IPA;

10. Sputter a thin homogeneous layer of gold for a total thickness of $20nm$;

11. Lift off the remaining resist in PRS.

The thin layer of chromium is necessary to make the surface flat, so the EBL machine can easily find a plane where to focus the beam; skipping the height check could lead to imprecise and uncontrollable exposure of the polymer.

It is important to note that the recipe is still under testing and will be subject to future improvements, as the final result is not exactly the expected one (see Section 4.2 for more details regarding the obtained nanopatterns).

3.3 Colloidal synthesis

A *colloid* is defined as "any substance consisting of particles substantially larger than atoms or ordinary molecules but too small to be visible to the unaided eye" [44]. More specifically, when used in this thesis the term refers to a collection of gold nanoparticles of any shape, with overall size between $10nm$ and $200nm$, dispersed in a structureless solvent. Nanoparticles in a colloidal solution are usually stabilized with capping agents and can be *functionalized* with molecules so as to strongly interact with specific substances (for example, they can be uniquely linked to certain membrane proteins in cells).

Compared to EBL, *colloidal synthesis* is fundamentally an higher-throughput and faster technique more suitable for further functionalization. As soft matter science progresses, synthesis' protocols become more varied and reliable, allowing in many cases to obtain monodispersed nanoparticles in solution. The great tunability of such colloids makes their applications very flexible and general. Nowadays, a wide variety of anisotropic morphologies can be achieved, going from nanocubes to highly-branched nanostars [45][46].

In general, two main categories of wet chemistry-based approaches exist:

- **One-pot synthesis**: involves the growth from metallic nuclei to spherical seeds and, eventually, bigger particles. It is based on the addition of metal atoms directly to the nuclei and so resulting unsuitable in the making of anisotropic nanoparticles;

- **Seed-mediated synthesis**: metal atoms selectively deposit on pre-formed spherical seeds thanks to surface passivation or kinetic control, in a multiple step process.

It should be noted that metal colloids are rarely straightforward to synthesize. Indeed, they involve long trial-and-error experiments to finely tune the plasmonic resonance and to prevent low reproducibility due to random fluctuation of parameters like chemicals concentrations, temperature and reaction speed. The underlying chemical reactions are complex and not always understood in depth, since their kinetics is impossible to study by conventional means.

3.3.1 Nanospheres

Spherical gold nanoparticles were prepared by standard citrate reduction as introduced by Turkevich and later refined by Frens [47]. This protocol involves the reduction of a gold salt (tetrachloroauric acid, $HAuCl_4$) by sodium citrate at $100°C$ in water. The final result is a monodisperse colloid in which gold nanoparticles have a tunable range of sizes, approximately from $10nm$ to more than $100nm$ in diameter, depending on various parameters.

The reaction kinetics behind this process is schematized in Figure 3.8 and can be explained with the *self-assembly theory* [48]. When dissolved in water, the hydrophilic tetrachloroauric salt dissociates into a proton and an anion, making the solution slightly acid. The aqueous solution is boiled and vigorously stirred before the addition of a reducing agent, in this case sodium citrate. The reducing agent gives three electrons to the cation Au^{3+}, stabilizing it into a zerovalent monomer Au^0 (metallic gold atom). At first the monomer concentration rapidly grows so as to induce the nucleation of polydisperse primary nanoparticles, followed by their aggregation and coalescence into bigger particles. The final growth into monodisperse nanoparticles is characterized by the consumption of the remaining Au^{3+} through autocatalytic surface reduction.

The direct proof of nanoparticles' formation is the visible change in solution colour from pale

yellow to ruby red (refer to Section 2.3.3 for the theoretical explanation of this phenomenon). Since the so made nanospheres are capped by citrate molecules via Van der Waals interactions and hydrogen bonding, the final colloid is stable over time.
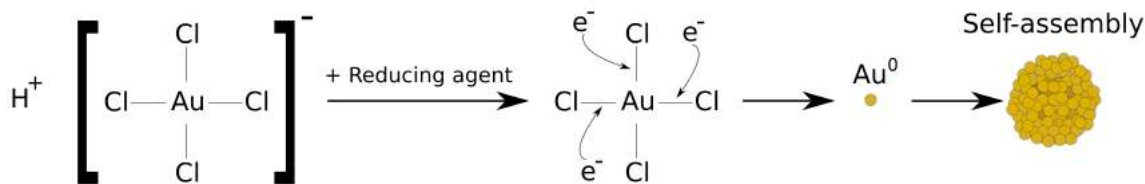

Figure 3.8: Chemical reactions during colloidal synthesys of gold nanoparticles

The exact procedure for making monodisperse gold nanospheres having a mean diameter of $15nm$ is based on Barbosa's protocol [49] and has been carried out as follows:

1. Cover a $250ml$ round-bottom flask with an electric heating mantle and mount it on a magnetic stirrer. The mantle guarantees a homogeneous temperature within the synthesis, while the solution is stirred by a teflon-coated magnetic bar;

2. Mount a condenser to the top neck of the flask and connect it to the cooling system, so that water flows from bottom to top. Fix it with an extension clamp to keep the whole system stable throughout the experiment. The condenser lets the vapor form drops that will go back into the flask so as not to change the solution's original dilution;

3. Block the second lateral neck of the flask with a rubber septum;

4. Inside the flask dissolve $17.1mg$ of $HAuCl_4$ in $100ml$ of MilliQ water so as to obtain a $0.5mM$ concentration of gold salt. Turn on the magnetic stirrer and heat the aqueous solution until vigorously boiling;

5. Inside a beaker dissolve $50.4mg$ of trisodium citrate dihydrate in $5ml$ of MilliQ water to obtain 1 wt% aqueous solution;

6. Use a glass pipette to quickly transfer the citrate solution into the flask through the second neck before immediately close it again with rubber septum;

7. Let react for 15 minutes, then turn off heating but keep on stirring for 5 more minutes;

8. Store the colloid in an opaque container at room temperature, covered in aluminum foil to prevent it from interacting with light.
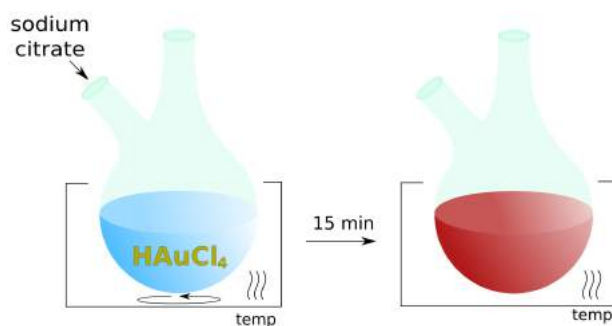

Figure 3.9: Step-by-step synthesis of citrate-capped gold nanoparticles

Assuming that all anions have been reduced into gold atoms which formed spherical nanoparticles of $15nm$ diameter (without leaving residual monomer) and assuming gold's atomic radius of $0.166nm$, the estimated nanoparticle concentration results $\approx 2.3 \cdot 10^{12} NPs/ml$.

3.3.2 Nanostars

The easiest way to produce gold nanostars is to use pre-synthesized spherical seeds of a certain size (in our case, $15nm$ of diameter) as nucleation points for the formation of tips [46]. Such spikes grow along preferential crystallographic directions of the metallic core thanks to the presence of capping agents (such as surfactants or polymers). Indeed, the anisotropic growth of tips has been claimed to be dependent on the preferential adsorption of capping molecules to certain seed's crystalline facets [50].

The seeded-growth of gold nanostars generally requires a metallic precursor ($HAuCl_4$), a mild reducing agent (dimethylformamide [DMF] or ascorbic acid) and some capping molecule (polyvinylpyrrolidone [PVP] or sodium citrate). In certain cases extra additives may become necessary, for example silver nitrate ($AgNO_3$) plays a role in the catalysis of the seeds' defects from which the tips can grow. Recent optimized protocols guarantee a good monodispersity of the tip-to-tip length.

The direct proof of nanostars' formation is the colour change of the solution to blue/dark blue. Indeed, such colour indicates that the extinction cross section peak is in the red part of the visible spectrum ($625nm - 740nm$).

The two different protocols tried are hereby covered: the former is highly reproducible and tunable but makes use of the cytotoxic dimethylformamide (DMF) and so requires a multi-step purification; the latter is instead a biocompatible method that involves ascorbic acid (vitamin C) as reducing agent to produce bare nanostars. While the second method might appear as the ideal one, the lack of a capping polymeric coating makes the nanoparticles highly unstable and prone to undesired aggregation. Moreover, if the nanoparticle is too close to the fluorophore ($< 5nm$) quenching can easily occur. Further functionalization with specific molecules bound to gold via thiols is possible and will represent a future step in this project.

DMF-based synthesis

It has been reported that, in presence of high concentration of PVP in DMF, highly branched nanostars can be obtained at room temperature and very efficiently [46]. Briefly, gold tips can grow on pre-formed gold seeds thanks to the reducing power of dimethylformamide (DMF) and the excess of polyvinylpyrrolidone (PVP).
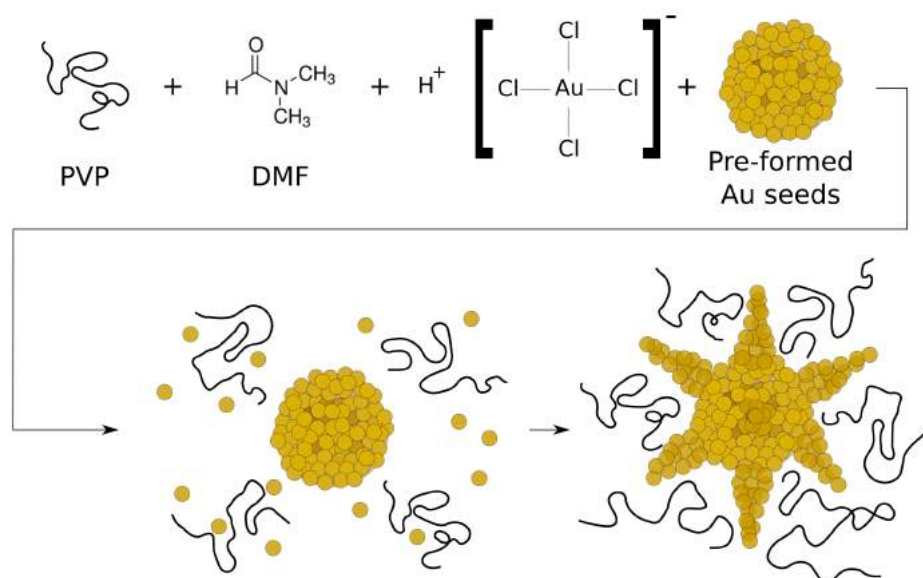

Figure 3.10: Chemical reactions during colloidal synthesys of gold nanostars in DMF

Five tests have been tried with different concentration of seeds. The exact protocol for making PVP-coated gold nanostars having tip-to-tip distance in the range of $40nm$ to $100nm$ is based on Barbosa's synthesis [49] and has been carried out as follows:

1. Prepare the stock solutions:

    - Dissolve $12.2mg$ of $HAuCl_4$ in $0.72ml$ of MilliQ water, to obtain a $50mM$ solution;

    - Dissolve $8.00g$ of PVP (MW 10000) in $80ml$ of DMF and mix vigorously until complete solubilization occurs, to obtain a $10mM$ solution;

2. Put a $25ml$ Erlenmeyer (conical) flask on the magnetic stirrer with a magnetic bar of the appropriate size inside it;

3. Transfer $15ml$ of $10mM$ PVP in DMF solution inside the flask and start stirring;

4. Add $82\mu l$ of $50mM$ $HAuCl_4$ aqueous solution inside the flask and wait 10 minutes while continuously stirring;

5. Add $0.5ml$ of preformed gold seeds ($15nm$ of average diameter) having a concentration from (a) to (e), each half of the previous:

    (a) $2.3 \cdot 10^{12} NPs/ml$

    (b) $1.15 \cdot 10^{12} NPs/ml$

    (c) $5.75 \cdot 10^{11} NPs/ml$

    (d) $2.88 \cdot 10^{11} NPs/ml$

    (e) $1.44 \cdot 10^{11} NPs/ml$

6. Wait 15 minutes for completion of the reaction, then spin at $4000rpm$ for 90 minutes;

7. Purify the solution by taking away the supernatant and re-disperse the pellet in $35ml$ of MilliQ water;

8. Repeat from step 2 for all different seeds' concentration;

9. Repeat the purification step, spinning at $4000rpm$ for 90 minutes and re-dispersing the pellet in $16ml$ of MilliQ water. Store at room temperature in an opaque container.

Following this protocol, five different colloids of approximately $20ml$ have been successfully synthesized. It is important to note that the purification has been carried out twice to ensure the lowest concentration of DMF possible. In fact, DMF is cytotoxic and can be used in cell cultures only in very limited quantities.
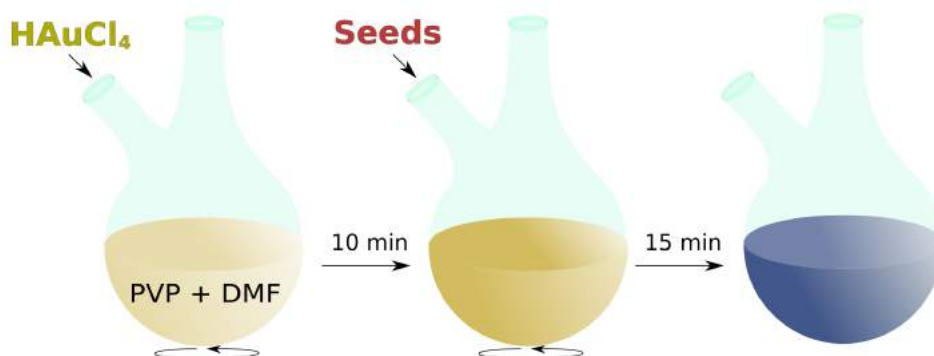

Figure 3.11: Step-by-step synthesis of PVP-capped gold nanostars

Biocompatible synthesis

The need of a biocompatible colloidal synthesis emerges from the well-studied cytotoxic effects of DMF in concentrations higher than 0.1% in the final medium [51]. Indeed, in order to use the nanostars described in the previous section several purification steps are required. Furthermore, the PVP coating might have a thickness such that the distance from the fluorophore is not optimal for fluorescence enhancement.

An alternative approach is then based on the use of ascorbic acid (vitamin C) instead of DMF to reduce the gold salt and silver ions instead of PVP to catalyze the spikes' growth [36]. Briefly, hydrochloric acid HCl activates the reducing power of ascorbic acid, which transforms the anion $AuCl_4^-$ into atomic gold Au^0. This monomer will then grow on the catalyzed sites in which silver atoms, coming from silver nitrate $AgNO_3$, have positioned. This polymer-free synthesis produces bare nanostars, lacking an external capping layer.
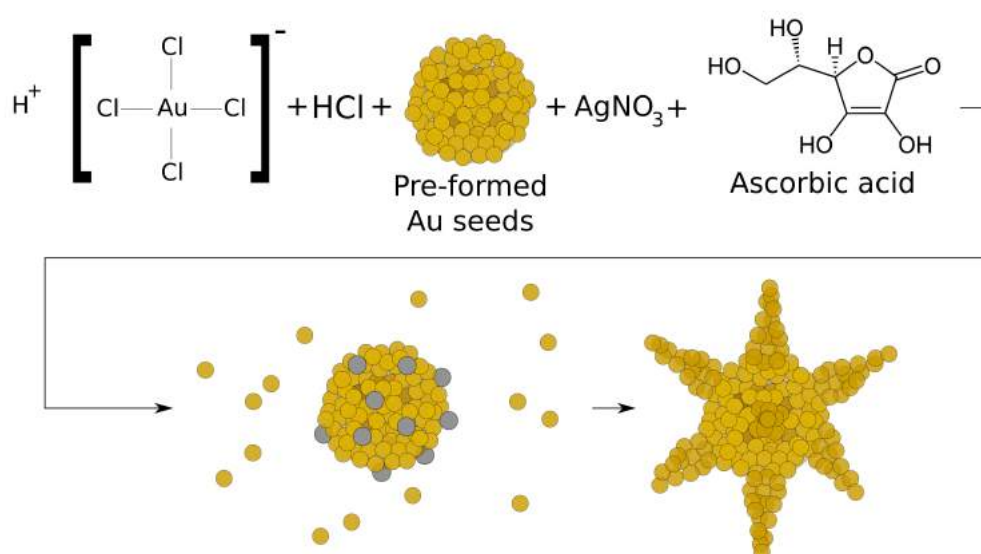

Figure 3.12: Chemical reactions during colloidal synthesis of gold nanostars in ascorbic acid

One downside of this method is that the bare nanostars are way less stable than the coated ones and therefore require to be kept at $4°C$ to slow down the reaction kinetics.

As showed in the original paper [36], the so produced gold nanostars should be highly tunable by varying the initial concentration of seeds. It has to be noted that the concentration of seeds used has been estimated and never measured, but several trials have been carried out to look for a range of different results by diluting the starting colloid.

Hereafter the actual step-by-step procedure followed is explained in detail:

1. Prepare the stock solutions:

    - Dilute $210\mu l$ of $HAuCl_4$ watery solution ($50mM$) in $1.890ml$ of MilliQ water to obtain a $5mM$ solution;

    - Dilute $60\mu l$ of $AgNO_3$ ($50mM$) in $940\mu l$ of MilliQ water to obtain a $3mM$ solution;

    - Dissolve $100mg$ of ascorbic acid powder ($MW = 176.12g/mol$) in $5.7ml$ of MilliQ water to obtain a $100mM$ solution;

2. Put $10ml$ of MilliQ water in an Erlenmeyer (conical) flask on the magnetic stirrer with a magnetic bar of the appropriate size inside it;

3. Fill in advance five micropipettes with the following volumes:

    (a) $500\mu l$ of $HAuCl_4$ solution $(5mM)$;

    (b) $20\mu l$ of HCl (3.7%);

    (c) $5\mu l$ of seeds in a certain concentration;

    (d) $34\mu l$ of $AgNO_3$ $(3mM)$;

    (e) $100\mu l$ of ascorbic acid solution $(100mM)$;

4. Start stirring vigorously, add the solution (a) to the flask and wait $1min$;

5. Add the solution (b) to the flask and wait $30s$;

6. Add the solution (c) to the flask and wait $5s$;

7. Add the solution (d) to the flask and wait $5s$ (nanostars will start to form, changing the overall colour to dark blue);

8. Add the solution (e) to the flask and wait $30s$;

9. Immediately purify the solution by centrifugation at $3000g$ for $10min$, then take the supernatant;

10. Store the final colloid at $4°C$ away from light sources.

The recipe still requires few adjustments since it appears to be extremely sensitive to the timing of each step. In fact it worked only with a concentration of seeds of $2.3 \cdot 10^{12} NPs/ml$ and this result was hard to reproduce in later experiments. Nevertheless, the need of a biocompatible synthesis motivates future investigations on this protocol.

3.4 SEM analysis

The human eye is intrinsically limited in resolution, so we cannot afford to see atomically small details. When aided by light microscopes, the highest achievable resolution is still dictated by the diffraction limit, given enough contrast (for example using fluorescent markers). In order to precisely characterize the produced gold nanoparticles (smaller than $150nm$) an electron microscope is therefore required. Even though a *Transmission Electron Microscope* (TEM) can get close to an atomic resolution, a *Scanning Electron Microscope* (SEM) best unravels surface details such as nanostars' spikes and nanorods' edges and for this reason it has been used to determine the morphology of the previously produced nanoantennas. All the information and the figures in this section are based, adapted and modified from MyScope's website under the Creative Commons license [52].

A Scanning Electron Microscope (SEM), as the name suggests, uses a focused beam of electrons to scan the surface of a sample so as to make a magnified image of it. Typical resolution is lower than $10nm$, depending on the sample.

The interaction between the electron beam and the sample's atoms can have different outcomes: some high energy electrons elastically bounce back (*backscattered electrons*, BSE), some others displace surface electrons that go outside the sample (*secondary electrons*, SE), but they can also lose energy in form of X-rays, light or heat. Traditional *micrographs* (SEM images) are produced by detecting secondary electrons coming out from each scanned spot. In general, SEs are generated from approximately the top $15nm$ of the surface; BSEs, on the other hand, penetrate deeper as the accelerating voltage increases and give information on underlying structures. To image thin samples is then best to avoid the generation of BSEs by keeping the energy of the beam limited (under $2kV$). SEs provide good topographic details, knowing that edges and sharp tips will look brighter since they produce more electrons.

The basic design of an SEM involves four essential parts in order to properly work:

- **Pumps**: a high vacuum minimizes the attenuation and in particular the scattering of the electron beam, making it possible to achieve the smallest probe size and consequently the highest resolution possible. Very often two kinds of vacuum pumps are used, one for rough evacuation and the other for reaching the higher vacuum;

- **Electron gun**: the source of electrons is typically an electrical filament from which electrons are extracted, either by heating (like in a *thermionic electron gun*) or by pulling using a high electrical potential (like in a *field emission gun*). A fraction of the accelerated electrons continue through the column producing a cohesive beam, while the others are returned to the power supply via ground connection;

- **Electromagnetic lenses**: after leaving the source, the diameter of the electron beam is reduced and focused using a system of electromagnetic lenses, copper coils wrapped up around a ferromagnetic material in which current flows. Depending on their function, *condenser lenses*, *objective lenses* and *scanning coils* exist. The scanning of the beam in the X and Y directions is carried out in a process called *rastering*. The so focused beam interacts with the sample, which will mainly produce BSEs and SEs;

- **Detectors**: signals generated from the sample are collected by a detector, converted to photons via a scintillator, amplified using a photomultiplier and converted back to electrical signals. These will be converted from analog to digital and finally sent to a computer. To record topographical information, SEs are attracted towards the detector by applying a small voltage bias (hundreds of volts).

Other devices can be involved, ranging from a water chilling system for avoiding overheating, to a rotating and tilting stage for better imaging of the specimens.
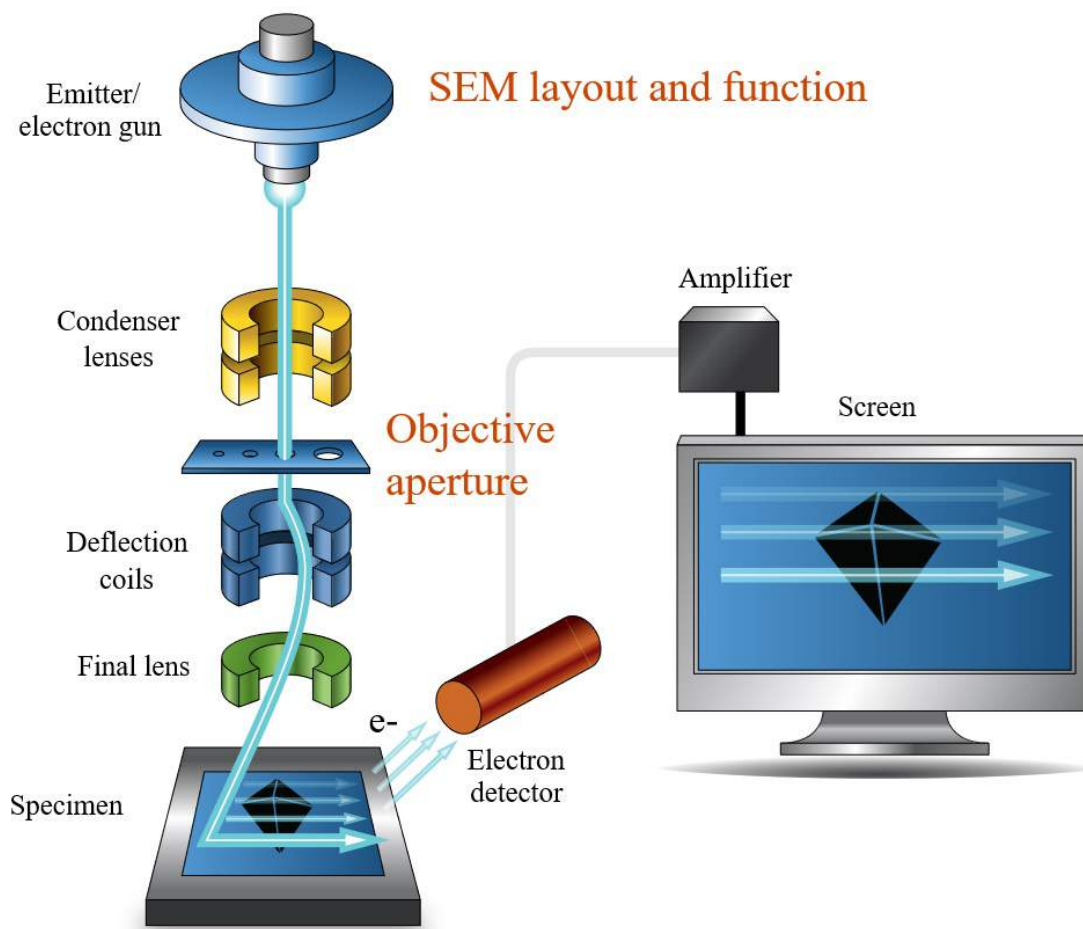

Figure 3.13: Schematic layout of a Scanning Electron Microscope (SEM)

Despite their great performance in optimal conditions, SEMs have several limitations: by working in vacuum, wet samples cannot be imaged; only electrically conductive samples will allow the formation of an image on the detector, while the non-conductive samples will be charged; measurements involving heights will not be accurate; thick samples have to be sliced due to the low penetration of the beam. Either produced by EBL or by colloidal synthesis, the previously made gold nanoparticles overcome all these constraints. In fact, they are intrinsically dry or can be dried easily, gold is conductive, sharp details enhance the contrast and ultimately the interest is focused on the surface's morphology, not on sub-surface structures.

All the specimens put in the SEM have been deposited either by lithography or drop casting of a colloid on indium tin oxide (ITO) coated glass, which is electrically conductive. All the imaged gold nanostructures ranged from $10nm$ to $150nm$.

The instrument employed for the purpose is Thermo Fisher Scientific's *FEI Verios 460*. The emitter is a Schottky Field Electron Gun (SFEG) and can produce an electron current between $1pA$ and $22nA$. The sample landing energy range is between $50V$ and $30kV$. SEs are collected by a Through the Lens Detector (TLD) while in immersion mode (high resolution mode). Pressure inside the chamber is stable under $10^{-5}mbar$. The working distance was recorded to be $5.3mm$ and it's the same for all the images.
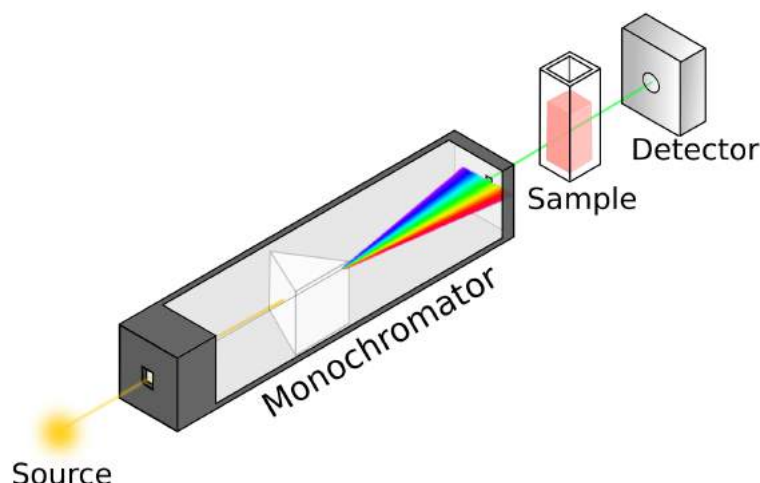
3.5 UV-Vis spectroscopy

Figure 3.14: Simplified schematics of a UV-Vis spectrophotometer

Most compounds undergo electronic transitions between the near-UV and the near-IR regions of the electromagnetic spectrum ($180nm - 2500nm$), affecting the final colour of the substance. Complementary to the study of fluorescent emission, absorption by chemicals is then related to molecular structure and can be measured through a *Ultraviolet-Visible spectrophotometer* [53]. UV-Vis spectrophotometry constitutes one of the most common tools to quantitatively study compounds either in solution or, less commonly, in solids, powders and gases.

The simplest setup (Figure 3.14) involves a radiation source, a monochromator to select the desired wavelength, a sample holder and a detector connected to a computer. Visible light is typically generated using a tungsten filament, while near-UV radiation requires a deuterium lamp. The wavelength selection is carried out by a grating monochromator which is able to scan very precisely the range of interest.

The absorption at each wavelength is quantified by comparing the intensity I of the radiation attenuated by the solution to the intensity I_0 of incident radiation. *Transmittance T* is indeed defined as:

$$T = \frac{I}{I_0} \tag{3.1}$$

The adimensional quantity *absorbance A* is defined as:

$$A = \log_{10}\left(\frac{I_0}{I}\right) = -\log_{10}(T) \tag{3.2}$$

For all the experiments regarding colloids' spectra, a Perkin Elmer's *Lambda 900 UV/VIS/NIR spectrophotometer* has been used. It consists in a double-beam, double monochromator ratio recording system with tungsten-halogen and deuterium lamps as sources. PMT and PbS detectors are used to cover the range $200nm - 2500nm$. In the UV-Vis range the guaranteed accuracy is $0.08nm$ and $0.3nm$ in the NIR. An integrating sphere is included in order to measure samples of high optical density. All samples were contained in a quartz cell and compared to a blank sample previously measured, specifically MilliQ water.

Since absorbance is strongly dependent on concentration of the attenuating species (as stated in the *Beer-Lambert law*), the measured spectra were normalized to unity so as to compare only the absorption peak and not its intensity.

3.6 Multimodal optical microscopy

Since the beginning of the project, the final goal has been the application of the produced nanoparticles to living cells and animals expressing one of the fluorescent Genetically Encoded Voltage Indicators (GEVIs). The physiology of such complex biological systems can only be approached non-invasively by using light microscopy. The multimodal optical setup used was built and optimized by Xin Meng, Gréta Szabó and Teun Huijben.

The optical table involves a *widefield microscope* and a *galvanometric scanning two-photon microscope*, so as to excite and measure the fluorescence of the expressed GEVIs.
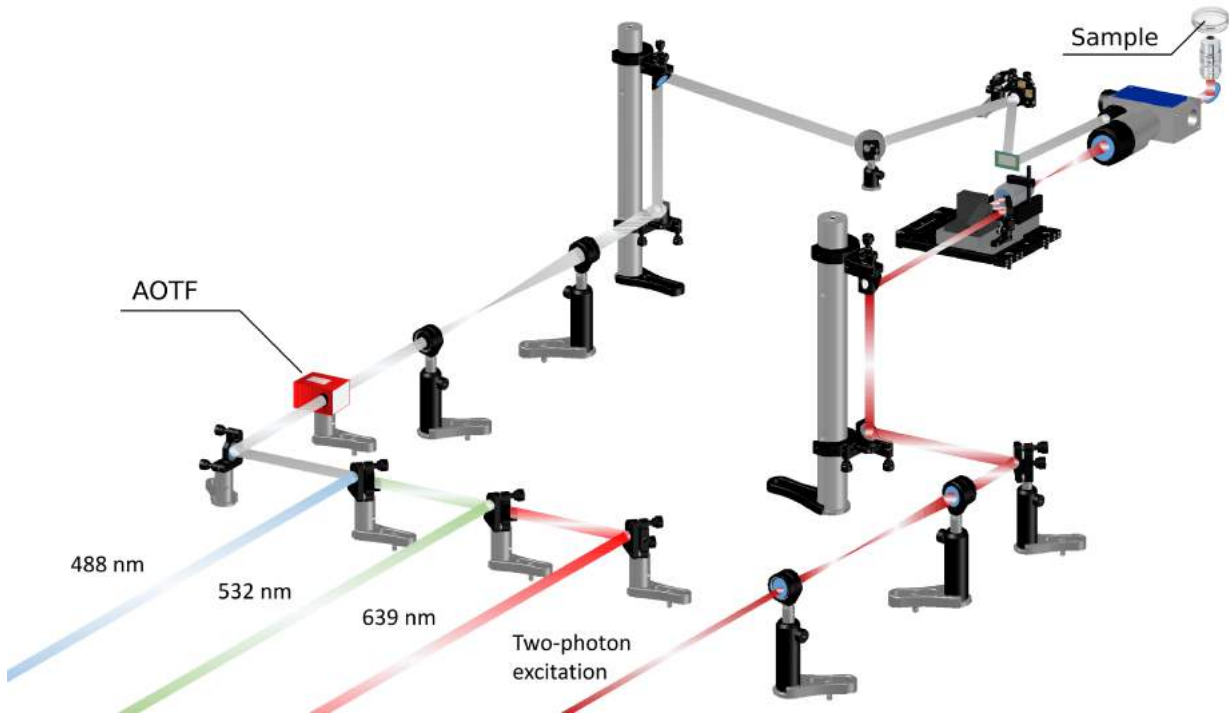

Figure 3.15: Excitation pathway of the imaging setup (courtesy of Xin Meng)

As far as the widefield pathway is concerned, three continuous wave laser sources of different wavelengths ($488nm$, $532nm$ and $639nm$) are combined using dichroic mirrors. Then, the beam is patterned temporally by passing through an *Acousto-Optic Tunable Filter* (AOTFnC-VIS from AA Optoelectronics) having a $22kHz$ switch rate. The intensity modulation is achieved via a *Digital Micromirror Device* (DMD, Vialux V7001 from Texas Instruments). As this DMD reflects the beam, light enters a *tube lens* (TTL200 from Thorlabs) and the pattern is projected by the objective. Finally, a digital camera (ORCA-Flash4.0 V3 from Hamamatsu, not depicted in Figure 3.15) captures the image in a low-noise configuration.

In parallel, two-photon (2P) microscopy is a form of nonlinear microscopy that can be achieved by employing a near-infrared pulsed laser and a galvanometric scanner. In our case, the laser source is an *ultrafast laser system* (Spectra-Physics InSight X3) tunable in the $680nm-1300nm$ range, having $120fs$ pulse width. The 2P beam is moved in the XY-plane by the fastest *galvanometric scanner* on the market (6215HR by Cambridge Technology). Along the pathway, a *long-pass dichroic mirror* (Di03-R785-t3-32x44 by Semrock) separates the excitation from the emission. Given that all the emission is expected to come only from the illuminated spot, to maximize the sensitivity a *photomultiplier tube* (PMT) has been employed (H10721-01 or

H10721-20 by Hamamatsu, depending on the fluorescence's wavelength). The PMT's output current has to be amplified by an external amplifier prior the sampling with a *National Instruments Data Acquisition Device* (NI DAQ).

A *beam-turning cube* was implemented in order to easily switch the emission's destination between the PMT and the camera. The acquired images or videos can be analyzed and processed later on using the free software ImageJ, working on any kind of modern computer. Measured signal can be either coming from gold nanoparticles themselves (photoluminescence) or from fluorophores (fluorescence).

3.6.1 Photoluminescence

When used in this thesis, the term *photoluminescence* will only refer to the laser-stimulated light emission by gold nanoparticles, to distinguish it from proteins' fluorescent emission. The first observation of bulk gold's photoluminescence was in 1969 by Mooradian [54], motivating later studies more specific on gold nanostructures. The process is object of research since the lack of a specific energy band gap between the valence and the conduction bands makes the luminescence a rare event.

The photoluminescence mechanism of gold involves the absorption of a photon, which will excite an electron from the d band to the $s - p$ band, and the consequent radiative recombination from the $s - p$ to the d band [55]. Non-radiative processes are also possible and influence the final energy of the emitted photon.

Green absorption is way more efficient than red absorption [56], so in our experiments the green laser ($532nm$) has been used. By filtering the incoming light, photoluminescence was easily measurable. Particular care has to be taken when imaging proteins that are linked to fluorophores excitable by green light. Given the low efficiency of the process and the size of the nanoparticles, the emission will appear as a dim diffraction-limited spot.

3.6.2 Fluorescence

Imaging of biological samples has been carried out by using a combination of a laser source (either 1P or 2P) and a filter, depending on the Genetically Encoded Voltage Indicator (GEVI) expressed in the cells. For all experiments, HEK cells (*Human Embryonic Kidney* cells) expressing the GEVI were plated on fibronectin-coated glass dishes.

All the proteins studied are variants of Arch (QuasAr2, QuasAr3, NovArch, Archon), so their fluorescence was excited with the red laser ($639nm$) and the filter had $660nm - 800nm$ range. In the case of 2P microscopy, the excitation wavelength has to be considered as doubled. Some proteins have a linked fluorescent marker (Citrine, mOrgange, GFP) to make it easier to find the most relevant transfected cells.

3.7 Patch clamp

Electrical signals naturally occurring in cells emerge when ions flow through the membrane in a dynamic and highly regulated cycle. In order to control or measure such signals a space-effective, sensitive, non-destructive and reliable tool has to be used. The electrophysiological technique of *patch clamp* has been developed in the late 1970s by Erwin Neher and Bert Sakmann to accomplish these specific tasks [57][2].

The idea behind patch clamp is rather simple but it requires an advanced technology to function properly: by accessing the cytoplasm through a small aperture, the electric potential can be measured via an electrode connected to an external negative-feedback amplifier. Thanks to the feedback system a single electrode is sufficient to both measure and control at the same time voltage and current. The reference electrode is put in the extracellular medium.

The glass pipette containing the $Ag/AgCl$ filament and a saline solution presents a very sharp tip with a small aperture of approximately $1\mu m$ in diameter (or less). The perfect adhesion of the membrane to the glass aperture (typically referred to as the *seal*) is necessary to perform a whole-cell experiment; this indeed ensures that there is no leakage current and that the concentration of ions inside the pipette is the same of the cytoplasmic one. The seal, corresponding to several gigaohms $(G\Omega)$ of resistance, can be obtained by applying a suction when nearby the cell followed by a zap suction to break just a patch of membrane.
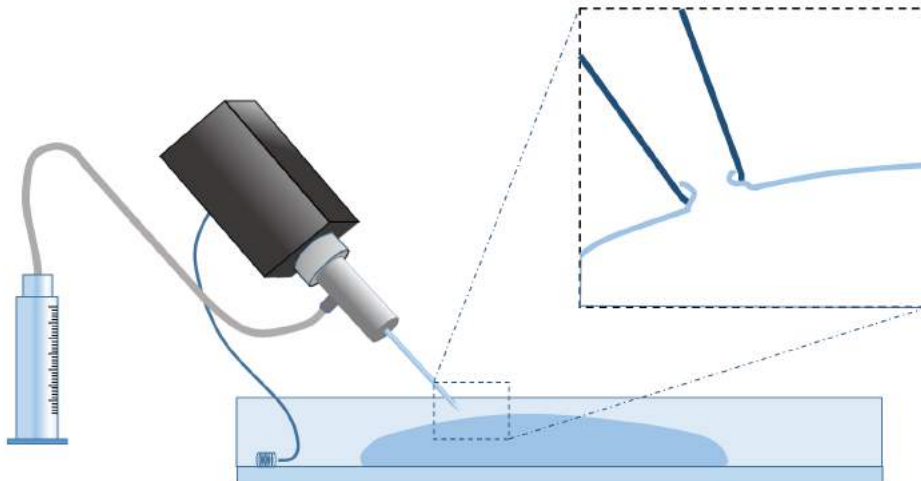

Figure 3.16: Whole-cell patch clamp (courtesy of Xin Meng)

The ionic concentration is converted to an amplifiable electrical signal following the reaction of the $Ag/AgCl$ electrode:

$$Cl^- + Ag \rightleftharpoons AgCl + e^- \tag{3.3}$$

With the patch clamp technique it is possible to either:

- Control the membrane potential and measure the current (*voltage clamp* configuration);

- Control the current and measure the membrane potential (*current clamp* configuration).

In our experiments on HEK cells, patch clamp is essential to precisely set a certain voltage and look at the fluorescent response of the protein of interest. Although other configurations are possible (cell-attached, inside-out, outside-out, perforated patch) only whole-cell setting has been employed. This can in principle allow the study of the voltage-sensitive fluorescence in presence and absence of gold nanoparticles without the use of qualitative external perfusions.

Chapter 4

Results and discussion

In this chapter I will discuss the results of my work, their analysis and their implications. The workflow goes from gold nanoparticles' simulations to production (either with electron beam lithography [EBL] and colloidal synthesis), to their application on HEK cells expressing the Archaerhodopsin-based GEVIs of interest.

Section 1 will show the results obtained with FDTD simulations, highlighting the optimal conditions for tuning the plasmonic resonance to the desired wavelength; assumptions and limitations of the model are also explained.

Section 2 will focus on the production of patterns of nanorods with EBL on ITO coated glass and their SEM characterization.

Section 3 will present the outcomes of the nanoparticles' colloidal synthesis; citrate-capped gold nanospheres, PVP-coated nanostars and biocompatible nanostars have been characterized with the UV-Vis and SEM technologies.

Section 4 will ultimately explain the attempts carried out to measure plasmonically enhanced fluorescence in HEK cells and the challenges encountered.

4.1   Preliminary simulations

After an initial testing phase to learn how to operate *Lumerical's FDTD Solutions* software, three different morphologies have been simulated with a very small mesh size: rods, spheres and stars. For the first case, the results helped in the design of optimal nanorods to produce with EBL; simulations of spheres confirmed the theoretical prediction that the plasmonic resonance can only be sufficiently red-shifted with very large nanoparticles; finally, simulations of nanostars helped explain *a posteriori* the spectra of previously characterized colloids.

4.1.1   Nanorods

Gold nanorods have been simulated using the script written in Appendix B.1 and analyzed with the free software SciDAVis.

In brief, the code varies the three main parameters (namely length l, width w and height H) of the smoothed rod immersed in water and computes the maximum average field enhancement $|E|^2/|E^0|^2$ in a small volume ($\Delta x = w/2, \Delta y = w/2, \Delta z = H$) $4nm$ away from the surface.

Then, the resonance wavelength and the corresponding average field enhancement are saved in a text file. This computational "screening" continues in a defined range by steps of $5nm$:

- $20nm \leq l \leq 100nm$;

- $20nm \leq w \leq 50nm$;

- $20nm \leq H \leq 50nm$;

The script skips tests with higher l if the resonant wavelength is higher than $780nm$ (not in the region of interest) to save computational time.

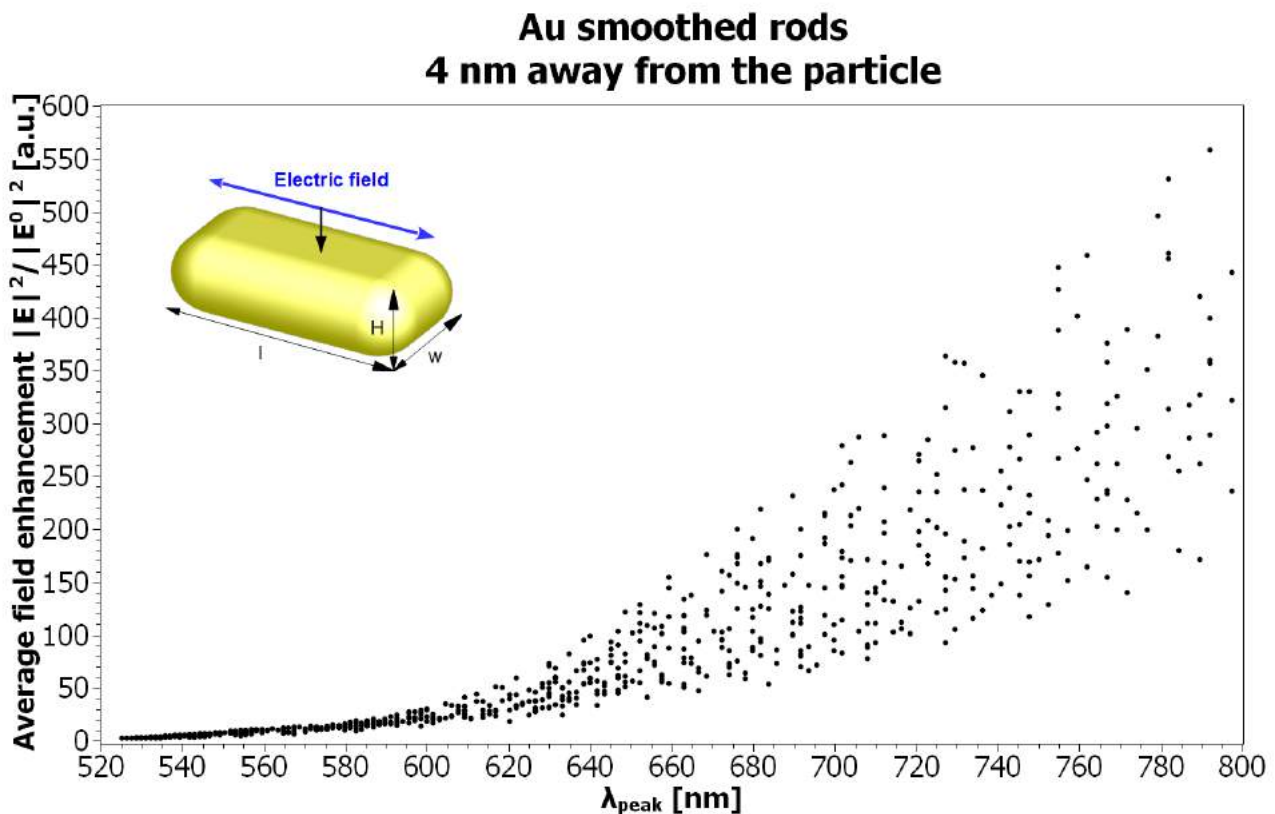Here presented are the results of these simulations:

Figure 4.1: Screening of gold nanorods where each spot corresponds to a set (l,w,H)

In Figure 4.1 each dot corresponds to a set of parameters (l,w,H). Because of the choice of the ranges, only the longitudinal resonance has been tested, so the transverse resonance does not appear in the graph. As expected from the theory of elongated rods and from previous experiments [58], the more the resonance is red shifted the stronger the field enhancement would become. This directly relates to the aspect ratio of the nanoparticle.

Differently from other kind of studies, these simulations took into account also different values for the height H, not treating it as negligible. The height's effect is qualitatively similar to the one appearing when changing the width, explaining why many combinations of parameters give a similar resonance wavelength.

From this graph it is possible to see that a much higher field enhancement can be obtained at higher wavelengths, so in principle one could ask why a weaker resonance around the emission peak of the fluorescent protein was chosen. For the coupling between the fluorophore and the gold nanorod to improve the quantum efficiency, the nanorod needs to be resonant with the

emission spectrum of the fluorophore. The emission of the protein is approximately a gaussian of FWHM $60nm$ centered around $680nm$; the spectrum of the nanorod is typically $40nm$ wide centered around the peak values as indicated in Fig. 4.1. The overlap integral of these two spectra determines the effective enhancement. Moreover, some geometries are unsuitable for EBL, resulting in unstable or impossible to fabricate structures.

A significant example of parameters resulting in a plasmonic resonance around the fluorescent emission peak is hereby reported:

l [nm]	w [nm]	H [nm]	λ_{peak} [nm]	Avg F.E. [a.u.]
75	50	25	676.056	75.4089
75	25	50	676.056	124.423
65	30	25	676.056	148.683
65	25	30	676.056	167.142
55	25	20	676.056	173.081
50	20	20	676.056	175.636
55	20	25	676.056	200.328
95	50	45	677.966	58.5407
95	45	50	677.966	64.0278
70	30	30	677.966	145.507
90	40	45	679.887	84.9346
85	45	35	679.887	88.2678
85	35	45	679.887	103.61
65	40	20	679.887	116.117
80	30	45	679.887	123.998
65	20	40	679.887	190.651
90	45	40	681.818	80.8659
80	45	30	681.818	93.6697
75	45	25	681.818	96.3441
75	35	30	681.818	126.722
75	25	45	681.818	146.198
75	30	35	681.818	150.726
60	30	20	681.818	167.137
60	20	30	681.818	219.02
100	50	50	683.761	53.194
80	35	35	683.761	124.754
70	35	25	683.761	138.211
70	20	50	683.761	170.456
70	25	35	683.761	172.723
95	45	45	685.714	73.282
70	50	20	685.714	86.2296

Figure 4.2: Combinations of parameters that give a peak in field enhancement around $680nm$

In order to choose the best combination of parameters, both the highest field enhancement and the feasibility during EBL production have been considered. For this reason, the *optimal* set of (l,w,H) chosen was $(65nm, 40nm, 20nm)$ as highlighted in Figure 4.2 in light green.

Reported next is also the empirical formula for the wavelength of resonance λ_{peak} obtained from a multi-parameter fit of the data:

$$\text{For } \lambda_{peak} > 540nm, \qquad \lambda_{peak} = \left[432 + 111.4\sqrt{\frac{l^2}{wH}}\right]nm, \qquad \epsilon \lesssim 5\% \qquad (4.1)$$

This fit function has been formulated by taking into account the dependency of plasmonic resonance to the aspect ratios l/w and l/H [59]. Adding these two terms didn't work well, but their product made the data points very close to a square root function. Applying the square root to the product of l/w and l/H the linear dependency was obtained for wavelengths higher than $540nm$, as shown in Figure 4.3.

This fit function should not be considered as explanatory nor descriptive of the system, but only a fast way to calculate approximately where the peak would be given a set of parameters. It only works with smoothed gold nanorods immersed in water.
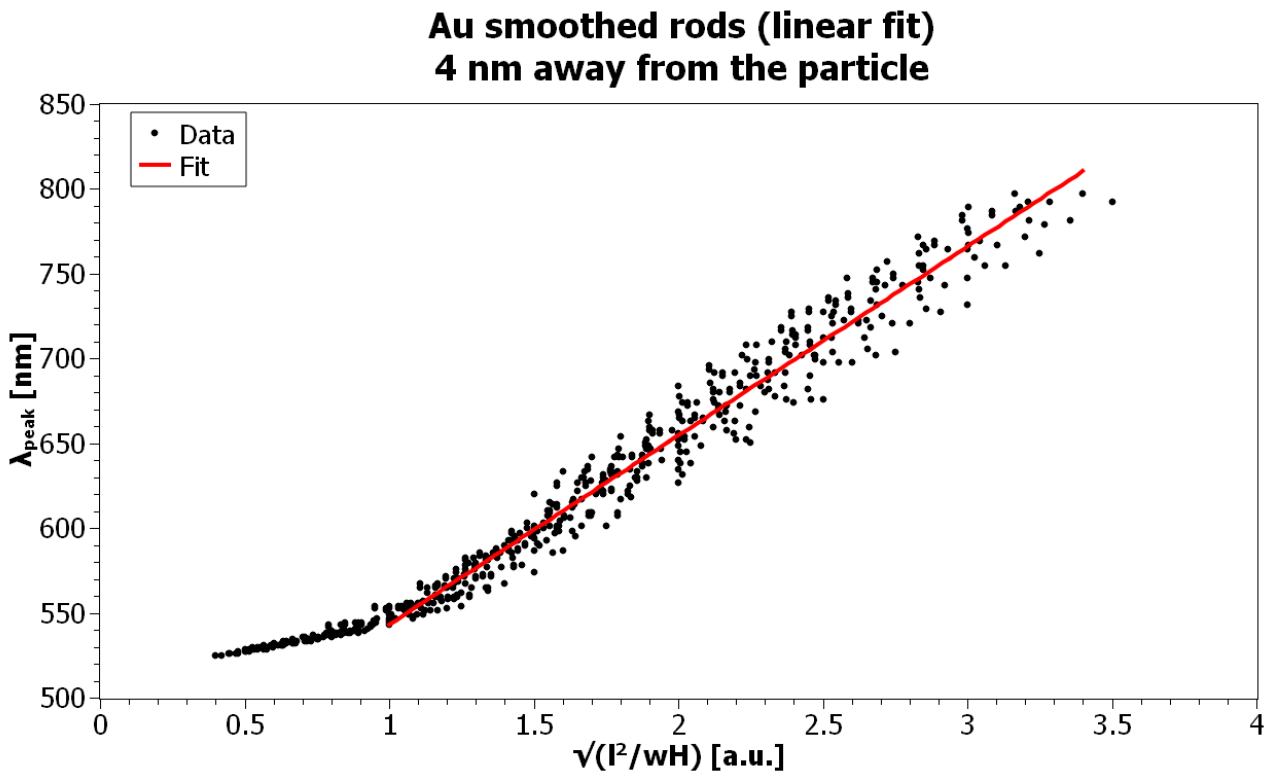

Figure 4.3: Empirical relation between wavelength peak position and aspect ratios

4.1.2 Nanospheres

Gold nanospheres have been simulated using the script written in Appendix B.2 and analyzed with the free software SciDAVis.

The code varies the radius R of the sphere immersed in water and computes the maximum average field enhancement $|E|^2/|E^0|^2$ in a small volume ($\Delta x = R/2, \Delta y = R/2, \Delta z = R/2$) $4nm$ away from the surface. Then, the resonance wavelength and the corresponding average field enhancement are saved in a text file. This computational "screening" continues in a defined range by steps of $2nm$, from $R_{min} = 6nm$ to $R_{max} = 76nm$.

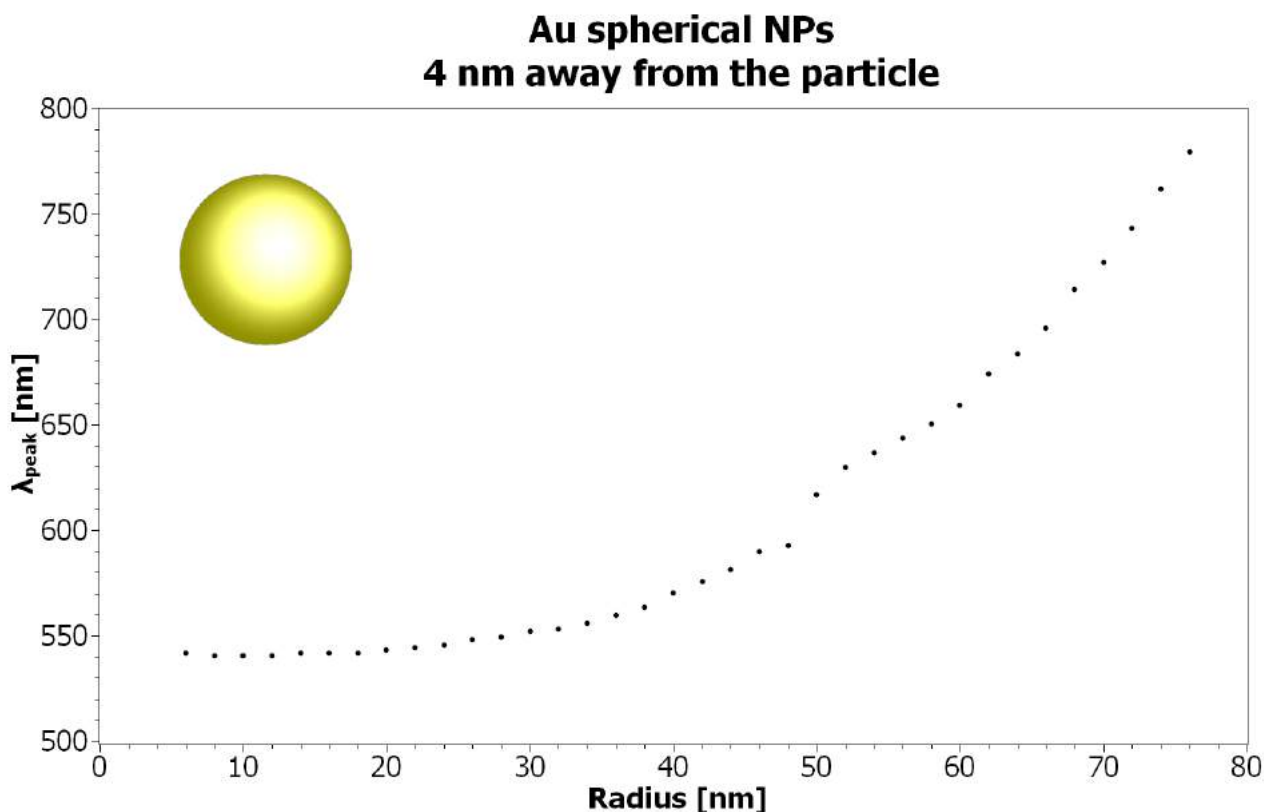Here presented are the results of these simulations:

Figure 4.4: Screening of gold nanospheres; bigger radii correspond to stronger peak's red shift

In Figure 4.4 is depicted the relation between the radius of the sphere and the wavelength peak in the average field enhancement. The simulation results very well agree with what is known from the theory, that is the limited tunability of the plasmonic resonance for such shape. It is important to notice that the wavelength peak is not exactly the same as the one measured in absorption experiments. This might happen because the absorption spectrum takes into account every mode excited in the nanoparticle, including transverse modes, whereas the enhancement as plotted here looks specifically at the field on the short edge of the particle aligned with the polarization of the incoming light, thereby preferentially taking longitudinal modes into account.

From this diagram it can be evinced that, in order to have a resonance with the fluorescent protein, the radius should be between $62nm$ and $64nm$, resulting in a particle of total diameter $\approx 125nm$. Even though feasible to synthesize, a nanoparticle like that would eventually be bigger than the actual cellular substructures we aim to study. Moreover, comparing the average

field enhancements (in Figure 4.5) with the values found for nanorods it becomes clear that spheres are not the ideal shape for our application.
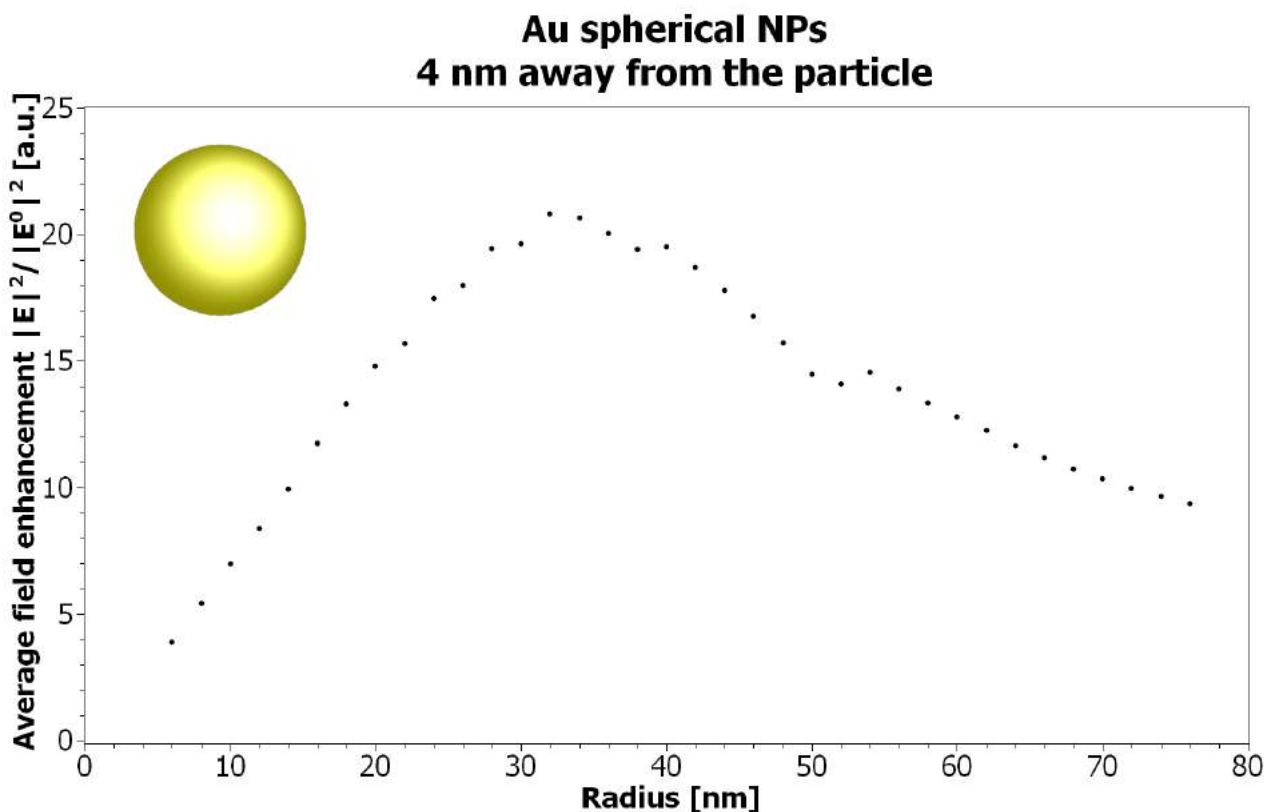

Figure 4.5: Screening of gold nanospheres; bigger radii correspond to lower field enhancement

This detrimental effect can be attributed to the emergence of multipolar contributions, which broaden the peak and break the quasi-static approximation. This kind of simulations was nevertheless useful to check the robustness of the method employed and to directly compute the effective electric field instead of inferring it from indirect measurements.

R [nm]	λ_{peak} [nm]	Avg F.E. [a.u.]	R [nm]	λ_{peak} [nm]	Avg F.E. [a.u.]
6	541.761	3.88371	42	575.54	18.7101
8	540.541	5.40551	44	581.114	17.7731
10	540.541	6.97065	46	589.681	16.7477
12	540.541	8.3692	48	592.593	15.7059
14	541.761	9.93776	50	616.967	14.4857
16	541.761	11.7266	52	629.921	14.0764
18	541.761	13.2852	54	636.605	14.5228
20	542.986	14.7881	56	643.432	13.8845
22	544.218	15.6711	58	650.407	13.3288
24	545.455	17.4572	60	659.341	12.777
26	547.945	17.966	62	674.157	12.2398
28	549.199	19.4495	64	683.761	11.6387
30	551.724	19.6205	66	695.652	11.1524
32	552.995	20.7903	68	714.286	10.7278
34	555.556	20.6314	70	727.273	10.3308
36	559.441	20.0414	72	743.034	9.96901
38	563.38	19.3932	74	761.905	9.62723
40	570.071	19.4858	76	779.221	9.34166

Figure 4.6: Complete results obtained from screening of gold nanospheres

4.1.3 Nanostars

Gold nanostars have been simulated using the script written in Appendix B.3 and analyzed with the free software SciDAVis. The developed model is entirely based on the PVP-coated gold nanostars as synthesized via the procedure described in Section 3.3.2, using the information gathered from their SEM imaging (see Section 4.3.2 for more information).

In brief, the code varies the radius R of the core of the nanostar immersed in water and having a fixed tip length of $10nm$. The script computes the maximum average field enhancement $|E|^2/|E^0|^2$ in a small volume ($\Delta x = R_{core}, \Delta y = R_{core}, \Delta z = R_{core}$) $4nm$ away from the surface. Then, the resonance wavelength and the corresponding average field enhancement are saved in a text file. Absorption and scattering cross sections are also saved separately as functions of the wavelength. This computational "screening" continues in a defined range by steps of $5nm$, from a core radius of $R_{core,min} = 20nm$ to $R_{core,max} = 50nm$.

The goal of these simulations is to explain and describe *a posteriori* the measured spectra of the respective colloids.

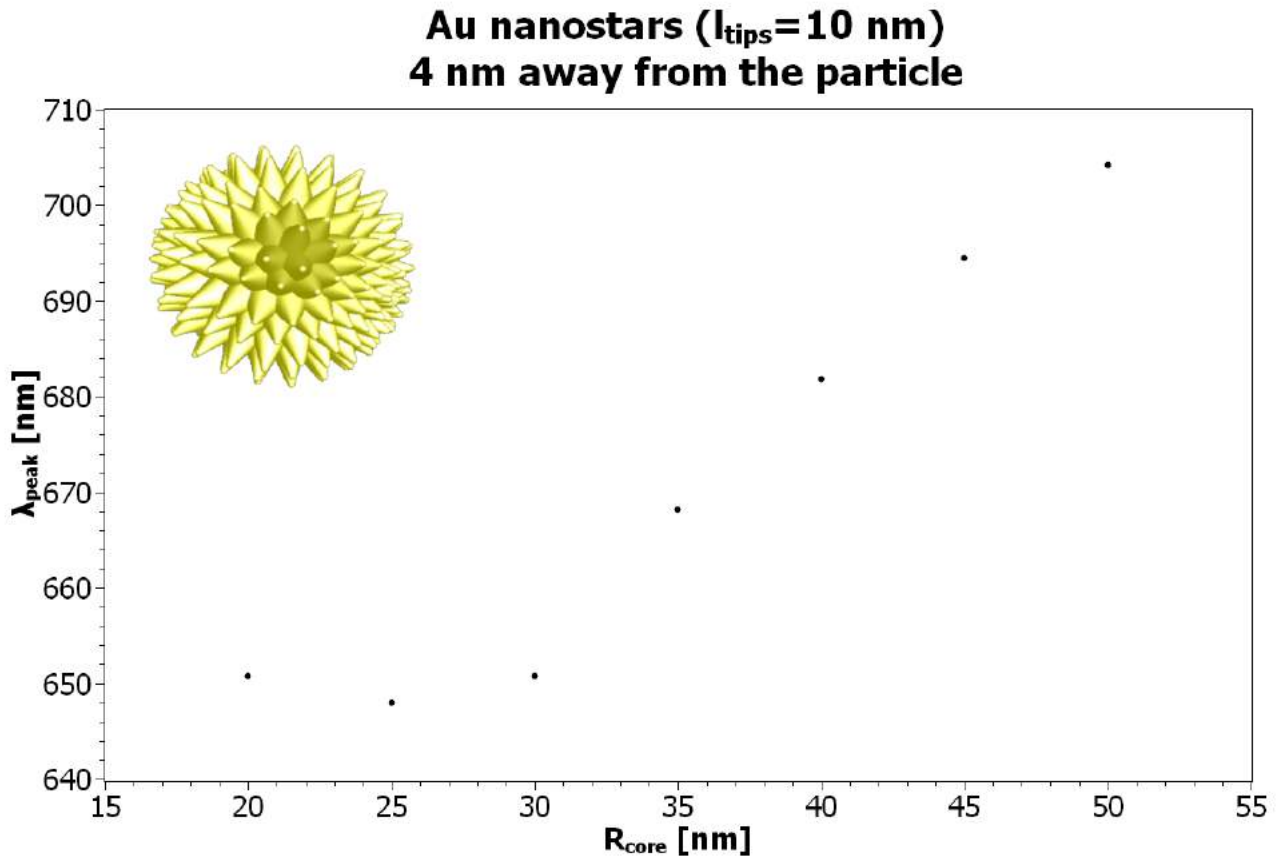The results obtained and their discussion are provided below:

Figure 4.7: Screening of gold nanostars; bigger radii correspond to a tunable peak's red shift

It appears interesting how the presence of the tips, as expected from the theory [38], immediately red shifts about $100nm$ compared to the plasmonic resonance of a gold spherical particle having the same size. Compared to the nanospheres, nanostars present a much more limited shift in resonance wavelength when the core size is changed, allowing a finer tunability of the peak. The initial blue shift is explained by observing the comparison of the cross sections in Figure 4.9 and Figure 4.10, and results from the competing effects of absorption and scattering.

From this simple model we infer that the ideal nanoparticles should have a core radius of $40nm$ and $10nm$-long tips, so as to be resonant with the protein at $680nm$. That is in principle confirmed by the comparison of UV-Vis spectra with the SEM charaterization of the synthesized gold colloids.
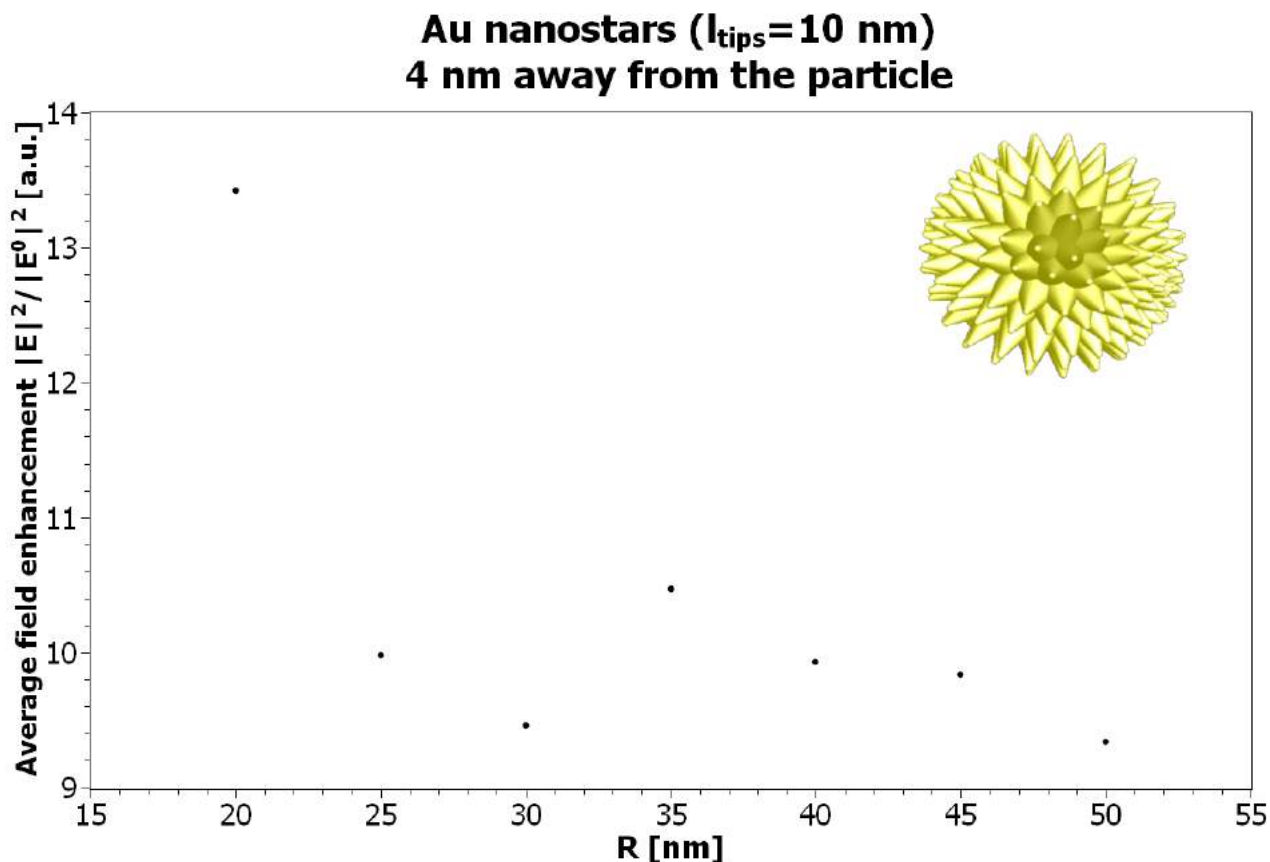

Figure 4.8: Screening of gold nanostars; field enhancement is not so dependent on core size

As far as the average field enhancement is concerned (Figure 4.8), it might seem that the effect is as strong as in the spherical case. However it has to be considered that for the sphere the enhancement is evaluated in a smaller region compared to the one evaluated for stars. Moreover, enhancement was computed 4 nm from this spacer layer, considering the whole system immersed in water. That means that the local field enhancement is expected to be much stronger and more focused at the spikes' tips. In this sense, the not negligible average field enhancement ensures that at least some of the proteins close by will be strongly affected.

From the results obtained we can carefully say that the field enhancement intensity is not particularly dependent on the size of the nanostar, as much as it was with spheres. Extra simulations might be helpful in the clarification of this feature.

Figure 4.9 reports the comparison between absorption and scattering cross sections, altogether with the extinction cross section which simply is the sum of the previous two. It can be clearly seen that small nanostars are dominated by absorption of the radiation, so they are not very efficient for our application. Scattering starts to become comparable and predominant over absorption in nanostars having a core radius of at least $R_{core} = 40nm$. Fortunately, that means that the optimal nanostars we identified before should work as expected, presenting negligible quenching effects and a hopefully higher overall radiative decay rate.
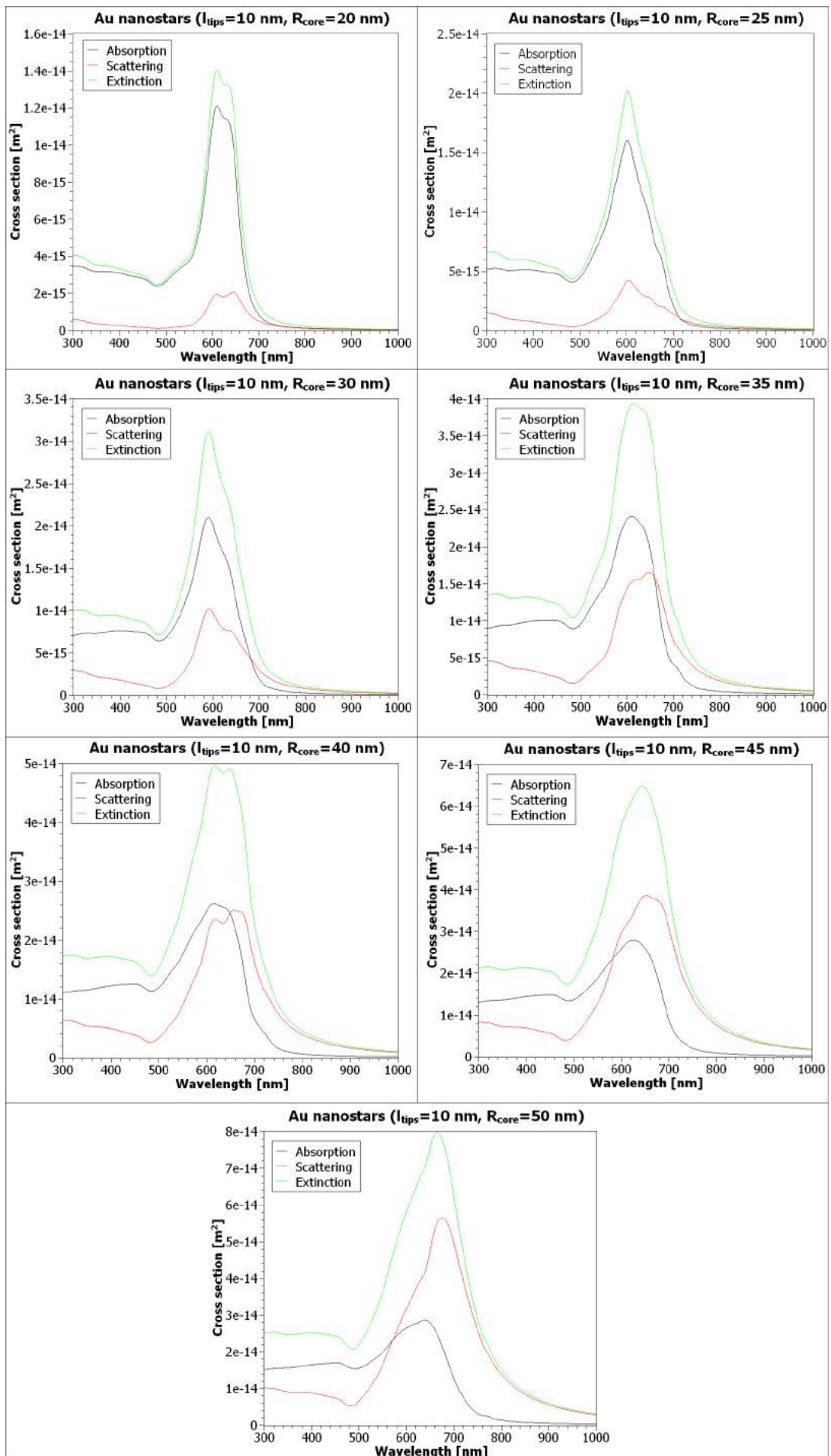
Figure 4.9: Absorption, scattering and extinction cross sections for different core sizes

For some reason related to the presence of the spikes, the absorption peak is always blue shifted respect to the scattering one. This translates in a first general blue shift when growing bigger particles, followed by again a red shift. From this we can infer that the size of the nanoparticles is not easily inferable from the UV-Vis spectra, but requires extra SEM characterization.
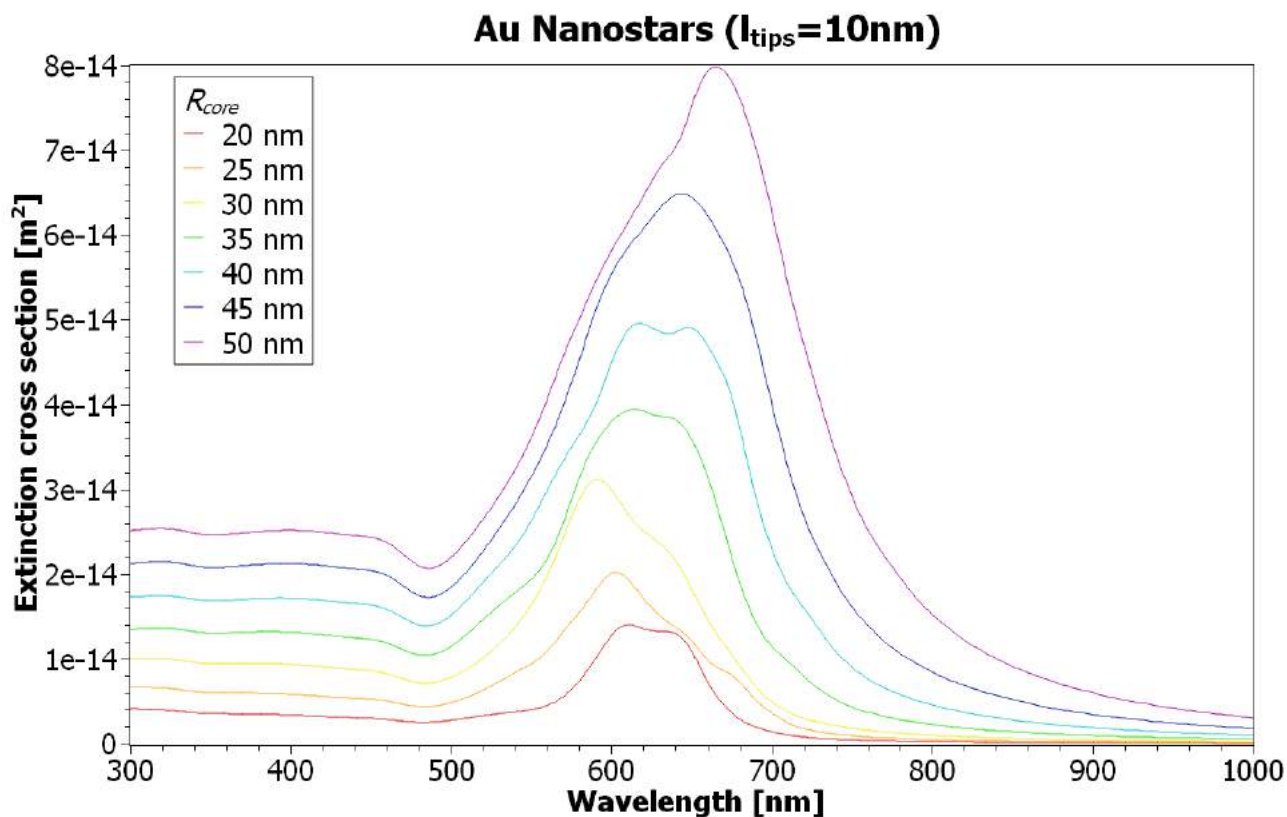

Figure 4.10: Comparison of overall extinction cross sections for different core sizes

The comparison in Figure 4.10 summarizes the main effects happening when growing bigger nanostars. The most notable one is the significant broadening of the peak due to non-dipolar effects, resulting in a less selective plasmonic resonance. It is important to remember that the emission spectra of the proteins are somehow broad as well. While not initially considered, it is possible that such a broad peak could positively affect the absorption as well in the *lightening rod effect* (see Section 2.3.5 for deeper insight).

Measured UV-Vis spectra in Section 4.3.2 can be qualitatively interpreted as a convolution of peaks due to the size distribution of the nanospheres. The characterized colloids show in fact that the tip-to-tip distribution span in ranges of $40nm$ between minimum and maximum sizes. Considering also that each nanostar has its unique features and that the model only considers a single ideal morphology, this explanation must remain qualitative.

4.2 EBL of gold nanorods

The design of the gold nanorods is based on the optimal parameters found from simulations in Section 4.1.1. In order to test their functionality on fluorescent cells, the nanoparticles must be deposited on a transparent substrate, preferably an imaging glass. Given that a conductive substrate is needed in the EBL production, ITO coated glass slides have been employed. The thickness of the slides must be carefully kept as low as possible, since the working distance of the objective is a limiting factor in optical imaging.
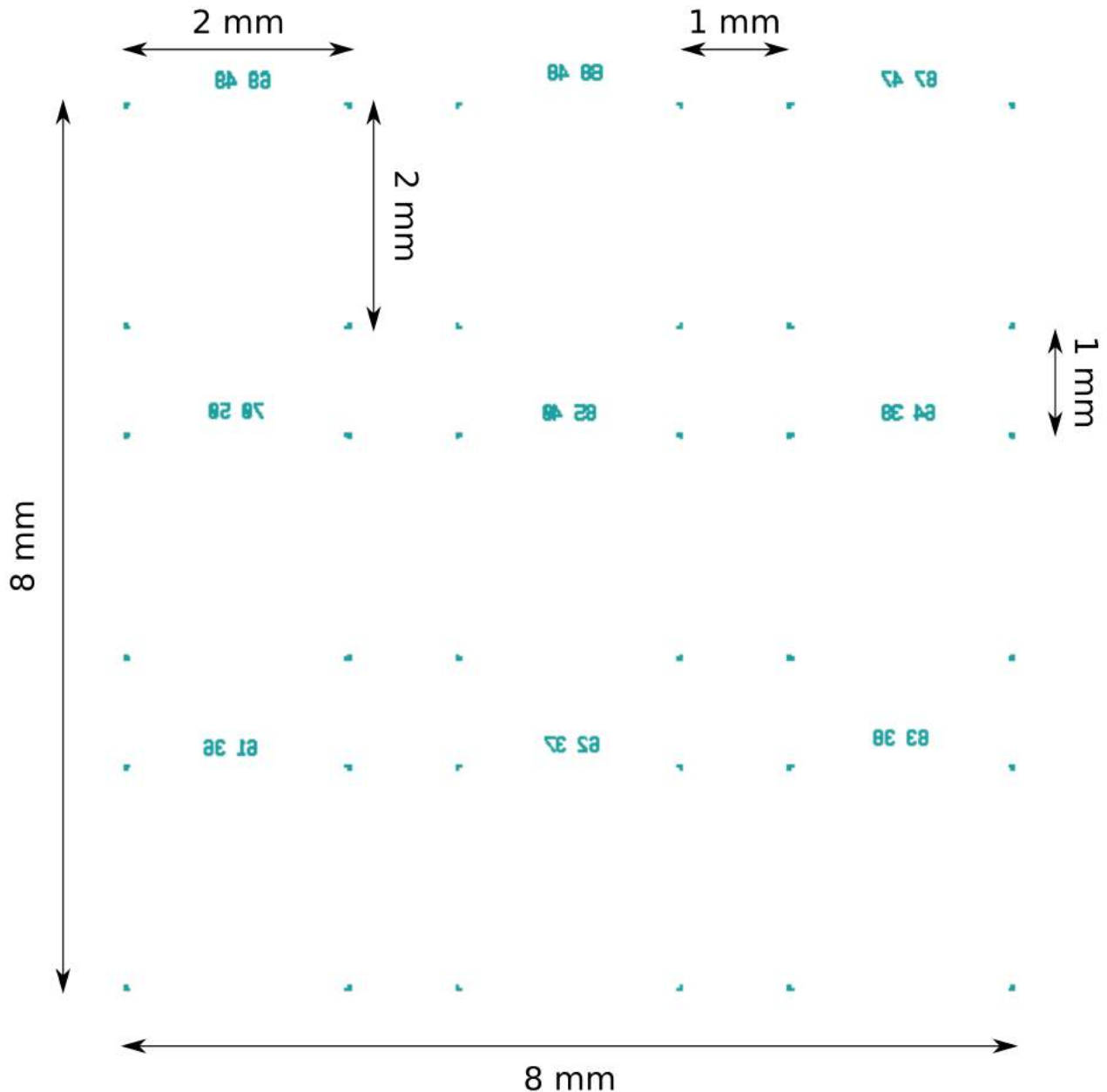
Figure 4.11: Markers' design; the written numbers are mirrored in order to appear correctly in an inverted optical microscope. Nanorods of different sizes (not depicted) are deposited inside each $2mm$ x $2mm$ square

In the spirit of testing small variations from the ideal design, not being sure of the final result of lithography, nine different combinations of length and width have been included on the same substrate. The written pattern also includes several markers visible by naked eye so as to easily find and identify the nanorods.

In Figure 4.11, the marked numbers correspond to the pair length-width of the rods (in this order), while the marked square edges delimit the region where the actual patterns have been deposited. Such markers also represent a fast way to check the successfulness of the whole process: if the markers are not visible in the optical microscope, probably there are no nanorods either. The contrary is however not always true, so extra inspection is needed.

The nanopatterns are designed so as to have a grid spacing of $3\mu m$, as shown in Figure 4.12. This distance is a good trade-off between length of EBL writing and density of particles. We expect on average to find 2 to 4 nanoparticles under each healthy HEK cell knowing that their average diameter is typically between $11\mu m$ and $15\mu m$ [60].
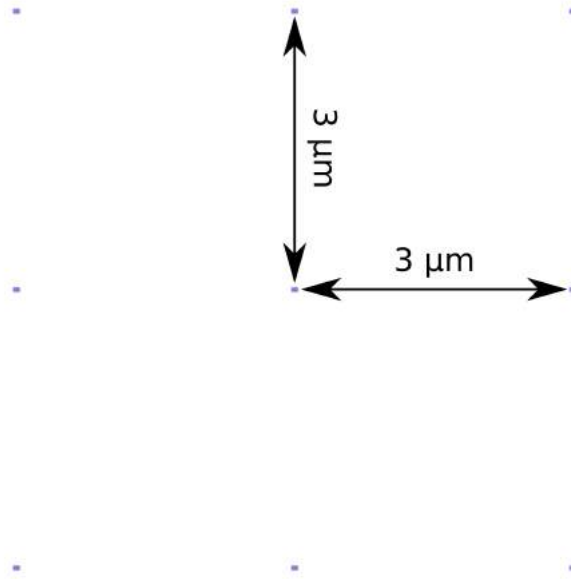

Figure 4.12: Nanorods design in a regular pattern

The whole production process has been more challenging than initially expected, not being successful for most of the time. The encountered issues have been various and time consuming to tackle:

- Originally, the ITO glass slides were too thin ($170\mu m$) so when the sample was clamped in the EBL machine it could easily break or at least bend. This would result in a failure of the height check, stopping the exposure before even starting the beam;

- Being almost completely transparent, the ITO glass surface was incredibly hard to measure, contributing to the difficulty of completing the height check;

- The recipe for the double-layer polymeric resist had to be adjusted several times before finding the optimal combination to achieve the desired resolution.

In order to fix the two first issues we employed thicker ITO glass slides ($550\mu m$, $15\Omega/sq$), but as the optical transparency still made the height check fail we also added a thin layer of chromium on top of the resist (see Section 3.2 for more details).

All the listed problems slowed down the research in this direction, allowing us the reliable production of only a single substrate to measure. It is our belief that with relatively small effort it could be possible to optimize the recipe and make better nanorods.

The final substrate made was inspected with the SEM and the nanopatterns were found in a regular grid as designed (Figure 4.13). The substrate reveals the ITO coating of the glass

and its structure; the gold nanoparticles look brighter than the ITO background, making their identification feasible. Note that it has been decided not to post process the following images to not distort the original data.
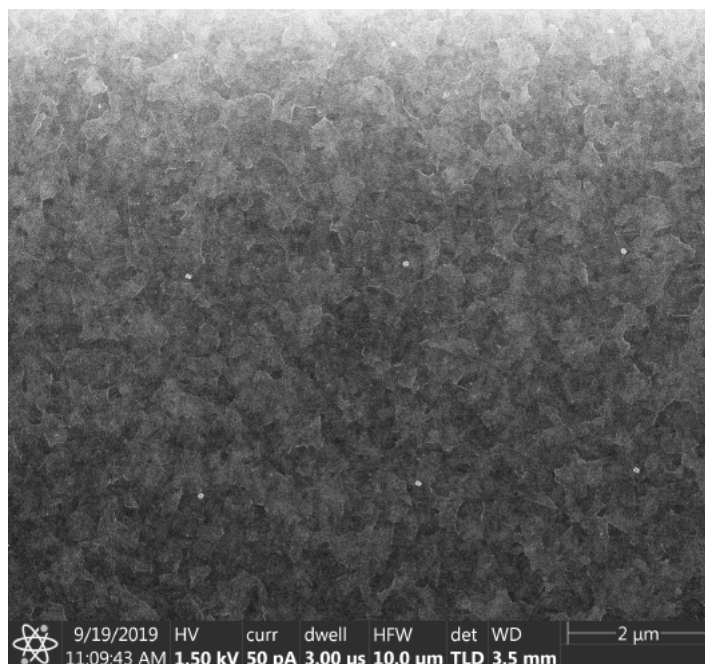
Figure 4.13: Nanoparticles deposited in a regular pattern having $3\mu m$ grid spacing

While the pattern might look good at first sight, when imaging the individual nanoparticles (Figure 4.14) it can be easily seen that the shape is definitely not rod-like, but rather is distorted into an amorphous particle. Unfortunately, none of the produced nanoparticles faithfully resembles a rectangle, but future corrections to the protocol could eventually fix this issue. From area measurements it becomes clear that particles are always broader than expected. Possible explanations include, but are not limited to, something wrong with resist recipe, faulty solubilization during development, chemical stress during etching of the chromium layer.

Figure 4.14: Nanorods distorted into amorphous nanoparticles

4.3   Colloidal gold nanoparticles

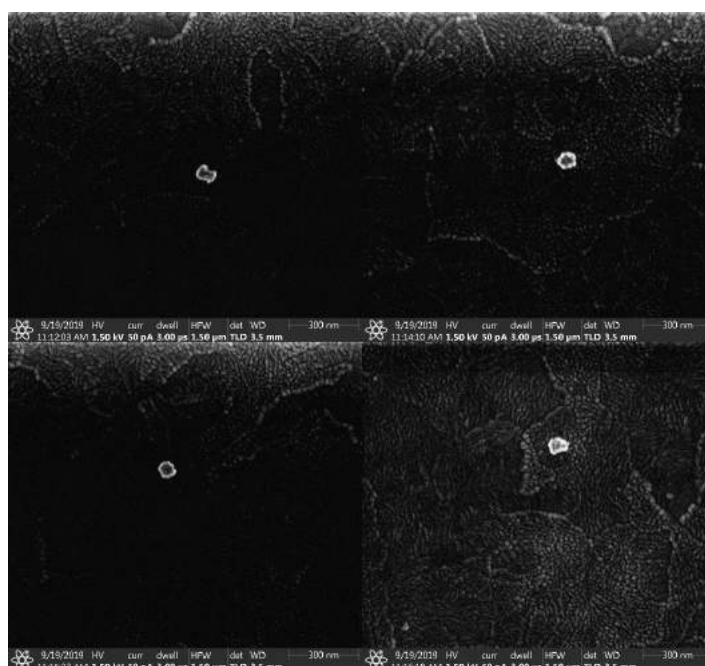The gold colloids presented in this section were all produced following the synthesis protocols explained in detail in Section 3.3 and have been characterized using UV-Vis spectrophotometry and SEM imaging. While the study of the absorbance spectra can give preliminary information on the plasmonic peak position, morphological characterization is fundamental in the comparison with the simulated counterpart. These two techniques define the fingerprint of the synthesized colloids and completely describe them.

In order to maximize the sensitivity of the spectrophotometer all colloids have been diluted in a ratio $1 : 10$ with MilliQ water, with the only exception of the biocompatible nanostars (produced with ascorbic acid) because already diluted enough. All the absorbance spectra are considered in comparison with a blank sample of MilliQ water.

Colloids have been deposited by *drop-casting* onto ITO coated glass in a dilution of $1 : 100$ with MilliQ water and quickly dried with a hotplate at $45°C$ to avoid precipitation in microcrystals and formation of aggregates. The involved volumes are small enough to not be considered hazardous ($< 1ml$) and the entire drying procedure has been carried out inside a ventilated hood. Morphological information was later measured using the free software ImageJ.

4.3.1   Nanospheres

Citrate-capped gold nanospheres were the first to be produced since they have the role of nucleation points in seed-mediated synthesis of nanostars.

In Figure 4.15 the normalized absorption spectrum of the diluted colloid is shown. The plasmonic peak occurs exactly at $520nm$ as predicted by the theory, explaining the ruby red color of the solution. In this case it's impossible to precisely infer the nanospheres' size from this spectrum.
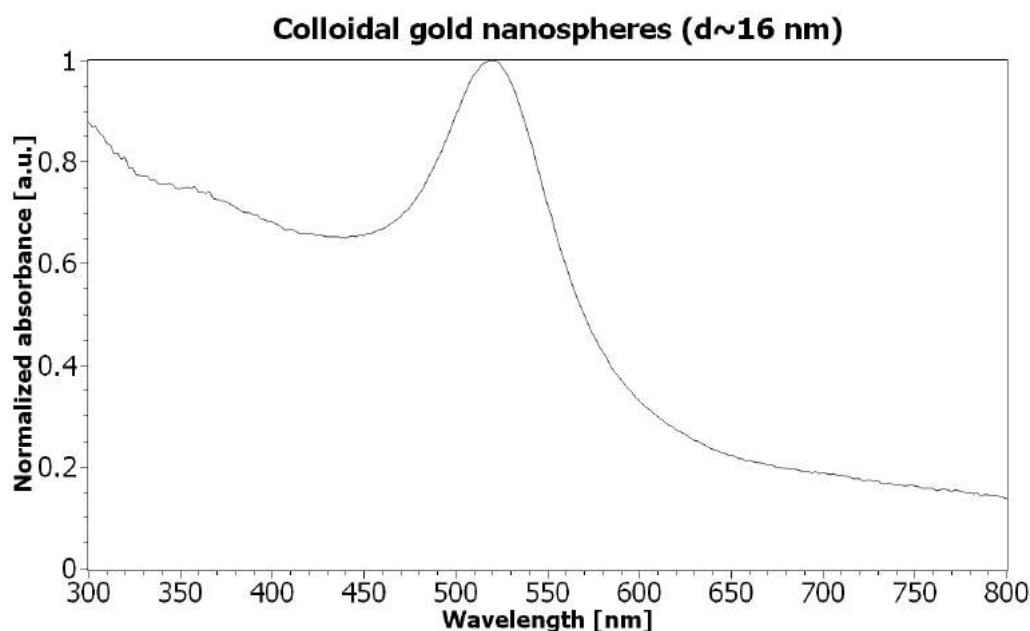

Figure 4.15: Normalized absorbance of gold nanospheres in water

SEM characterization (Figure 4.16) proved not only that the nanoparticles were spherical, but also that their population was monodisperse (Figure 4.17). Even though a bit blurry, the images

taken were easily used to measure the radius of each isolated spot. To minimize human error and small variations from the ideal spherical condition, the radius is calculated indirectly from the measure of the area. The average radius is $\approx 8nm$ and the average diameter $\approx 16nm$.
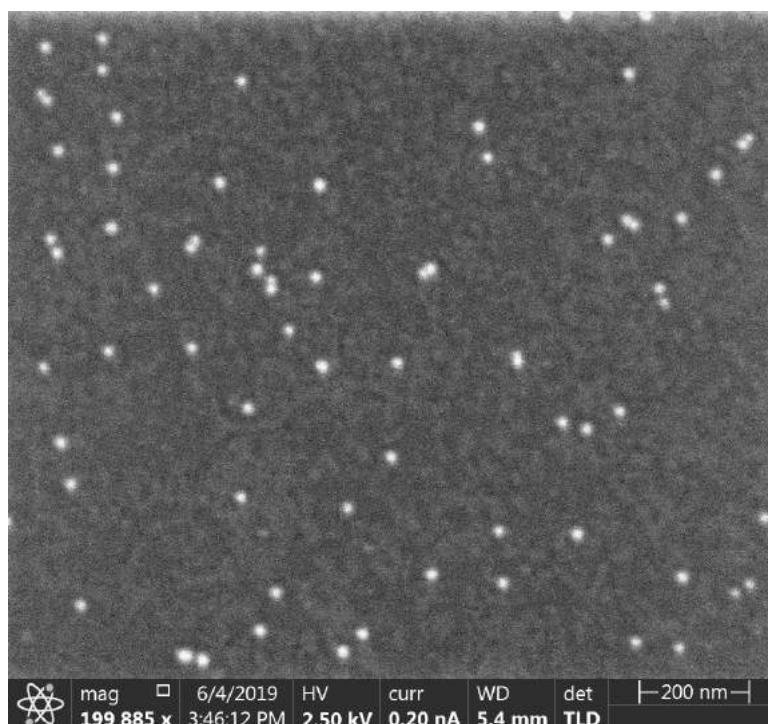
Figure 4.16: Monodispersed citrate-capped gold nanospheres dried on ITO glass

The analyzed results clearly imply that the gold colloid is monodisperse and reliable enough to be used later in the seed-mediated synthesis of nanostars. The citrate capping is expected to be weak enough to be replaced by any other kind of polymer or surfactant.

By keeping the colloid at room temperature away from light sources, it should remain stable over very long time. No degradation is expected to happen anytime in the next few years.
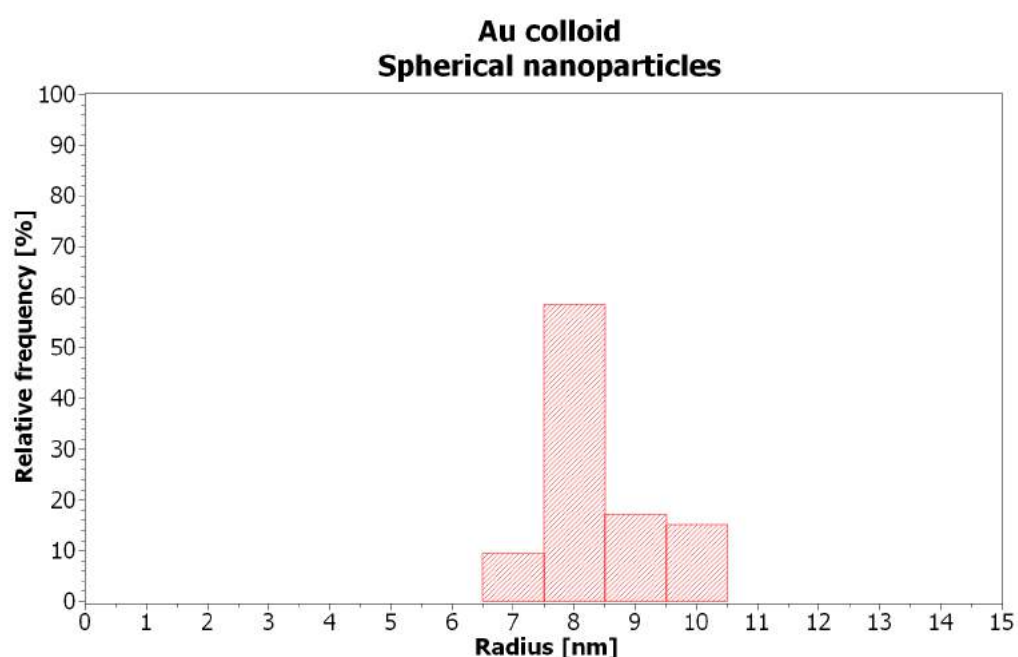
Figure 4.17: Statistical distribution of monodispersed nanospheres' radii

4.3.2 Nanostars in DMF

PVP-coated gold nanostars were synthesized by the seed-mediated protocol explained earlier in Section 3.3, which involved the use of DMF as reducing agent. The very high concentration of PVP favored the formation of many short tips around the gold core. The protocol has been carried out five times so as to test the tunability of the plasmonic peak.
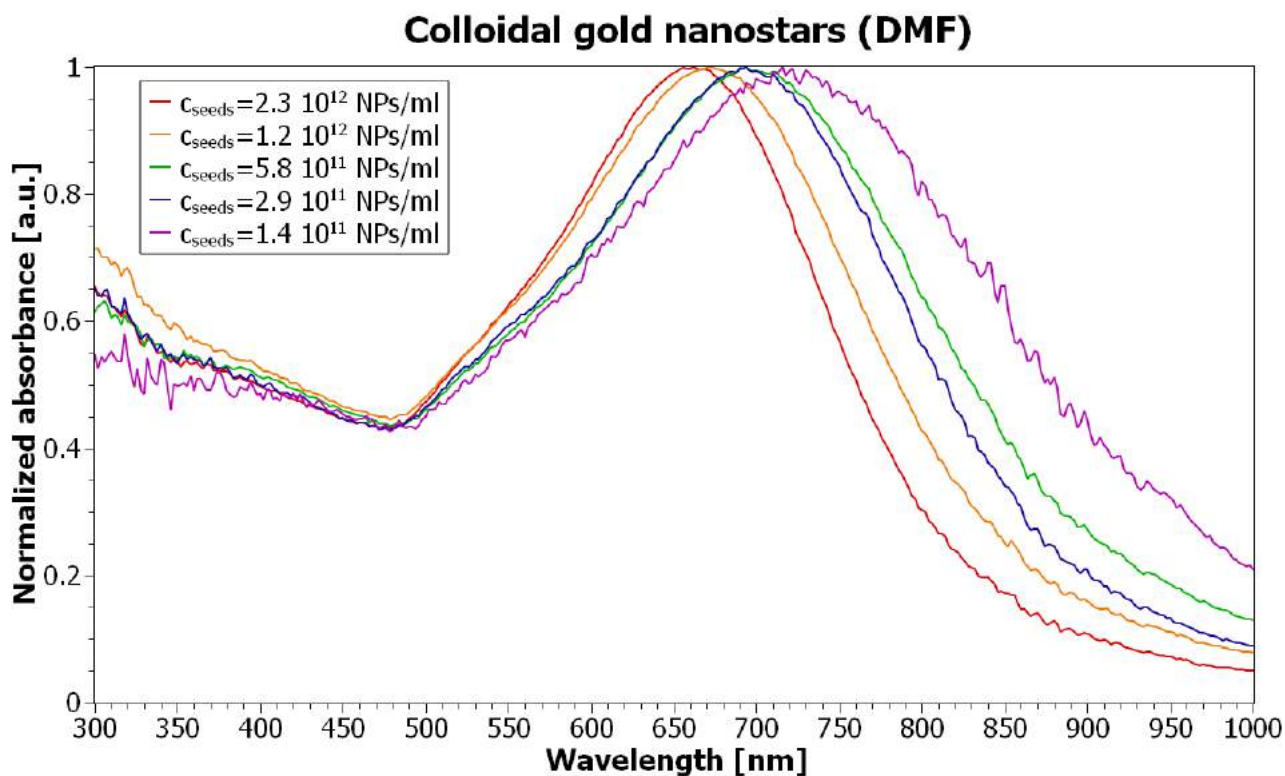
Figure 4.18: Normalized absorbance of PVP-coated gold nanostars in diluted DMF

The spectrophotometric analysis revealed that the five different colloids had slightly different absorbance spectra. The resonance peak is always found around the region of interest of the spectrum ($680nm$), as we also imagined by noting the blueish color of the colloids.

In particular:

c_{seeds} [NPs/ml]	λ_{peak} [nm]
$2.3\ 10^{12}$	662
$1.2\ 10^{12}$	672
$5.8\ 10^{11}$	694
$2.9\ 10^{11}$	694
$1.4\ 10^{11}$	716

Figure 4.19: Position of plasmonic peak dependency on initial seeds concentration

The plasmonic resonance appears to be tunable in a $50nm$ range by simply changing the initial concentration of seeds. By lowering this concentration, however, the peak gets broader hinting a lost monodispersity or the rising of multipolar effects. To better investigate the physics behind these results, SEM images of the different colloids have been analyzed. In Figure 4.20 some significant examples of gold nanostars have been reported.
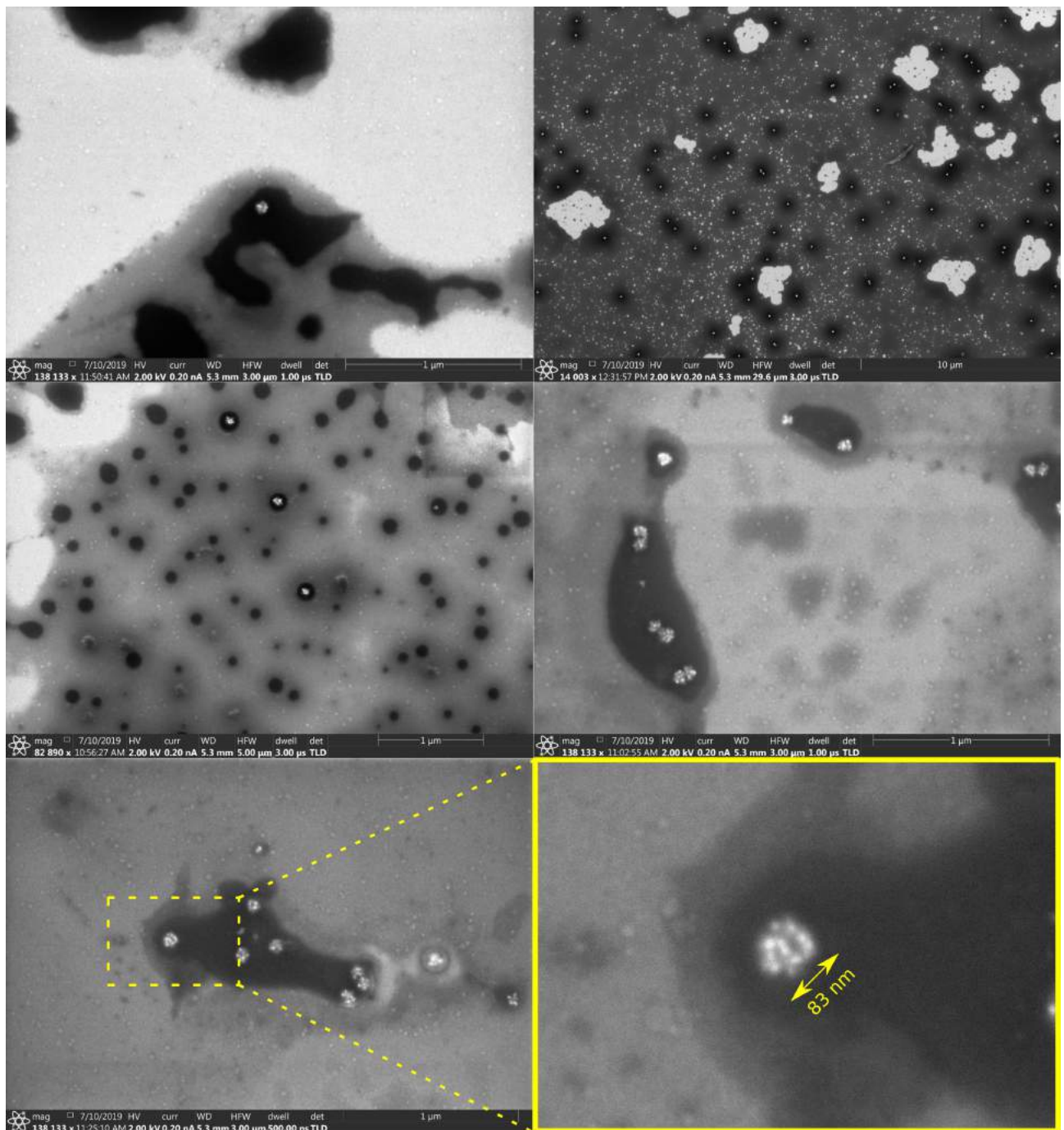
Figure 4.20: Different SEM micrographs showing the gold nanostars (white) surrounded by droplets of PVP (dark gray/black) and bigger gold seeds which have not become stars (light gray dots); top left image represent a strongly diluted sample, while the top right image a not diluted one; bottom right image clearly shows the charging of the nanostar's spikes, appearing brighter to the electron detector

SEM images were not enhanced or modified with any kind of software to faithfully reproduce what measured. We can safely claim that the measured objects are nanostars (and not nanospheres) because of the charging of the sharp tips. As expected, nanostars are coated by PVP; we come to this conclusion by comparing the images of diluted samples with not diluted ones and acknowledging that they are never isolated from such black droplets.

In each acquired image the tip-to-tip distance of the nanostars was measured indirectly from the area of the circle containing them, using the free software ImageJ.

c_{seeds} [NPs/ml]	Seeds Size range [nm]	Nanostars Size range [nm]
$2.3 \cdot 10^{12}$	20 – 40	N.M.
$1.2 \cdot 10^{12}$	20 – 40	50 – 90
$5.8 \cdot 10^{11}$	20 – 35	60 – 100
$2.9 \cdot 10^{11}$	15 – 35	40 – 80 (*)
$1.4 \cdot 10^{11}$	20 – 40	100 – 150

(*) = concentration of nanostars was too low to produce meaningful statistics

Figure 4.21: Ranges of tip-to-tip distance (N.M. stands for Not Measured)

From the above statistics it is possible to define a general trend of production of bigger nanostars when starting with less seeds. In one certain case the sample was too diluted to actually measure enough nanoparticles to make a significant statistic. In the first sample tested (where $c_{seeds} = 2.3 \cdot 10^{12} NPs/ml$) we could not recognize any realistic nanostar, so we assumed that something went wrong during the drop casting of the colloid onto the ITO substrate to image. Further measurements could complete the missing information in Figure 4.21.

In each sample there are always seeds that have grown a bit but didn't become nanostars, keeping their size between $15nm$ and $40nm$. Despite their massive presence, no visible effect appears at $520nm$ in the measured spectra, possibly due to the predominant effect of bigger nanoparticles (since their extinction cross section is much greater).

Micrographs of the nanostars later inspired, as shown in Section 4.1.3, the models used to simulate similar gold nanostars. Although the number of branches in each nanostar differs from case to case, the measured tip radius is often around $5nm$. Estimating a tip length of $10nm$ and considering the ideal condition where the surface is fully covered, the model has been formulated so as to scale the number of spikes proportionally with the core radius.

By comparing the SEM micrographs with the UV-Vis spectra and the relative FDTD simulations we can infer various information:

- Lower seeds concentration translates into bigger, sparser nanostars. This can happen because there are more gold atoms available for each spherical core to grow on;

- Bigger nanostars generally present a broader and more red shifted absorbance spectrum;

- The relatively heterogeneous populations of nanostars made with lower concentrations of seeds correspond to broader plasmonic peaks in the UV-Vis spectra;

- By controlling the initial concentration of seeds, the plasmonic resonance of the colloid can be finely tuned in a certain range;

- Scattering cross section becomes predominant when using a concentration of seeds lower than $\sim 10^{12} NPs/ml$.

Since the produced gold nanostars clearly appear to be resonant with the GEVI of interest, they have been largely involved in the later imaging experiments in combination with fluorescent HEK cells. Up to now, the PVP-coated gold nanostars are the only reliable nanoparticles in tune with the GEVI. While in principle all the five synthesized colloids could be tried to plasmonically enhance fluorescence, the major focus has been on the middle three samples (one having the plasmonic peak at $672nm$ and the other two at $694nm$).

4.3.3 Nanostars in Ascorbic acid

The results shown in this section have been reported for integrity, but they must be regarded as preliminary and incomplete.

Biocompatible (*bare*) gold nanostars were synthesized following the protocol explained in detail in Section 3.3, which involved ascorbic acid as reducing agent and was unfortunately successful only once. UV-Vis spectrophotometry has been employed in order to test if the resonance was in the region of interest (around $680nm$). In fact, if the peak's wavelength had been far from the desired one, the protocol might have been abandoned in favor of a more appropriate one.

Hereafter the absorption spectrum of the synthesized colloid is reported:
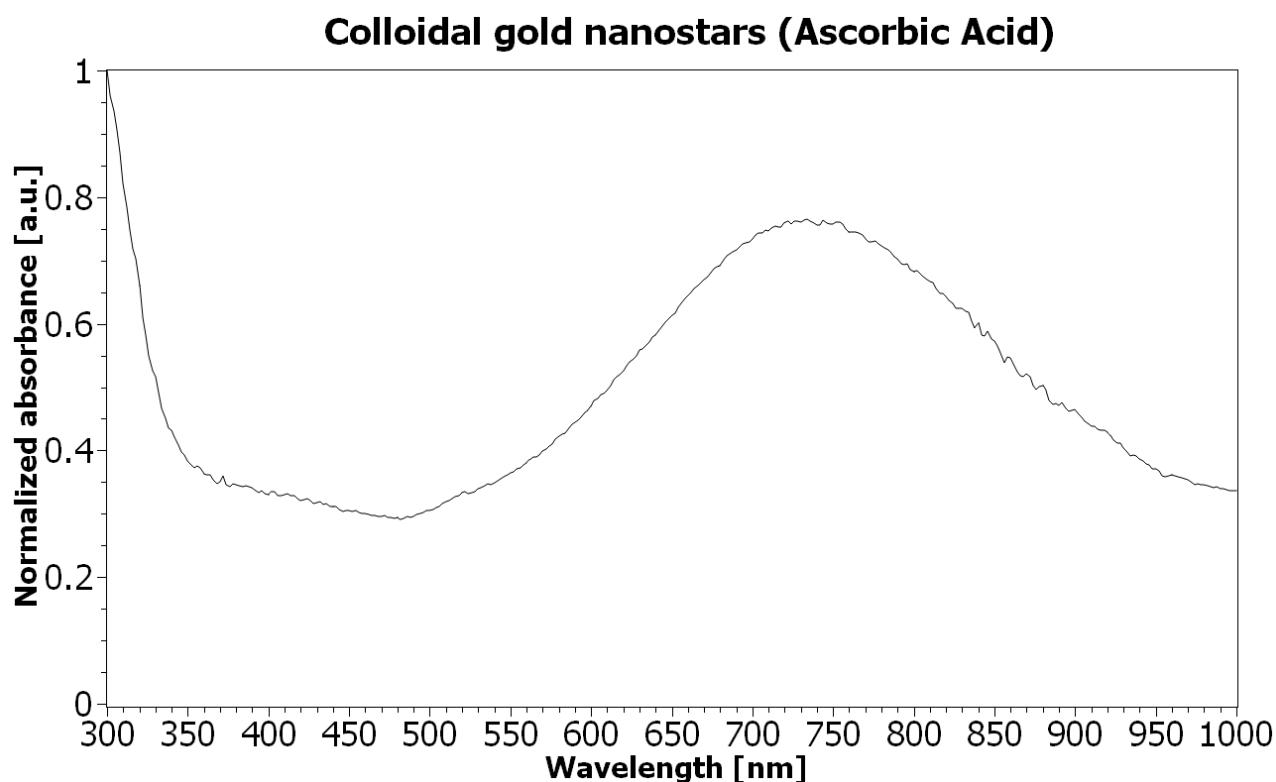
Figure 4.22: Normalized absorbance of gold biocompatible nanostars

From the graph in Figure 4.22 it can be noted that the plasmonic peak is very broad, possibly because of a non homogeneous population of nanostars. The resonance appears to be in the region of interest, so further refinement of the synthesis protocol could achieve better results and higher reproducibility. The ascorbic acid absorption peak's tail is very pronounced towards the UV part of the spectra, compatible with previous measurements [61].

As the colloid must be kept at $4°C$, it is possible that during the time at room temperature undesired effects start to detriment the spectrum from the ideal condition. If this were true, it would bring up other issues related to the application on cells at $37°C$. In this case one solution could be the stabilization of the nanoparticles with some kind of functionalized ligand.

No SEM characterization has been carried out due to both lack of time and limited utility of a colloid not yet reproducible. With more morphological information it would be possible to model the nanoparticles and explain *a posteriori* the measured spectrum.

4.4   MEF of Archaerhodopsin-based GEVIs

The Metal-Enhanced Fluorescence (MEF) mechanism, explained thoroughly in Section 2.3.5, is based on the coupling of a plasmonic nanoparticle with a fluorescent molecule, in our case the Archaerhodopsin-based GEVI. The expected outcome was some kind of very bright fluorescent spot in the cell membrane, which appeared voltage dependent and very well localized.

Many promising papers have shown significant fluorescence enhancements in controlled inorganic samples, but the application to biological systems is rather ground-breaking. For this reason, a shared precise protocol involving both nanoparticles and living cells is, to our present knowledge, still lacking. The general approach adopted is trial-and-error based, meaning each hypothesis we came up with was carefully tested and eventually reformulated. This also implies that a significant part of the time has been spent on unsuccessful experiments.

All the seeded HEK cells were cultured following well established biological protocols, kept at $37.0°C$ and with a CO_2 level set at 5.0%. Transfection of the cells to make them express the GEVI was always done one day before the seeding onto imaging dishes and two to three days before the actual imaging experiment. Cells' health has been constantly verified by checking that their morphology was as described in literature.

The optical setup is common to all experiments and described in Section 3.6. The camera has a pixel size of $6.5\mu m$, so accounting for the magnification of the system of 27.8 we obtain a resolution of about $235nm$ which is close to the ideal optical limit. In reality, diffraction-limited spots will occupy approximately $3 - 4$ pixels in each direction. The most meaningful tests are hereafter reported in an thematically organized way.

Nanorods pattern

The substrate obtained with EBL was tested with HEK cells expressing NovArch (a variant of ArchD95N). Our hope was based on the eventual possibility of a bunch of nanoparticles being randomly resonant with the fluorophores, despite their highly variable amorphous shape. Far from the optimal condition, this situation would have been considered only a preliminary result, but it would have established a first draft of the protocol to reproduce the experiment.

We decided not to coat the substrate with fibronectin before seeding transfected HEK cells on it, because we expected such kind of molecular matrix to completely isolate the nanopattern from the actual cells. Furthermore, we were hoping that the nanorods would have contributed to the formation of a rough surface, favorable to cell adhesion.

To make the glass slide fit in the stage of the microscope, we bought a suitable $22mm$ x $22mm$ holder and fixed it into a plastic holder that has been custom made with a 3D printer.

It has become clear after the first wash with Phosphate-Buffered Saline (PBS), the cells were not adhering to the substrate. Even if the procedure has been carried out with particular care, the remaining cells were too sparse to find significant fluorescent signal to measure. Moreover, some of the remaining cells started floating in the extracellular solution, making this measurement even harder.

From such experiment we can understand that the adhesion problem must solved before future tests involving gold nanorods. It should be verified that the fibronectin coating included in the standard protocols is thin enough (less than $4nm$) to let the nanoparticle-fluorophore coupling happen; otherwise, gold-binding linker molecules could provide such selective adhesion to specific cell parts.

Colloidal nanostars coupled to purified protein

ArchD95N protein has been overexpressed in *E. coli* and purified following the original standard protocol [18]. Like all membrane proteins, ArchD95N is not hydrosoluble, so the membrane phospholipids have been replaced with a detergent.

In the control imaging dish we plated $10\mu l$ of gold nanostars and let them dry overnight at room temperature. When looked at under green light in the optical microscope, diffraction limited spots appear and blink on the same focal plane of the bottom of the dish, confirming their presence. We would expect a similar photoluminescence when looking at the purified protein dropped onto such dishes, other than the expected enhancement under red light.
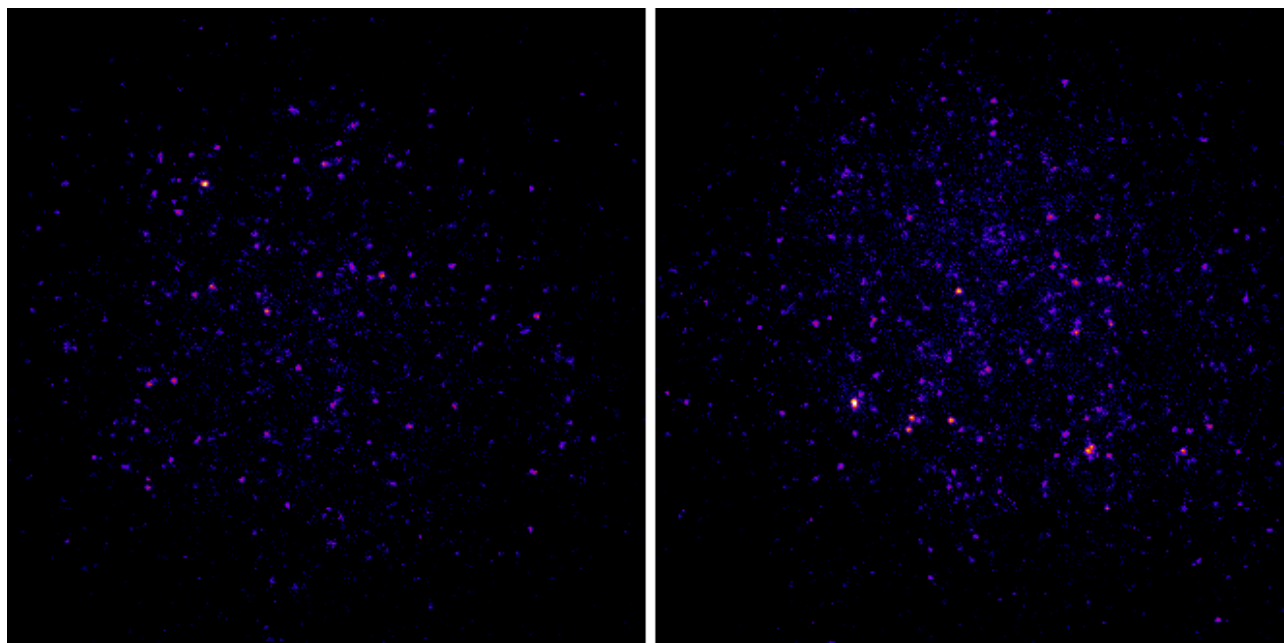

Figure 4.23: Photoluminescence of gold nanostars excited with green light in control dish. Look Up Table (LUT) has been set to "Fire" and contrast and brightness have been adjusted to highlight the signal coming from the nanostars. FOV = $115\mu m$ x $115\mu m$

In the dish combining both protein and nanostars we couldn't find such diffraction limited structures but bigger aggregates, similar to stains (Figure 4.24). We still haven't proposed any interpretation of such data other than some kind of interaction between the hydrophilic environment around nanostars and the hydrophobic protein solution.

Under green light the protein is less excitable and consequently less fluorescent, so we can focus on a plane where the stains appear to be, while under red light the fluorescence of the protein blurs the whole image and slightly highlights the aggregates found under green light.

Fluorescence signal in correspondence of the stains has a brightness at most of double of the intensity of the surroundings, but the spots are way above the resolution limit (so they are not isolated nanostars). Apparent plasmonic enhancement is not as high as predicted either.

Purification protocol is rather time consuming, so this test has been tried only once. As in later experiments, the real issue we encountered is the precise localization of the nanostars so as to easily compare the fluorescence signal with and without it. Furthermore, we fear that the protein is drying or degrading, because when looking at the bright-field image after laser illumination we have found even stranger fractal-like stains (Figure 4.25).
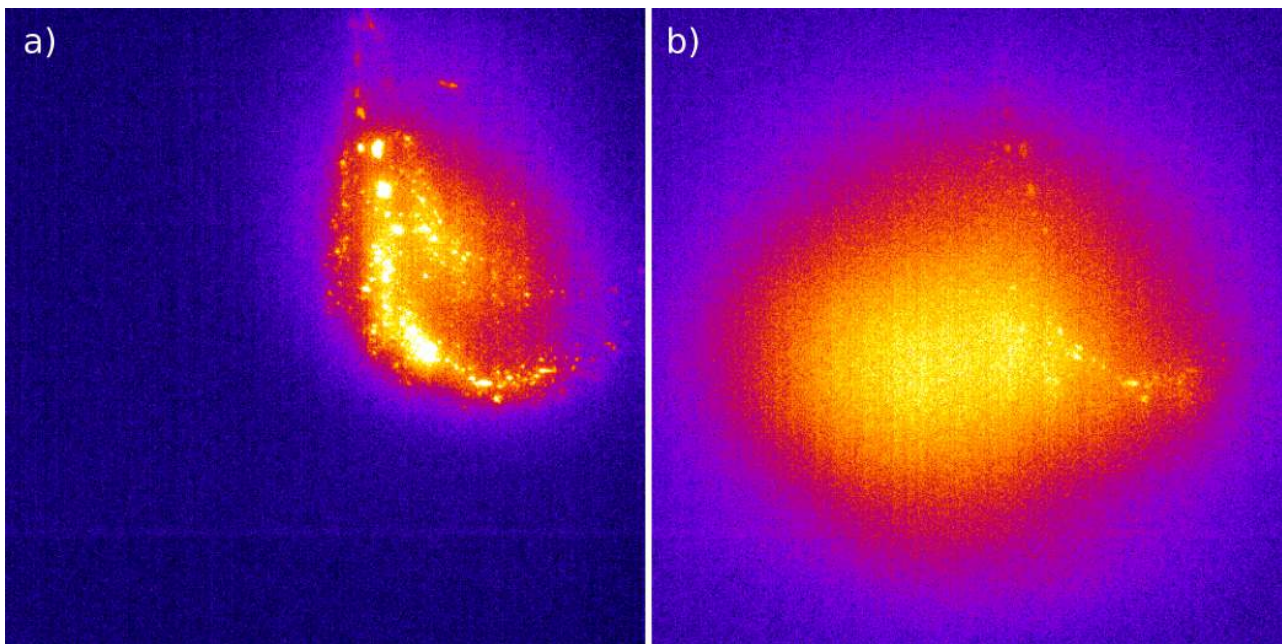
Figure 4.24: ArchD95N protein on gold nanostars under a) green light and b) red light. Look Up Table (LUT) has been set to "Fire" and contrast and brightness have been adjusted to highlight the signal. FOV = $235\mu m$ x $235\mu m$
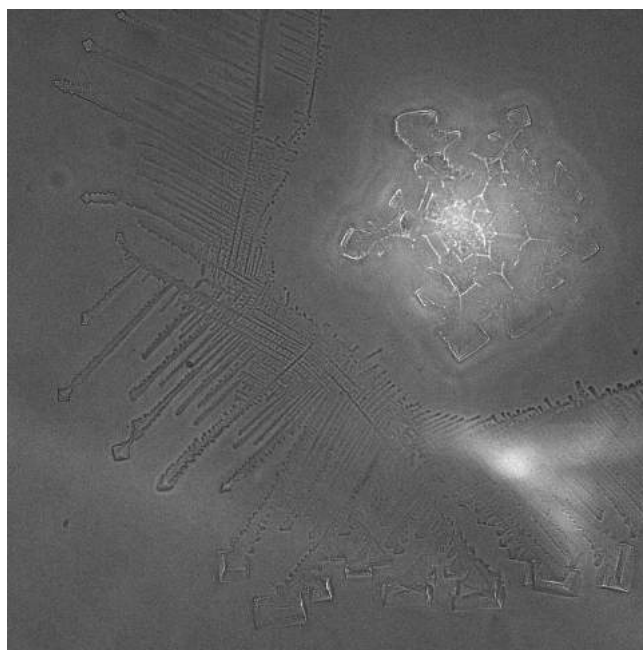
Figure 4.25: Bright-field image of purified protein on nanostars surrounding laser illumination of the sample. Brightness and contrast have been auto-adjusted. FOV = $445\mu m$ x $445\mu m$

Colloidal nanostars added dropwise onto cells

After the previous attempt of measuring the plasmonic enhancement in the purified protein, gold nanostars have been tested directly on fluorescent cells. The first approach to the problem involved the monitoring of certain selected cells before and after the dropwise addition of $10\mu l$ of colloid diluted in PBS, directly in the extracellular medium. This would have in principle the advantage of directly quantifying the fluorescence enhancement by comparing the optical signal before and after the interaction with the nanoparticles, needing no extra control dishes.

Unfortunately, this kind of protocol didn't work as expected. In fact, even a single drop in the dish could perturb the system, making the cells displace and deform just enough to make their images not comparable with the previous ones.

Qualitative comparison between images shows no significant general or local enhancement in the fluorescence signal and in certain cases the signal appears even lowered/quenched. It is possible that the nanostars might just be floating around in the extracellular medium, never getting too close to the cell membrane despite their high concentration.

This experiment evinced that we needed a different way to fix the nanoparticles to the cell membrane. The natural approach became then the plating of the nanostars *under* the cells, by trying to include them in the underlying fibronectin matrix.
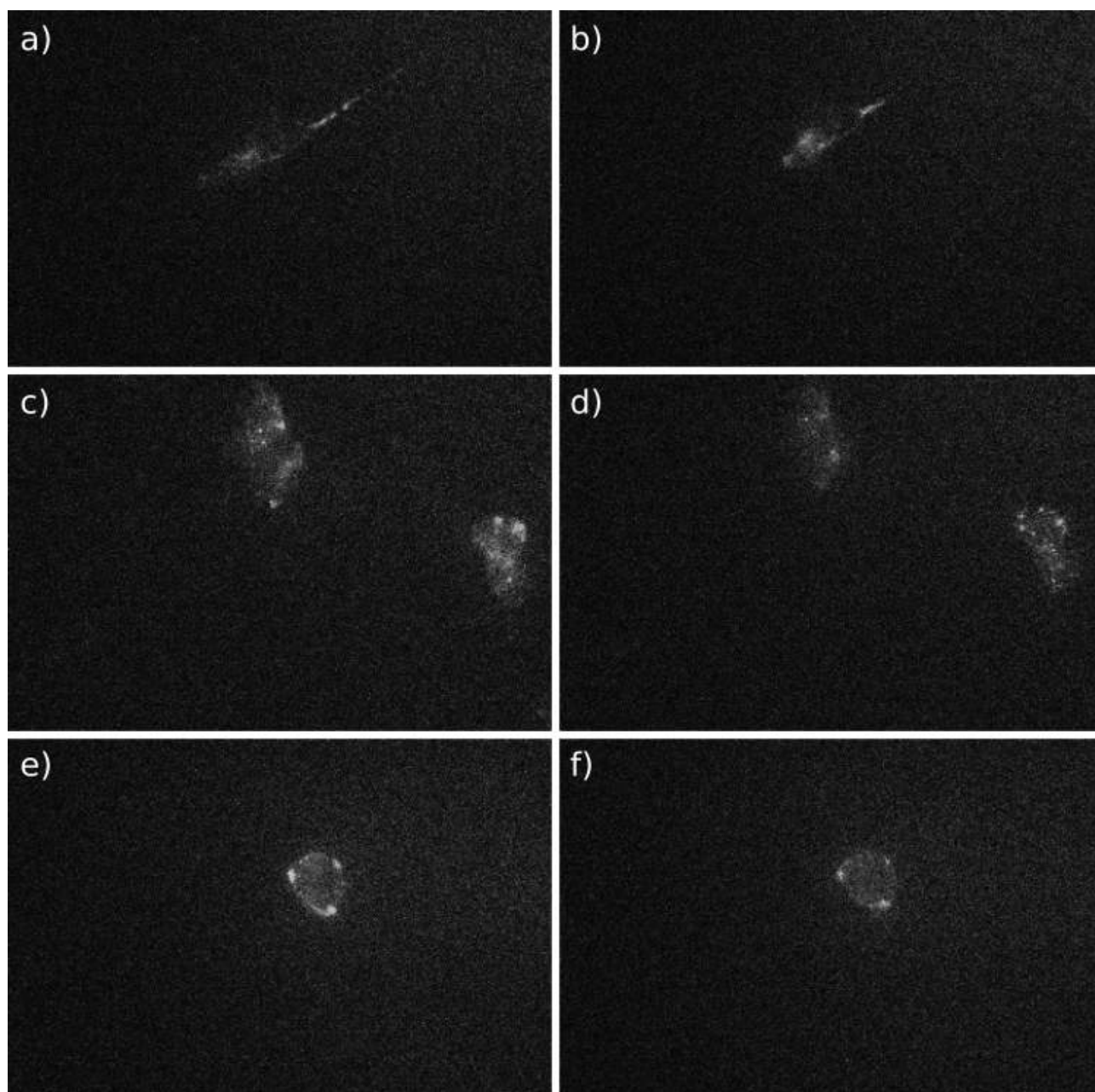
Figure 4.26: Fluorescence imaging of HEK cells before (left column) and after (right column) addition of colloidal nanostars. From a) to b) there is a significant change in cell's shape, from c) to d) there is a lowering of the signal, from e) to f) the cell is displaced and slightly rotated. All the images are obtained by removing the background noise, have a FOV of $335 \mu m$ x $220 \mu m$ and are captured with a frame rate of $75 fps$

Colloidal nanostars added dropwise onto fibronectin coating

The last and maybe most rewarding approach, as suggested by previous experiments, was based on the addition of $10\mu l$ colloidal gold nanostars onto the fibronectin coating, *before* the plating of the cells. In this way we would expect the nanostars to be directly included in the fibronectin matrix, to which the cells directly attach to, bringing the proteins in contact with the nanoantennas. We also speculated that some nanostars could be uptaken and have a role in the fluorescence enhancement from the internal side of the membrane.

The testing of photoluminescence in presence only of nanostars could confirm their embedding in the fibronectin coating. Under red light the signal was extremely weak, barely possible to quantify, as expected. Under green illumination the nanostars show a stronger intermittent photoluminescence. When scanning the focal plane on the z direction we can easily find a limited window where the signal comes from, confirming that the nanostars are present in a rather thin superficial layer. A short recording of the blinking nanostars has been post-processed to sum the intensity in all the frames and highlight the positions of the particles.
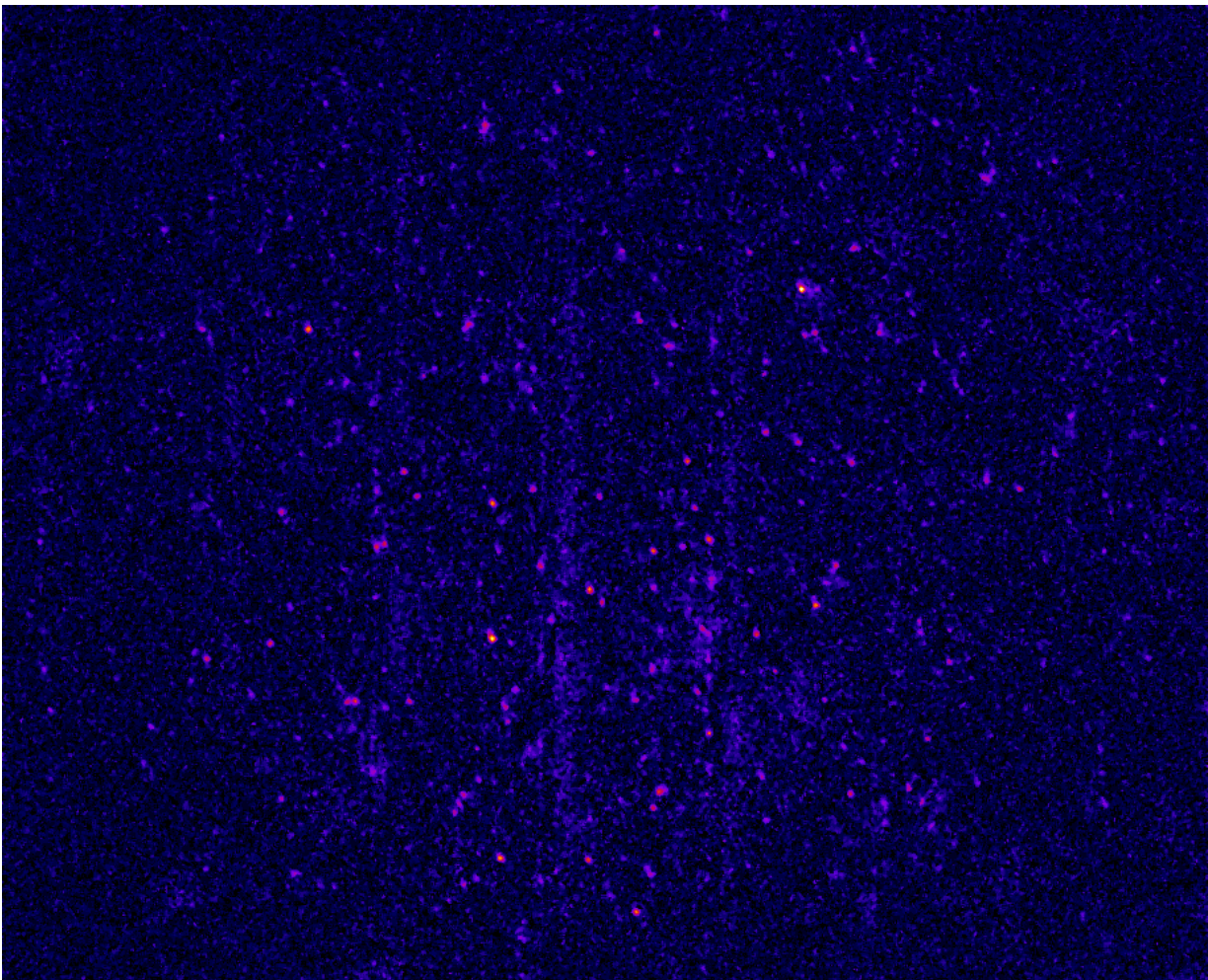
Figure 4.27: Photoluminescence of gold nanostars in fibronectin matrix under green illumination. Frames have a FOV of $214\mu m$ x $173\mu m$ and are captured with a frame rate of $75fps$; during post-processing the frames were summed, contrast and brightness regulated and LUT set to "Fire"

The results are very similar to the ones obtained in Figure 4.23, being for all practical purposes the same experiment. Measurement and analysis of the FWHM of each spot confirms that they all come from diffraction limited sources, in this case nanometric gold nanostars.

The initial hope was to find the same localized diffraction-limited spots also in cells, so when first measuring the fluorescence of ArchOn expressed in HEK cells we originally believed to have found them (Figure 4.28 - a,b,c). However, a simple comparison with some control cells plated on fibronectin *without* the embedded nanostars (Figure 4.28 - d,e,f) has revealed that such bright spots are naturally occurring in the cell regardless the presence of plasmonic particles.
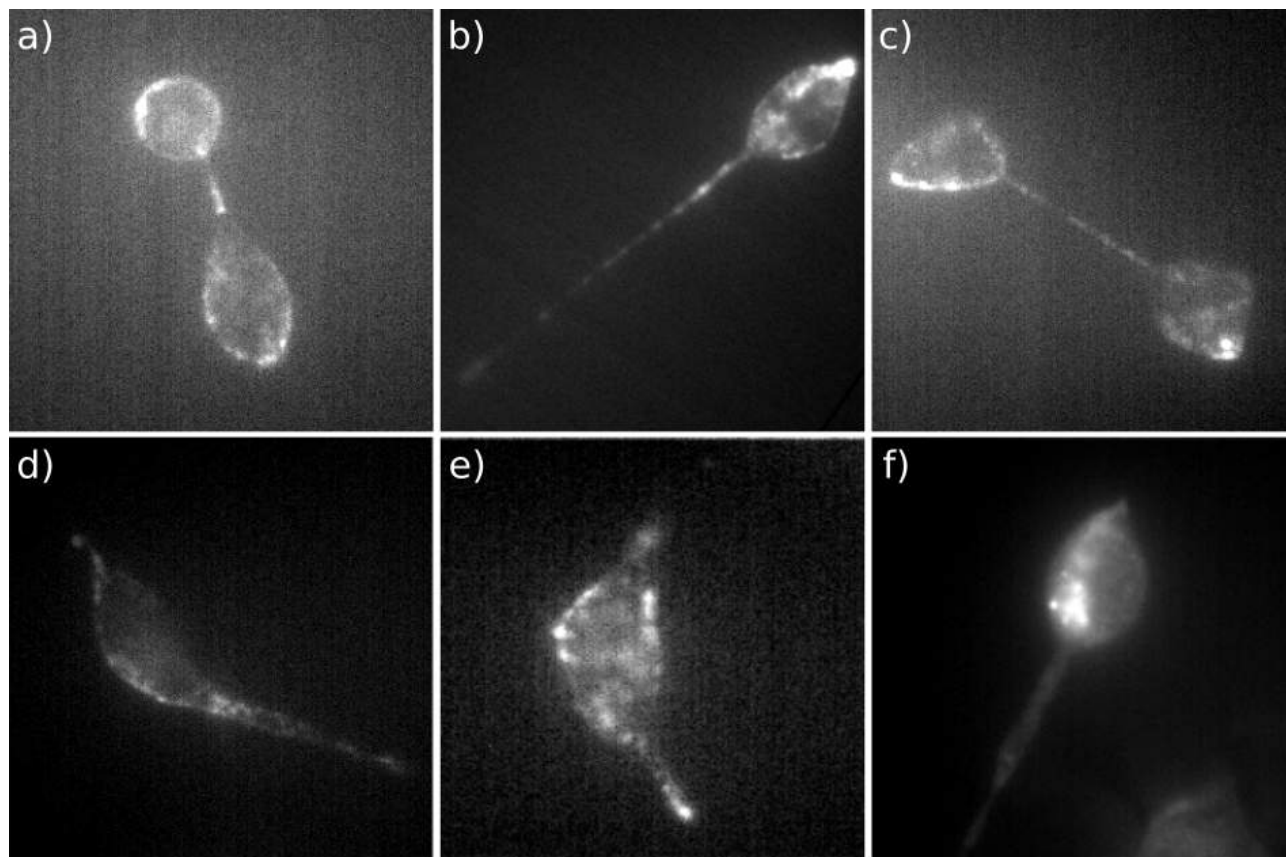
Figure 4.28: Comparison between a-c) cells seeded on nanostars and d-f) control cells. All the images have a FOV of $70\mu m$ x $70\mu m$ and are captured with a frame rate of $75 fps$; exposure time is $5ms$, contrast and brightness have been adjusted to highlight the fluorescent spots

The measured bright spots could easily be interpreted as protein aggregates, caused by overexpression of the protein. These aggregates could be at the cell membrane, or in the cytoplasm. In the former case they would still be voltage sensitive, but not in the latter.

To test whether the spots were localized only at the bottom of the cells (ideally nearby the fibronectin layer) and not everywhere in the membrane, Z scans were carried out to roughly reconstruct the 3D structure of the cell. Depending on the size of the cell, the focal plane was scanned between $15\mu m$ and $50\mu m$ along the vertical axis. Results confirmed that the bright spots are present everywhere in the cell membrane. As the illumination is in wide field mode and does not harness confocal microscopy, inevitable blurring of the signal makes it difficult to precisely tell if the spots are just in the membrane or isolated inside the cytoplasm. If the signal were eventually coming from the plasmonically enhanced proteins, that would mean that the nanostars have been uptaken by the cells.

At this stage it was impossible to draw strong conclusions, as the clear identification of the origin of such bright signal is still elusive. An additional experiment carried out involved the correlation between 2P photoluminescence of gold and 1P fluorescence of the spots, to try to verify the presence of the nanostars nearby the higher signal. We abandoned this kind of test

because we have found great difficulty in perfectly aligning the images, both in the XY plane and in the Z. Switch between the two configurations is very time consuming and can lead to unreliable experiments.

The decisive experiment was in the end the test of voltage sensitivity of the fluorescent bright spots found in previous attempts. To carry out such kind of measurement, we used a classical patch clamp system in parallel with the optical microscope. In this way we are able to control the voltage and at the same time to measure the fluorescent signal.

HEK cells expressing NovArch were plated on the nanostars-embedded fibronectin like in previous experiments. The glass micropipette used had a resistance of $R_{pip} = 5.7M\Omega$, optimal for stable patch clamp. After sealing the membrane in the whole-cell configuration, the system was illuminated by the red laser and voltage set to be a square wave between $-30mV$ to $70mV$, with frequency $1Hz$.

The obtained recording (at $75fps$, exposure time $2ms$) was analyzed first to check the voltage sensitivity of the whole cell, as shown in Figure 4.29. To do this, the overall fluorescence intensity has been plotted. As expected, the GEVI has a fluorescence that is higly correlated to the command voltage sent.
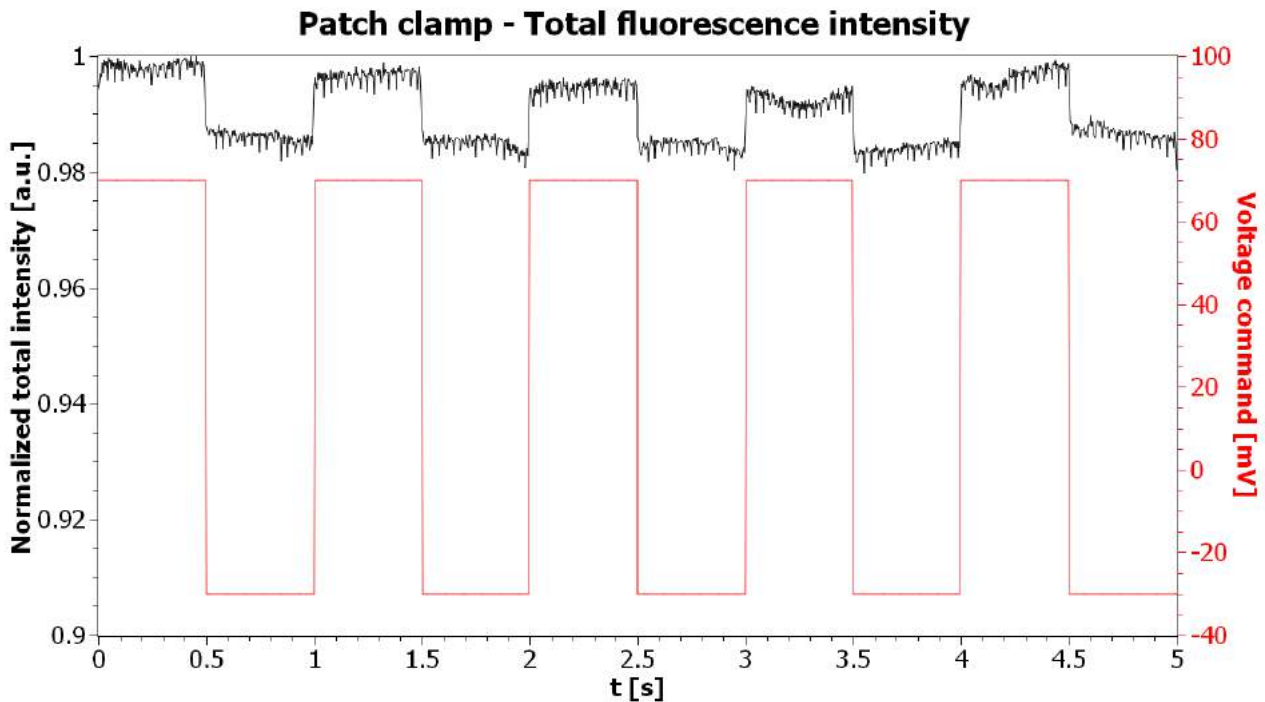
Figure 4.29: Total fluorescence intensity over time during patch clamp experiment (voltage clamp configuration). Note that the noise in the fluorescence signal is mainly coming from the optical noise coming from the camera

The next step in this experiment was to create a pixel-by-pixel correlation image with the overall fluorescence intensity, to clearly see if the bright spots are actually voltage dependent. If the pixel is not correlated to the signal than it would be darker, while if it is correlated it would look brighter. Intracellular aggregates' fluorescence should not be dependent on the voltage, so they're expected to look as dark spots.

The obtained correlation image (Figure 4.30) surprisingly shows that the spots are indeed voltage sensitive, like the rest of the cell membrane. The lack of internal black parts lead us

to the conclusion that if the spots are due to local higher concentration of protein, than they must be in the cell membrane and not in the cytoplasm. Because of a lack of time, we couldn't perform the experiment in the same conditions for the control cells, nor a statistically significant study involving the nanoparticles. The success of this very last measurement is however very much encouraging us to keep pushing the project forward.
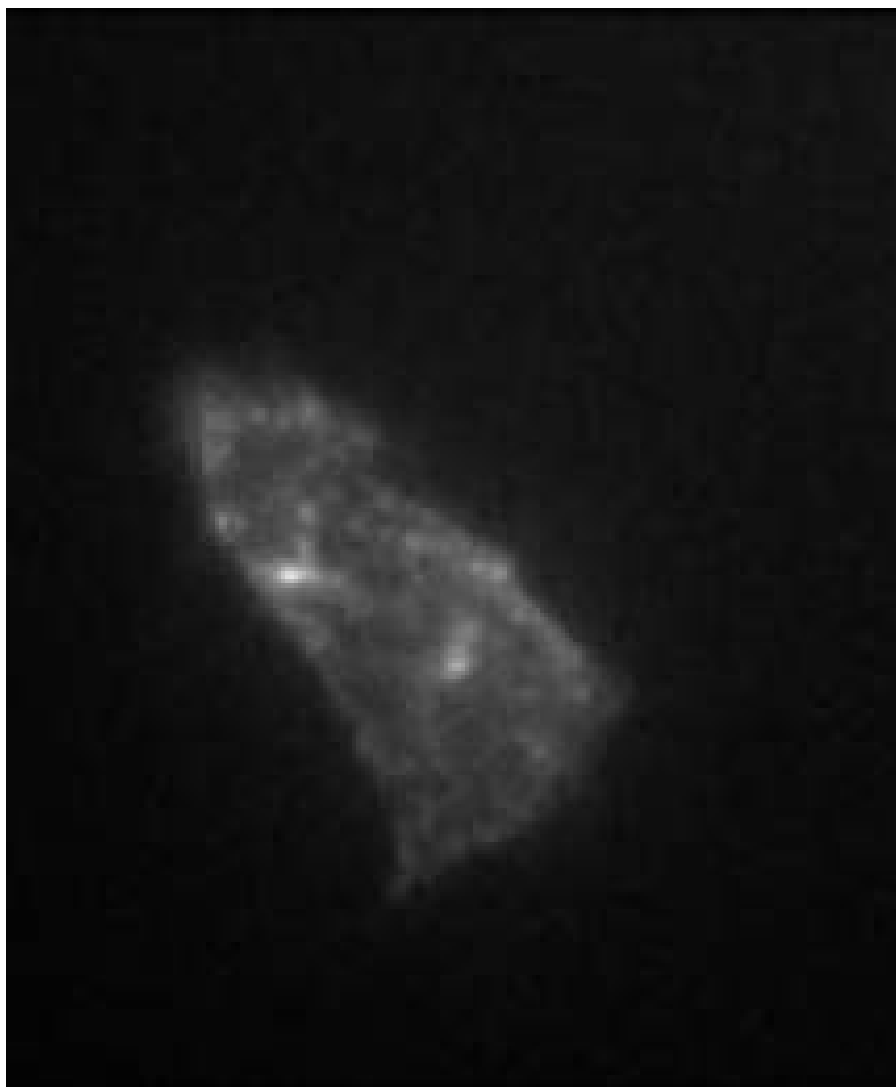
Figure 4.30: Correlation analysis between each frame and total intensity, where brighter pixels indicate higher correlation with voltage variations. Each frame has an exposure time of $2ms$, FOV $= 50\mu m$ x $61\mu m$. During the post processing, despeckling of the image helped removing the broken pixels not dependent on the voltage

Chapter 5

Conclusions

Strong statements in biology are always very hard to formulate, because of both high complexity of the systems and high trial-to-trial variability. Nevertheless, a systematic approach to the problem can help discarding wrong assumptions and, eventually, can bring up new logical hypothesis to test.

Neurophotonics is a new and multidisciplinary field, intriguing but also challenging. In this thesis I've approached the production and application of gold nanoparticles to enhance fluorescent proteins reporting membrane potential. My main motivation in starting this project was a fascination for the possibilities that new technologies provide us in garnering a detailed understanding of the physics underlying the biological functions of complex systems like neurons and, eventually the brain. However, the fact that the field is in its infancy also means that experimental protocols are far from standardized yet. This is especially true for my project, combining novel voltage sensitive proteins with concepts from nanophotonics.

The computational approach was in the end very successful and the simulated features of nanoparticles were strongly supported by the theory and verified experimentally. Study of the average field enhancement near the plasmonic particles allowed for the optimization of the parameters, while study of the cross sections (absorption, scattering and extinction) unraveled the different contributions influencing plasmonic resonance. Simulations were also used to explain *a posteriori* the measured absorbance spectra of the gold colloids produced.

Electron beam lithography of gold nanorods proved itself more challenging than expected, but in the end the last nanopattern made represented a promising start for future refinement of the protocol. The biggest issues encountered were related to the use of thin glass samples coated with a thin conductive layer, which were easily breakable and difficult to focus on in the EBL procedure because of high transparency. The proposed solutions (use of thicker glass, chromium layer on top of the device, fibronectin coating to enhance cellular adhesion) will need to be adapted in the optimal recipe, yet to be formulated.

The best and most encouraging results have been obtained with colloidal synthesis of gold nanostars, showing a plasmonic resonance that is tunable around the emission peak of the protein. The established synthesis protocol of PVP-coated nanostars is reliable and relatively easy to carry out. Full morphological and spectroscopic characterization of the produced nanoparticles completes the knowledge necessary to predict and control their plasmonic resonance.

An extensive part of my work focused on the direct test of gold nanoparticles on fluorescent model cells, to measure the metal enhanced fluorescence nearby the voltage sensitive proteins. The last patch clamp test carried out seems to point out that the diffraction-limited fluorescent

spots are voltage dependent. Previous measurements on control cells suggest that signal from intracellular aggregates is not correlated to the membrane potential, so by comparison we are convinced that the localized fluorescence comes directly from the cell membrane. Evident and unequivocal enhancement was however not found. The common issue frustrating these experiments is the the uncertainty of the position of the nanoparticles relative to the cell membrane.

The initial approach to this project involved using EBL to write nanostructures at well defined positions. This approach should be revived and optimized as it provides a crucial intermediate step in quantifying and characterizing plasmonic enhancement of cell-membrane localized molecules in controlled circumstances. The next steps in this project will have to overcome this uncertainty and establish a strong correlation between diffraction limited spots and colloidal plasmonic nanoparticles. This can be achieved by functionalizing the nanoparticles to bind to the cell membrane or membrane proteins. This is also crucial for the next phase of the project, to link nanostars to dendritic spines of neurons via scaffold proteins naturally expressed only in those subcellular compartments.

Precise control over localized fluorescence enhancement could unveil subcellular voltage dynamics without losing information about the surrounding environment. Reaching this important milestone is becoming more and more realistic in the near future, but many obstacles still remain. All the experiments in this thesis brought deeper insight on the challenges facing a project combining nano- and neurophotonics, and stronger desire to overcome them. Apart from providing the theoretical underpinnings to make this happen, my thesis describes a large body of work focused on the experimental falsification of hypotheses on the right design for nano-neurophotonic experiments; the insights gained will be used to make nanoscopic voltage imaging reality.

Chapter 6

Acknowledgments

🇮🇹

🇪🇺

Questi cinque anni universitari sono stati per me un'avventura, e nessuna avventura è tale senza gli opportuni compagni di viaggio. A tutte le persone che hanno contribuito ad essere quello che sono oggi, dedico questi sinceri ringraziamenti.

Il primo grande *hartelijk bedankt* va a **Daan Brinks**, che sin dalla prima email mi ha accolto nel suo laboratorio facendomi sentire parte di un progetto emozionante. Fin da subito mi sono trovato in grande sintonia con la sua ambizione, il suo entusiasmo e la sua passione, rappresentando così un importante punto di riferimento professionale. Lo ringrazio anche per la grande fiducia nelle mie capacità e per avermi offerto la possibilità di proseguire questo progetto con lui, darò il massimo per non deludere le sue aspettative.

Un dovuto grazie va ad **Ornella Cavalleri**, che ha accettato di supportarmi in questa tesi con grande positività. Mi sono innamorato della biofisica al terzo anno grazie al suo corso, insegnato con passione assieme ad **Alessandra Pesce**, per cui se tutto questo è stato possibile è anche merito loro. Ringrazio **Claudio Canale** per la sua supervisione, per i preziosi consigli pratici e per la gentilezza sempre dimostrata. Grazie in generale a tutto il **gruppo di biofisica del DIFI**, che ha sopportato la mia continua presenza negli ultimi tre anni e ha rappresentato un ambiente amichevole e rilassato in cui confrontarsi.

These five university years were for me an adventure, and no adventure is such without the appropriate traveling companions. To all the people who contributed to be what I am today, I dedicate these sincere thanks.

The first big *hartelijk bedankt* goes to **Daan Brinks**, who welcomed me into his laboratory from the first email making me feel part of an exciting project. From the beginning I found myself in great harmony with his ambition, his enthusiasm and his passion, thus representing an important professional role model. I also thank him for the great faith in my ability and for giving me the opportunity to continue this project with him, I will give my best to not disappoint his expectations.

A due acknowledgment goes to **Ornella Cavalleri**, who agreed to support me in this thesis with great positivity. I fell in love with biophysics during the third year thanks to her course, taught with passion along with **Alessandra Pesce**, so if all this was possible it is also thanks to them. I thank **Claudio Canale** for his supervision, for the valuable practical advice and for the kindness always demonstrated. Thanks in general to the whole **DIFI biophysics group**, which has endured my continued presence for the past three years and has been a friendly and relaxed environment to confront in.

Un misto di *grazie*, *thanks* e *bedankt* va a tutti i miei amici e colleghi di Delft, seconda famiglia lontano da casa. Un grande abbraccio a **Vidya**, 鑫 (**Xin** per gli amici), **Nicolò**, **Laura**, **Cristiano**, **Ryan** (spaghetti≠noodles), **Aya**, **Bregje**, **Nahum**, **Beth**, **Leonie**, **Aditi**, **Mike**, **Stef** e a tutti coloro che hanno reso il mio Erasmus indimenticabile. Grazie in particolare allo "svedese" **Carel** per il suo lavoro in cleanroom e grazie di cuore ad **Anjella** per tutto il supporto, senza il quale starei ancora cercando una casa.

Se gli ultimi cinque anni sono stati i più belli della mia vita è anche merito di un gruppo di amici con cui ho condiviso le giornate in università, in classe e in laboratorio ma anche lontano dai libri. Un grazie allora a tutti gli amici del **partito del Nocciolino**, fondatori e membri onorari, per le lunghe discussioni politico-filosofiche, per il conforto nei momenti difficili e soprattutto per tutte le risate. Non voglio dilungarmi troppo, ma ci tengo a mandare un abbraccio fortissimo ad **Alba**, **Denise**, **Beatrice**, entrambe le due **Eriche**, **Daniele** e **Nicolò**. Terrò nel cuore tutti i bei momenti passati, per sempre. Stiano tranquilli che, per quanto lontano io sia, non si libereranno di me facilmente!

Un grazie agli amici "storici", che mi hanno visto crescere e sono cresciuti con me. Parlo di **Alice**, **Esther**, **Ambra**, **Marta**, **Valentina**, **Roberta** e **Micol**, ma anche di amici più lontani come **Eleonora** e **Matteo**, con i quali condivido un legame immune al tempo e alla distanza. Anche per tutti questi avrei mille cose da dire, ma mi limito ad una parola: *grazie*. Posso sempre contare su di loro, e sanno che questo è reciproco.

Ringrazio il Teatro, come forma di arte e di espressione personale, perché oltre ad avermi fatto conoscere persone meravigliose come **Ilaria**, **Anna** e **Matilde**, mi ha anche fatto conoscere meglio me stesso. Un grazie a tutti gli amici di musical, per avermi fatto vivere un sogno che ho tenuto nel cassetto per troppo tempo, e grazie in generale a tutti coloro che negli anni hanno condiviso il palcoscenico e le emozioni con me.

Prima di concludere questa lunga dedica, ho promesso a me stesso di ringraziare **Wikipedia**,

A mix of *grazie*, *thanks* and *bedankt* goes to all my friends and colleagues in Delft, my second family away from home. I send a big hug to **Vidya**, 鑫 (**Xin** for friends), **Nicolò**, **Laura**, **Cristiano**, **Ryan** (spaghetti≠noodles), **Aya**, **Bregje**, **Nahum**, **Beth**, **Leonie**, **Aditi**, **Mike**, **Stef** and to all those who made my Erasmus unforgettable. Thanks in particular to the "svedese" **Carel** for his work in the cleanroom e thanks from the heart to **Anjella** for all the support, without which I'd still be looking for a house.

If the last five years have been the most beautiful of my life, it is also thanks to a group of friends with whom I shared the days in the university, in the classroom and in the laboratory but also away from the books. Thanks, then, to all the friends of the **Nocciolino party**, both founders and honorary members, for the long political-philosophical discussions, for comfort in difficult moments and above all for all the laughter. I don't want to dwell too much, but I really want to send a very strong hug to **Alba**, **Denise**, **Beatrice**, both the two **Eriche**, **Daniele** and **Nicolò**. I will keep all the good old moments in my heart, forever. Rest assured that, however far I may be, they will not get rid of me easily!

Thanks to the old friends, who saw me grow up and grew up with me. I'm talking about **Alice**, **Esther**, **Ambra**, **Marta**, **Valentina**, **Roberta** and **Micol**, but also farthest friends such as **Eleonora** and **Matteo**, with whom I share a link immune to time and distance. I would have a thousand things to say, but I limit myself to one word: *thank you*. I can always count on them, and they know that this is mutual.

I thank the Theater, as a form of art and personal expression, because in addition to introducing me to wonderful people such as **Ilaria**, **Anna** and **Matilde**, it also made me know myself better. Thanks to all the friends from musical theater, for making me live a dream that I kept secret for too long, and thanks in general to all those who have shared the stage and the emotions with me over the years.

Before concluding these long acknowledgments, I promised myself to thank **Wikipedia**,

l'enciclopedia libera per eccellenza, senza la quale la mia formazione non sarebbe stata la stessa. Il mio impegno è quello di portare avanti l'ideale secondo il quale la conoscenza deve essere il più accessibile possibile. Merita una menzione speciale anche **Wolfram Alpha**, potente strumento che ha reso i miei primi anni universitari meno duri.

Per i miei genitori **Rita** e **Daniele** ho tenuto i ringraziamenti finali, quelli più speciali e importanti. Mi hanno insegnato ad essere ambizioso, determinato e curioso, crescendomi nel modo migliore possibile e permettendo che mi realizzassi qualunque fosse il mio obiettivo. Il mio successo è anche un vostro successo! Un abbraccio anche a mio fratello **Luca** e a mia cognata **Lina** per il supporto che mi danno costantemente. Un bacio alla piccola **Nicole**, con l'augurio che quando potrà leggere questa dedica fra qualche anno mantenga la curiosità che la caratterizza. D'altronde, è da quella che nascono gli scienziati! Un grazie di cuore alla mia meravigliosa cugina **Noemi**, che non solo mi ha regalato il capolavoro che è la copertina di questa tesi, ma che è sempre stata una delle mie più grandi fan sin da bambini.

Infine, l'ultimo ringraziamento va a quel ragazzo che da quattro anni mi sopporta, mi sostiene e mi ama nonostante i momenti difficili. Grazie al mio compagno di vita **Manlio**, le parole non sarebbero mai abbastanza per dire quanto migliore io sia diventato per merito suo. Quindi concludo dicendo solo questo: *ti amo.*

the free encyclopedia par excellence, without which my education would not have been the same. My commitment is to pursue the ideal according to which knowledge must be as accessible as possible. Also worth a special mention is **Wolfram Alpha**, a powerful tool that made my first university years less hard.

For my parents **Rita** and **Daniele** I kept the final acknowledgments, the most special and important ones. They taught me to be ambitious, determined and curious, raising me in the best way possible and allowing me to realize myself whatever my goal was. My success is also your success! A hug also to my brother **Luca** and to my sister in law **Lina** for the support they give me constantly. A kiss to the little **Nicole**, with the hope that when she can read this note in a few years, she will keep the curiosity that characterizes her. After all, it is from curiosity that scientists are born! A heartfelt thank you to my wonderful cousin **Noemi**, who not only gave me the masterpiece that is the cover of this thesis, but who has always been one of my biggest fans since childhood.

Finally, the last thanks goes to that guy who has been enduring me for four years, supports me and loves me despite the difficult moments. Thanks to my life partner **Manlio**, words would never be enough to say how much better I became thanks to him. So I conclude by just saying this: *I love you.*

Appendix A

Kreibig's linear relation

One of the corrections to the Quasi-Static Approximation treated in Chapter 3 is the *surface damping* (or surface scattering). In equation (2.43) the characteristic length of the process has been considered as:

$$\lambda_{boundary} = \frac{4}{3}r \tag{A.1}$$

as proved by Kreibig [62]. A simpler and more intuitive motivation of this choice is provided hereafter, based solely on geometrical considerations. Since scattering events are considered independent from one another, in this treatment only the surface damping is modeled.

Consider a spherical nanoparticle of radius r inside which electrons can travel only in straight trajectories. Let $P(x, y, z)$ be the initial point on the surface where an electron has just collided with the boundary, and let $P'(x', y', z')$ be a generic final point on the sphere surface where the electron will impact after traveling a distance $d[P, P']$. Then:

$$x^2 + y^2 + z^2 = r^2, \qquad x'^2 + y'^2 + z'^2 = r^2 \tag{A.2}$$

Since the scattering is assumed isotropic inside the sphere, all the points P' belonging to the surface have the same probability of being hit.

Without loss of generality, consider a reference system so that the initial point is $P(0, 0, r)$.

$$d[P, P'] = \sqrt{x'^2 + y'^2 + (z' - r)^2} = \sqrt{2r(r - z')} = \sqrt{2}r\sqrt{1 - \frac{z'}{r}} \tag{A.3}$$

The characteristic length of the process $\lambda_{boundary}$ can be defined as the average distance of all the possible ones:

$$\lambda_{boundary} = \frac{\int_\Omega \int_{-r}^r d[P, P']dz'd\Omega}{\int_\Omega \int_{-r}^r dz'd\Omega} = \frac{\int_{-r}^r d[P, P']dz'}{\int_{-r}^r dz'} \frac{\cancel{4\pi}}{\cancel{4\pi}} = \frac{\sqrt{2}\cancel{r} \int_{-r}^r \sqrt{1 - \frac{z'}{r}}dz'}{2\cancel{r}} \tag{A.4}$$

The integral can be rewritten and solved by changing the integration variable:

$$a = 1 - \frac{z'}{r} \quad \Rightarrow \quad dz' = -rda \tag{A.5}$$

$$\lambda_{boundary} = \frac{\sqrt{2}r}{2} \int_0^2 \sqrt{a}\ da = \frac{\sqrt{2}r}{2} \frac{4\sqrt{2}}{3} = \frac{4}{3}r \tag{A.6}$$

While the coefficient 4/3 had been discussed by other authors, the linear relation is reasonable and does perfectly fit the experimental data.

Appendix B

Code

Here presented are the integral Lumerical's FDTD Solutions scripts made and used for my simulations. All code is original and free to use and to modify for any imaginable purpose.

Note: since the materials' fit parameters could not be overwritten on the original ones, the models have been saved in copies such as *"H2O (Water) - Palik Copy 1"*.

B.1   Nanorods

```
1  #Initialization
2  clear; #clear all declared variables
3
4  simtime=150; #simulation time in fs
5  meshacc=2; #mesh accuracy (1=lowest, 8=highest)
6  detail=20; #number of mesh per smallest detail
7
8  lambda_start=300; #wavelength start in nm
9  lambda_stop=800; #wavelength stop in nm
10 n_freq=501; #number of points in the frequency spectrum
11
12 points_l=17; #number of lengths tested
13 l_array=linspace(20,100,points_l); #create a linear array of lengths between
      min and max
14 points_w=7; #number of widths tested
15 w_array=linspace(20,50,points_w); #create a linear array of widths between
      min and max
16 points_H=7; #number of heights tested
17 H_array=linspace(20,50,points_H); #create a linear array of heights between
      min and max
18
19 D=4; #distance of the 3D monitor from the particle's surface in nm
20
21 f_print="[NR] screening.txt"; #text file with results
22
23 if (fileexists(f_print)) { rm(f_print);} #remove the file it if already
      exists
24
25 #Write results file header
26 write(f_maxe,"Screening of Au Smoothed quadrilateral NP");
27 write(f_maxe,"Dimensions and Wavelenght in nm, |E|^2/|E0|^2 in a.u.");
28 write(f_maxe,"    ");
29 write(f_maxe,"l [nm]  w [nm]  H [nm]  lambda [nm] Avg F.E. [a.u.]");
```

```
30  AvgE=zeros(n_freq); #reset the array containing the average field enh.
31
32  for(i_H=1:points_H) #cycle different heights
33  {
34    for(i_w=1:points_w) #cycle different widths
35    {
36      for(i_l=1;i_l<=points_l;i_l=i_l+1) #cycle different lengths
37      {
38        switchtolayout; #switch to layout mode
39        deleteall; #delete previously created objects
40        l=l_array(i_l); #set length
41        w=w_array(i_w); #set width
42        H=H_array(i_H); #set height
43        R=w;  #set smooth edges radius as min[l,w,H]/2
44        if(R>l)
45        {R=l;}
46        if(R>H)
47        {R=H;}
48        R=R/2;
49
50        #Nanorod setup
51        addobject('rd_quad_extpoly'); #add smoothed rod
52        set('name','np');
53        set('x',0);
54        set('y',0);
55        set('z',0);
56        set('material','Au (Gold) - CRC Copy 1');
57        set('x span', l*1e-9);
58        set('y span', w*1e-9);
59        set('z span', H*1e-9);
60        set('radius', R*1e-9);
61
62        #Water
63        addrect;
64        set('name','water');
65        set('x',0);
66        set('y',0);
67        set('z',0);
68        set('x span', 2e-6);
69        set('y span', 2e-6);
70        set('z span', 2e-6);
71        set('material','H2O (Water) - Palik Copy 1');
72        set('override mesh order from material database',true);
73        set('mesh order',3);
74
75        #Simulation region
76        addfdtd;
77        set('x',0);
78        set('y',0);
79        set('z',0);
80        set('x span', (l+800)*1e-9);
81        set('y span', (w+800)*1e-9);
82        set('z span', (H+800)*1e-9);
83        set('simulation time',simtime*1e-15);
84        set('mesh accuracy',meshacc);
85        set('x min bc',5); #simmetry
86        set('y min bc',4); #simmetry
87
88        #TFSF Source
89        addtfsf;
```

90

```
90          set('x',0);
91          set('y',0);
92          set('z',0);
93          set('x span', (l+2*D+w+10)*1e-9);
94          set('y span', (w+10)*1e-9);
95          set('z span', (H+20)*1e-9);
96          set('wavelength start',lambda_start*1e-9);
97          set('wavelength stop',lambda_stop*1e-9);
98          set('direction',1); #Backward direction
99
100         #Uniform mesh inside TFSF region
101         addmesh;
102         set('dx',R/detail*1e-9);
103         set('dy',R/detail*1e-9);
104         set('dz',R/detail*1e-9);
105         set('x',0);
106         set('y',0);
107         set('z',0);
108         set('x span', (l+2*D+w+10)*1e-9);
109         set('y span', (w+10)*1e-9);
110         set('z span', (H+20)*1e-9);
111
112         #Field monitors
113         addpower;
114         set('name','E');
115         set('monitor type',8); #3D power monitor
116         set('x',(l/2+D+w/4)*1e-9);
117         set('y',0);
118         set('z',0);
119         set('x span', w/2*1e-9);
120         set('y span', w/2*1e-9);
121         set('z span', H*1e-9);
122
123         setglobalmonitor("frequency points",n_freq); #Set global monitors
    frequency points
124
125         run; #Start the simulation
126
127         E=getelectric('E'); #Returns |E|^2/|E0|^2 in 4D matrix E
128         Elambda=getresult('E','E');
129         lambda_array=(Elambda.lambda)*1e9; #Pick the array of measured
    wavelengths (not linear)
130
131         for(j=1:n_freq)
132         {
133           Ej=pinch(E,4,j); #Pick the 3 D matrix at the desired frequency
134           AvgE(j)=mean(Ej); #Calculate the average field enhancement
135         }
136
137         pos=findpeaks(AvgE); #Find peak position
138         write(f_maxe, num2str(l)+" "+num2str(w)+" "+num2str(H)+" "+num2str(
    lambda_array(pos))+" "+num2str(AvgE(pos)));  # Write one row of data (l,
     w, H, lambda peak, avg F.E.)
139         if(lambda_array(pos)>780) #Skip to next width if peak is too red
    shifted (save computational time)
140         {i_l=points_l+1;}
141       }
142   }
143 }
```

B.2   Nanospheres

```
1  #Initialization
2  clear; #clear all declared variables
3
4  simtime=150; #simulation time in fs
5  meshacc=2; #mesh accuracy (1=lowest, 8=highest)
6  detail=40; #number of mesh per radius
7
8  lambda_start=300; #wavelength start in nm
9  lambda_stop=800; #wavelength stop in nm
10 n_freq=501; #number of points in the frequency spectrum
11
12 points_R=20; #number of tests
13 R_array=linspace(6,44,points_R); #create a linear array of radii between min
      and max
14 D=4; #distance of the 3D monitor from the particle's surface in nm
15
16 f_print="[NP] spheres screening.txt"; #text file with results
17
18 if (fileexists(f_print)) { rm(f_print);} # remove the file it if already
    exists
19
20 #Write results file header
21 write(f_print,"Screening of Au Spherical NP");
22 write(f_print,"Dimensions and Wavelenght in nm, |E|^2/|E0|^2 in a.u.");
23 write(f_print,"   ");
24 write(f_print,"R[nm]  lambda [nm] Avg F.E. [a.u.]");
25
26 AvgE=zeros(n_freq); #reset the array containing the average field enh.
27
28 for(i_R=1;i_R<=points_R;i_R=i_R+1) #cycle different radii
29 {
30   switchtolayout; #switch to layout mode
31   deleteall; #delete previously created objects
32   R=R_array(i_R); #set radius
33
34   #Nanoparticle setup
35   addsphere;
36   set('name','np');
37   set('x',0);
38   set('y',0);
39   set('z',0);
40   set('material','Au (Gold) - CRC Copy 1');
41   set('radius', R*1e-9);
42
43   #Water
44   addrect;
45   set('name','water');
46   set('x',0);
47   set('y',0);
48   set('z',0);
49   set('x span', 2e-6);
50   set('y span', 2e-6);
51   set('z span', 2e-6);
52   set('material','H2O (Water) - Palik Copy 1');
53   set('override mesh order from material database',true);
54   set('mesh order',3);
55
56   #Simulation region
```

```
57    addfdtd;
58    set('x',0);
59    set('y',0);
60    set('z',0);
61    set('x span', (2*R+800)*1e-9);
62    set('y span', (2*R+800)*1e-9);
63    set('z span', (2*R+800)*1e-9);
64    set('simulation time',simtime*1e-15);
65    set('mesh accuracy',meshacc);
66    set('x min bc',5); #simmetry
67    set('y min bc',4); #simmetry
68
69    #TFSF Source
70    addtfsf;
71    set('x',0);
72    set('y',0);
73    set('z',0);
74    set('x span', (2*R+2*D+2*R)*1e-9);
75    set('y span', (2*R+2*D+2*R)*1e-9);
76    set('z span', (2*R+2*D+2*R)*1e-9);
77    set('wavelength start',lambda_start*1e-9);
78    set('wavelength stop',lambda_stop*1e-9);
79    set('direction',1); #Backward direction
80
81    #Uniform mesh inside TFSF region
82    addmesh;
83    set('dx',R/detail*1e-9);
84    set('dy',R/detail*1e-9);
85    set('dz',R/detail*1e-9);
86    set('x',0);
87    set('y',0);
88    set('z',0);
89    set('x span', (2*R+2*D+2*R)*1e-9);
90    set('y span', (2*R+2*D+2*R)*1e-9);
91    set('z span', (2*R+2*D+2*R)*1e-9);
92
93    #Field monitors
94    addpower;
95    set('name','E');
96    set('monitor type',8); #3D power monitor
97    set('x',(R+D+R/4)*1e-9);
98    set('y',0);
99    set('z',0);
100   set('x span', R/2*1e-9);
101   set('y span', R/2*1e-9);
102   set('z span', R/2*1e-9);
103
104   setglobalmonitor("frequency points",n_freq); #Set global monitors
       frequency points
105
106   run; #Start the simulation
107
108   E=getelectric('E'); #Return |E|^2/|E0|^2 in 4D matrix E
109   Elambda=getresult('E','E');
110   lambda_array=(Elambda.lambda)*1e9; #Pick the array of measured wavelengths
       (not linear)
111
112   for(j=1:n_freq)
113   {
114      Ej=pinch(E,4,j); #Pick the 3D matrix at the desired frequency
```

```
115        AvgE(j)=mean(Ej); #Calculate the average field enhancement
116    }
117
118    pos=findpeaks(AvgE); #Find peak position
119    write(f_print, num2str(R)+" "+num2str(lambda_array(pos))+"  "+num2str(AvgE
       (pos))); #Write one row of data (radius, lambda peak, avg F.E.)
120 }
```

B.3   Nanostars

```
 1  #Initialization
 2  clear; #clear all declared variables
 3
 4  simtime=200; #simulation time in fs
 5  meshacc=2; #mesh accuracy (1=lowest, 8=highest)
 6  detail=30; #number of mesh per smallest detail
 7
 8  lambda_start=300; #wavelength start in nm
 9  lambda_stop=1000; #wavelength stop in nm
10  n_freq=701; #number of points in the frequency spectrum
11
12  points_R=7; #number of tests performed
13  R_min=20; #minimum core radius tested
14  R_max=50; #maximum core radius tested
15  R_array=linspace(R_min,R_max,points_R); #creates a linear array of radii
       between min and max
16
17  D=4; #distance of the 3D monitor from the particle's surface in nm
18  L_tip=10; #tip lenght in nm
19  theta=40; #cone angle in degrees
20  r=3; #cone tip radius in nm
21
22  f_print="[NS] screening.txt"; #text file with results
23
24  if (fileexists(f_print)) { rm(f_print);} #remove the file it if already
       exists
25
26  #Write results file header
27  write(f_print,"Screening of Au NSs");
28  write(f_print,"Dimensions and Wavelenght in nm, |E|^2/|E0|^2 in a.u.");
29  write(f_print,"   ");
30  write(f_print,"R [nm] lambda [nm] Avg F.E. [a.u.]");
31
32  AvgE=zeros(n_freq); #reset the array containing the average field enh.
33
34  for(i_R=1;i_R<=points_R;i_R=i_R+1) #cycle different core radii
35  {
36    switchtolayout; #switch to layout mode
37    deleteall; #delete previously created objects
38    R=R_array(i_R); #set radius
39
40    n=2*pi*R/r+0.5; #number of spikes in largest circumference
41
42    #Nanostar setup - core
43    addsphere;
44    set('name','core');
45    set('radius',R*1e-9);
46    set('material','Au (Gold) - CRC Copy 1');
47    set('x',0);
```

94

```
48    set('y',0);
49    set('z',0);
50
51    #Nanostars setup - round of spikes
52    for(i=0;i<n;i=i+1)
53    {
54      addrect;
55      set('name','nullrect'+num2str(i));
56      set('override mesh order from material database',true);
57      set('mesh order',5);
58      set('alpha',0);
59      set('x span',(2*R+L_tip)*1e-9);
60      set('y span',2*r*1e-9);
61      set('z span',2*r*1e-9);
62      set('x',(R+L_tip/2)*1e-9);
63      set('y',0);
64      set('z',0);
65      addtogroup('tip'+num2str(i));
66
67      addobject('rd_tip_cone');
68      set('name','tipgold'+num2str(i));
69      set('material','Au (Gold) - CRC Copy 1');
70      set('z span',L_tip*1e-9);
71      set('cladding radius',r*1e-9);
72      set('tip radius',0.05*R*1e-9);
73      set('cone angle',theta);
74      set('x',-(R+L_tip/3)*1e-9);
75      set('y',0);
76      set('z',0);
77      addtogroup('tip'+num2str(i));
78
79      select('tip'+num2str(i));
80      set('x',0);
81      set('y',0);
82      set('z',0);
83      set('first axis','x');
84      set('second axis','y');
85      set('third axis','z');
86      set('rotation 1',0);
87      set('rotation 2',360/n*i);
88      set('rotation 3',0);
89      addtogroup('round');
90    }
91
92    #Nanostars setup - cover the surface with spikes
93    for(i=1;i<n/2;i=i+1)
94    {
95      select('round');
96      copy;
97      set('name','round'+num2str(i));
98      set('x',0);
99      set('y',0);
100     set('z',0);
101     set('first axis','x');
102     set('second axis','y');
103     set('third axis','z');
104     set('rotation 1',2*360/n*i);
105     set('rotation 2',0);
106     set('rotation 3',0);
107   }
```

```
108    #Water
109    addrect;
110    set('name','water');
111    set('x',0);
112    set('y',0);
113    set('z',0);
114    set('x span', 2e-6);
115    set('y span', 2e-6);
116    set('z span', 2e-6);
117    set('material','H2O (Water) - Palik Copy 1');
118    set('override mesh order from material database',true);
119    set('mesh order',3);
120
121    #Simulation region
122    addfdtd;
123    set('x',0);
124    set('y',0);
125    set('z',0);
126    set('x span', (800+2*R+2*L_tip)*1e-9);
127    set('y span', (800+2*R+2*L_tip)*1e-9);
128    set('z span', (800+2*R+2*L_tip)*1e-9);
129    set('simulation time',simtime*1e-15);
130    set('mesh accuracy',meshacc);
131    set('x min bc',5); #simmetry
132    set('y min bc',4); #simmetry
133
134    #TFSF Source
135    addtfsf;
136    set('x',0);
137    set('y',0);
138    set('z',0);
139    set('x span', (8*R)*1e-9);
140    set('y span', (8*R)*1e-9);
141    set('z span', (8*R)*1e-9);
142    set('wavelength start',lambda_start*1e-9);
143    set('wavelength stop',lambda_stop*1e-9);
144    set('direction',1); #Backward direction
145
146    #Uniform mesh inside TFSF region
147    addmesh;
148    set('dx',R/detail*1e-9);
149    set('dy',R/detail*1e-9);
150    set('dz',R/detail*1e-9);
151    set('x',0);
152    set('y',0);
153    set('z',0);
154    set('x span', (2*R+2*L_tip)*1e-9);
155    set('y span', (2*R+2*L_tip)*1e-9);
156    set('z span', (2*R+2*L_tip)*1e-9);
157
158    #Field monitors
159    addpower;
160    set('name','E');
161    set('monitor type',8); #3D power monitor
162    set('x',(R+D+L_tip)*1e-9);
163    set('y',0);
164    set('z',0);
165    set('x span', R*1e-9);
166    set('y span', R*1e-9);
167    set('z span', R*1e-9);
```

96

```
168    #Cross section monitors - Absorption (inside TFSF region)
169    addobject('cross_section');
170    set('name','cs_abs');
171    set('x',0);
172    set('y',0);
173    set('z',0);
174    set('x span',(2*R+L_tip)*1e-9);
175    set('y span',(2*R+L_tip)*1e-9);
176    set('z span',(2*R+L_tip)*1e-9);
177
178    #Cross section monitors - Scattering (outside TFSF region)
179    addobject('cross_section');
180    set('name','cs_sca');
181    set('x',0);
182    set('y',0);
183    set('z',0);
184    set('x span',(2*R+3*L_tip)*1e-9);
185    set('y span',(2*R+3*L_tip)*1e-9);
186    set('z span',(2*R+3*L_tip)*1e-9);
187
188    setglobalmonitor("frequency points",n_freq); #Set global monitors
        frequency points
189
190    run; #Start the simulation
191
192    E=getelectric('E'); #Return |E|^2/|E0|^2 in 4D matrix E
193    Elambda=getresult('E','E');
194    lambda_array=(Elambda.lambda)*1e9; #Pick the array of measured wavelengths
        (not linear)
195
196    for(j=1:n_freq)
197    {
198      Ej=pinch(E,4,j); #Pick the 3D matrix at the desired frequency
199      AvgE(j)=mean(Ej); #Calculate the average field enhancement
200    }
201
202    pos=findpeaks(AvgE); #Find peak position
203    write(f_print, num2str(R)+" "+num2str(lambda_array(pos))+"  "+num2str(AvgE
        (pos))); #Write one row of data (radius, lambda peak, avg F.E.)
204
205    cs_A=getresult('cs_abs','sigma'); #Return absorption cross section
206    cs_S=getresult('cs_sca','sigma'); #Return scattering cross section
207    print_cs_A=[cs_A.lambda*1e9,-cs_A.sigma]; #Create matrix with two columns
        (wavelength, cross section)
208    print_cs_S=[cs_S.lambda*1e9,cs_S.sigma]; #Create matrix with two columns (
        wavelength, cross section)
209    write('[4] cs_abs_'+num2str(R)+'.txt',num2str(print_cs_A)); #Write a text
        file with the absorption cross section
210    write('[4] cs_sca_'+num2str(R)+'.txt',num2str(print_cs_A)); #Write a text
        file with the scattering cross section
211 }
```

Bibliography

[1] Rodolfo R. Llinás, Yosef Yarom *Oscillatory properties of guinea-pig inferior olivary neurones and their pharmacological modulation: an in vitro study.* J. Physiol. 376, 163–82, 1986, DOI: 10.1113/jphysiol.1986.sp016147

[2] Youyang Zhao, Samsoon Inayat, Dmitriy A. Dikin, Joshua H. Singer, Rodney S. Ruoff, John B. Troy *Patch clamp technique: review of the current state of the art and potential contributions from nanoengineering.* J. Nanoengineering and Nanosystems, Volume 222, Issue 1, 1-11, 2008, DOI: 10.1243/17403499JNN149

[3] Joel M. Kralj, Daniel R. Hochbaum, Adam D. Douglass, Adam E. Cohen *Electrical Spiking in Escherichia coli Probed with a Fluorescent Voltage-Indicating Protein.* Science, 2011 Jul 15, 333(6040):345-8, DOI: 10.1126/science.1204763

[4] Sergei Kühn, Ulf Håkanson, Lavinia Rogobete, Vahid Sandoghdar *Enhancement of Single-Molecule Fluorescence Using a Gold Nanoparticle as an Optical Nanoantenna.* Physical Review Letters 97, 017402, 2006, DOI: 10.1103/PhysRevLett.97.017402

[5] Gualtiero Piccinini, Sonya Bahar *Neural Computation and the Computational Theory of Cognition.* Cogn. Sci. 37, 453–488, 2013, DOI: 10.1111/cogs.12012

[6] Eldra Solomon, Linda Berg, Diana W. Martin *Biology.* Brooks Cole, 8th edition, 2007, ISBN: 978-0495317142

[7] Eric R. Kandel, James H. Schwartz, Thomas M. Jessell, Steven A. Siegelbaum, A. James Hudspeth *Principles of Neural Science.* McGraw-Hill, 5th edition, 2012, ISBN: 978-0071390118

[8] Christof Koch *Biophysics of Computation: Information Processing in Single Neurons.* Oxford University Press, 1st edition, 2004, ISBN: 978-0195181999

[9] Oliver P. Ernst, David T. Lodowski, Marcus Elstner, Peter Hegemann, Leonid S. Brown, Hideki Kandori *Microbial and Animal Rhodopsins: Structures, Functions, and Molecular Mechanisms.* Chem. Rev. 2014, 114, 1, 126-163, DOI: 10.1021/cr4003769

[10] Mark Fox *Optical Properties of Solids.* Oxford University Press, 2nd edition, 2010, ISBN: 978-0199573370

[11] Luca Anghinolfi *Self-Organized Arrays of Gold Nanoparticles: Morphology and Plasmonic Properties.* Springer Nature, 1st edition, 2012, ISBN: 978-3642304958

[12] Mark L. Brongersma *Introductory lecture: nanoplasmonics.* Faraday Discuss., 2015, 178, 9-36, DOI: 10.1039/C5FD90020D

[13] Stephen D. Gedney *Introduction to the Finite-Difference Time-Domain (FDTD) Method for Electromagnetics.* Morgan & Claypool, 2011, ISBN: 9781608455232

[14] John B. Schneider *Understanding the Finite-Difference Time-Domain Method.* 2010, `www.eecs.wsu.edu/~schneidj/ufdtd`

[15] Alan L. Hodgkin, Andrew F. Huxley *A quantitative description of membrane current and its application to conduction and excitation in nerve.* J. Physiol., 1952, 117(4): 500–544, DOI: 10.1113/jphysiol.1952.sp004764

[16] Roger D. Traub, Robert K. S. Wong, Richard Miles, Hillary Michelson *A Model of CA3 Hippocampal Pyramidal Neuron Incorporating Voltage-Clamp Data on Intrinsic Conductances.* Journal of Neurophysiology, 66(2):635-50, DOI: 10.1152/jn.1991.66.2.635

[17] Dougal Maclaurin, Veena Venkatachalam, Hohjai Lee, Adam E. Cohen *Mechanism of voltage-sensitive fluorescence in a microbial rhodopsin.* Proc. Natl. Acad. Sci. USA, 2013 Apr 9, 110(15):5939-44, DOI: 10.1073/pnas.1215595110

[18] Joel M. Kralj, Adam D. Douglass, Daniel R. Hochbaum, Dougal Maclaurin, Adam E. Cohen *Optical recording of action potentials in mammalian neurons using a microbial rhodopsin.* Nat. Methods, 2011 Nov 27, 9(1):90-5, DOI: 10.1038/nmeth.1782

[19] Robert W. Corkery, Eric C. Tyrode *On the colour of wing scales in butterflies: iridescence and preferred orientation of single gyroid photonic crystals.* Interface Focus, June 2017, DOI: 10.1098/rsfs.2016.0154

[20] Les Cowley *Atmospheric Optics.* `https://www.atoptics.co.uk/`

[21] Philippe Walter, Eléonore Welcomme, Philippe Hallégot, Nestor J. Zaluzec, Christopher Deeb, Jacques Castaing, Patrick Veyssière, René Bréniaux, Jean-Luc Lévêque, Georges Tsoucaris *Early use of PbS nanotechnology for an ancient hair dyeing formula.* Nano Lett., 2006, 6 (10), DOI: 10.1021/nl061493u

[22] Robert H. Brill, Nicholas D. Cahill *A red opaque glass from Sardis and some thoughts on red opaques in general.* J. Glass Stud. 30, 16–27, 1988

[23] David J. Barber, Ian C. Freestone *An Investigation of the origin of the colour of the Lycurgus cup by analytical transmission electron microscopy.* Archaeometry, Volume 32, Issue 1, 1990, DOI: 10.1111/j.1475-4754.1990.tb01079.x

[24] Trustees of the British Museum, Creative Commons Attribution-NonCommercial-ShareAlike 4.0 International License

[25] Royal Institution of Great Britain, photography by Paul Wilkinson

[26] Craig F. Bohren, Donald R. Huffman *Absorption and scattering of light by small particles.* Wiley VCH Pub., 2012, ISBN: 9780471293408

[27] Michael Meier, Alexander Wokaun *Enhanced fields on large metal particles: dynamic depolarization.* Opt. Lett., 8:581, 1983, DOI:10.1364/OL.8.000581

[28] Masahiko Daimon, Akira Masumura *Measurement of the refractive index of distilled water from the near-infrared region to the ultraviolet region.* Appl. Opt. 46, Issue 18, 3811-3820, 2007, DOI: 10.1364/AO.46.003811

[29] Joseph R. Lakowicz *Principles of Fluorescence Spectroscopy.* Springer Nature, 3rd edition, 2006, ISBN: 978-0387312781

[30] Chris D. Geddes, Joseph R. Lakowicz *Metal-Enhanced Fluorescence.* Journal of Fluorescence, Vol. 12, Issue 2, 121-129, June 2002, DOI: 10.1023/A:1016875709579

[31] Karl H. Drexhage *Interaction of Light with Monomolecular Dye Layers.* Progress in Optics, 12:163-232, 1974, DOI: 10.1016/S0079-6638(08)70266-X

[32] Riccardo Sapienza, Toon Coenen, Jan Renger, Martin Kuttge, Niek F. van Hulst, Albert Polman *Deep-subwavelength imaging of the modal dispersion of light.* Nature Materials, Vol. 11, September 2012, DOI: 10.1038/NMAT3402

[33] Jacob P. Hoogenboom, Gabriel Sanchez-Mosteiro, Gerard Colas des Francs, Dominique Heinis, Guillaume Legay, Alain Dereux, Niek F. van Hulst *The Single Molecule Probe: Nanoscale Vectorial Mapping of Photonic Mode Density in a Metal Nanocavity.* Nano Lett., 2009, 9(3):1189-95, DOI: 10.1021/nl803865a

[34] Joseph R. Lakowicz *Radiative decay engineering 5: metal-enhanced fluorescence and plasmon emission.* Anal. Biochem., 2005, 15; 337(2): 171–194, DOI: 10.1016/j.ab.2004.11.026

[35] Vincenzo Amendola, Roberto Pilot, Marco Frasconi, Onofrio M. Maragò, Maria Antonia Iatì *Surface plasmon resonance in gold nanoparticles: a review.* J. Phys.: Condens. Matter, 29, 2017, 203002, DOI: 10.1088/1361-648X/aa60f3

[36] Agampodi S. De Silva Indrasekara, Sean F. Johnson, Ren A. Odion, Tuan Vo-Dinh *Manipulation of the Geometry and Modulation of the Optical Response of Surfactant-Free Gold Nanostars: A Systematic Bottom-Up Synthesis.* ACS Omega, 2018, 3, 2202-2210, DOI: 10.1021/acsomega.7b01700

[37] Lumerical's FDTD Solutions `https://www.lumerical.com/products/fdtd/`

[38] Lukas Novotny, Bert Hecht *Principles of nano-optics.* Cambridge University press, p.209, 2nd edition, 2012, ISBN: 978-1107005464

[39] Edward D. Palik *Handbook of Optical Constants of Solids - Water (H_2O).* Academic Press, 1998, ISBN: 978-0125444231

[40] David R. Lide *CRC Handbook of Chemistry and Physics - Optical Properties of Selected Elements.* CRC Press (Internet Version), 6th edition, Boca Raton, FL, 2005, ISBN 978-0849332043

[41] Lumerical's FDTD Solutions - TFSF manual `https://kb.lumerical.com/ref_sim_obj_sources_tfsf.html`

[42] Timothy R. Groves *Electron beam lithography.* Nanolithography, 2014, 80-115, DOI: 10.1533/9780857098757.80

[43] Sami Franssila *Introduction to Microfabrication.* John Wiley & Sons Inc., 2nd edition, 2010, ISBN: 978-0470749838

[44] Encyclopædia Britannica's definition of colloid `https://www.britannica.com/science/colloid`

[45] Enrique Carbó-Argibay, Stefanos Mourdikoudis, Isabel Pastoriza-Santos, Jorge Pérez-Juste *Nanocolloids of Noble Metals.* Nanocolloids - A Meeting Point for Scientists and Technologists, 2016, 37-73, DOI: 10.1016/B978-0-12-801578-0.00002-3

[46] Andrés Guerrero-Martínez, Silvia Barbosa, Isabel Pastoriza-Santos, Luis M. Liz-Marzán *Nanostars shine bright for you - Colloidal synthesis, properties and applications of branched metallic nanoparticles.* Current Opinion in Colloid & Interface Science, 16, 2011, 118–127, DOI:10.1016/j.cocis.2010.12.007

[47] Judith Kimling, Maryrita Maier, Berta Okenve, Vassilios Kotaidis, H. Ballot, Anton Plech *Turkevich Method for Gold Nanoparticle Synthesis Revisited.* J. Phys. Chem. B., 2006, 110, 32, 15700-15707, DOI: 10.1021/jp061667w

[48] Fudong Wang, Vernal N. Richards, Shawn P. Shields, William E. Buhro *Kinetics and Mechanisms of Aggregative Nanocrystal Growth.* Chem. Mater., 2014, 26, 5-21, DOI: 10.1021/cm402139r

[49] Silvia Barbosa, Amit Agrawal, Laura Rodríguez-Lorenzo, Isabel Pastoriza-Santos, Ramón A. Alvarez-Puebla, Andreas Kornowski, Horst Weller, Luis M. Liz-Marzán *Tuning Size and Sensing Properties in Colloidal Gold Nanostars.* Langmuir, 2010, 26(18), 14943–14950, DOI: 10.1021/la102559e

[50] Chun-Hong Kuo, Michael H. Huang *Synthesis of Branched Gold Nanocrystals by a Seeding Growth Approach.* Langmuir, 2005, 21, 5, 2012-2016, DOI: 10.1021/la0476332

[51] Leila Jamalzadeh, Hosein Ghafoori, Reyhaneh Sariri, Hanieh Rabuti, Jila Nasirzade, Hajar Hasani, Mahmoud Reza Aghamaali *Cytotoxic Effects of Some Common Organic Solvents on MCF-7, RAW-264.7 and Human Umbilical Vein Endothelial Cells.* Avicenna J. Med. Biochem., 2016 June, 4(1):e33453, DOI: 10.17795/ajmb-33453

[52] MyScope by Microscopy Australia `https://myscope.training/index.html` Creative Commons License (Attribution-ShareAlike 4.0 International)

[53] Paul J. Worsfold, Elias A.G. Zagatto *Spectrophotometry — Overview.* Encyclopedia of Analytical Science, 2005, 318-321, DOI: 10.1016/B978-0-12-409547-2.14265-9

[54] Aram Mooradian *Photoluminescence of Metals.* Phys. Rev. Lett., 22, 1969, 185-187, DOI: 10.1103/PhysRevLett.22.185

[55] H.A. Alluhaybi, Sibkrishna Ghoshal, Bahia O. Alsobhi, Wan Nurulhuda Wan Shamsuri *Visible Photoluminescence from Gold Nanoparticles: A Basic Insight.* Optik - International Journal for Light and Electron Optics, June 2019, 192:162936, DOI: 10.1016/j.ijleo.2019.162936

[56] Yuqing Cheng, Guowei Lu, Yingbo He, Hongming Shen, Jingyi Zhao, Keyu Xiad, Qihuang Gong *Luminescence quantum yields of gold nanoparticles varying with excitation wavelengths.* Nanoscale, January 2015, 8(4), DOI: 10.1039/C5NR07343J

[57] Hussein Nori Rubaiy *A Short Guide to Electrophysiology and Ion Channels.* J. Pharm. Pharm. Sci., 20, 48 - 67, 2017, DOI: 10.18433/jpps.v20i1.28694

[58] Krystyna Drozdowicz-Tomsia, Ewa M. Goldys *Gold and Silver Nanowires for Fluorescence Enhancement.* Nanowires - Fundamental Research, July 2011, DOI: 10.5772/16330

[59] Stephan Link, Mona B. Mohamed, Mostafa A. El-Sayed *Simulation of the Optical Absorption Spectra of Gold Nanorods as a Function of Their Aspect Ratio and the Effect of the Medium Dielectric Constant.* J. Phys. Chem. B 1999, 103, 16, 3073-3077, DOI: 10.1021/jp990183f

[60] Ron Milo, Paul Jorgensen, Uri Moran, Griffin Weber, Michael Springer *BioNumbers* - `https://bionumbers.hms.harvard.edu/files/Sizesofvariouscells.pdf` Nucleic Acids Res., 2010, 38(Database issue): D750–D753, DOI: 10.1093/nar/gkp889

[61] Shaheen A. Maniyar, Jameel G. Jargar, Swastika N. Das, Salim A. Dhundasi, Kusal K. Das *Alteration of chemical behavior of L-ascorbic acid in combination with nickel sulfate*

at different pH solutions in vitro. Asian Pac. J. Trop. Biomed., 2012, 2(3): 220–222, DOI: 10.1016/S2221-1691(12)60045-8

[62] Uwe Kreibig *Electronic properties of small silver particles: the optical constants and their temperature dependence.* J. Phys. F: Met. Phys., 1974, 4, 999, DOI: 10.1088/0305-4608/4/7/007